STUDY OF SILICON NANOWIRE FIELD EFFECT TRANSISTOR FOR

ANALOG AND DIGITAL BIOSENSING

by

Pengyuan Zang

APPROVED BY SUPERVISORY COMMITTEE:

_____
Walter Hu, Chair

_____
Jeong-Bong Lee

_____
Lawrence J. Overzet

_____
Siavash Pourkamali

STUDY OF SILICON NANOWIRE FIELD EFFECT TRANSISTOR FOR

ANALOG AND DIGITAL BIOSENSING

by

PENGYUAN ZANG, BS, MS

DISSERTATION

Presented to the Faculty of

The University of Texas at Dallas

in Partial Fulfillment

of the Requirements

for the Degree of

DOCTOR OF PHILOSOPHY IN

ELECTRICAL ENGINEERING

THE UNIVERSITY OF TEXAS AT DALLAS

May 2017

ACKNOWLEDGMENTS

can hardly imagine how I can get through the tough times without the courage and support from my family.

I would also like to express my gratitude to the other faculty members on my dissertation committee, for their full support of my research and my career, including Dr. Lawrence Overzet, Dr. Jeong Bong Lee, and Dr. Siavash Pourkamali. I really enjoyed my time working with Dr. Overzet as his teaching assistant, and I appreciate the opportunity to learn from him the qualities necessary to be successful. Over the years, other faculty members have helped me with my academic or personal growth, including Dr. Jie Zheng, Dr. Chadwin Young, Dr. William Frensley, and Dr. Dian Zhou from UT Dallas, as well as Dr. Xuan Zeng and Dr. Jun Tao from our collaborating group at Fudan University, China.

I have enjoyed the time working with my other colleagues and friends at UT Dallas, and I am grateful for their constructive and inspiring discussions as well as their spiritual support. During my first years after joining UTD, I learned a lot from the senior group members including Dr. Xinrong Yang, Dr. Ruhai Tian, Dr. Suresh Regonda, Lisa Spurgin, Dr. Krutarth Trivedi, Dr. Edward Castellana, Gary Kendall, Serena Greene and Dr. Yi Yang. I genuinely appreciate the cleanroom hands-on experience imparted by Lisa Spurgin, as well as her kindness and great personality. On the other hand, it was my pleasure to work with the biosensor team, including Yuchen Liang, Silu Zhang, Honglei Wang, Fengquan Song, and Brandi Kirkpatrick. The mutual learning from our countless discussions has benefited all of us. I would also like to extend my thanks to other current and former group members, including Balasubramaniam Balachandran, Devashish Lingam, Vikramshankar Kamakoti, Shannon Menezes, David Gehlhausen, and Michael Wallace. Additionally, I have been blessed to have the academic and/or spiritual

STUDY OF SILICON NANOWIRE FIELD EFFECT TRANSISTOR FOR

ANALOG AND DIGITAL BIOSENSING

Pengyuan Zang, PhD
The University of Texas at Dallas, 2017

Supervising Professor: Walter Hu

The advancement of semiconductor technology has popularized the low power, economical and

small form-factor solid-state devices, such as those highly integrated and interconnected as the

fundamental infrastructure for the internet of things (IoT). Due to its CMOS-compatibility and

electrical interface, biosensors that utilize field effect transistor (FET) as transducer have become

the perfect candidate to interface directly with the chemical and biological properties of the

physical world. Especially, nanowire (NW) FET biosensor has received great attention as a

highly sensitive biosensing platform, benefiting from its large surface-to-volume ratio. In this

work, several challenges and key aspects of existing NW FET biosensor were studied, and

solutions were proposed to address these problems. For example, the hydrolytic stability of the

surface sensing element was evaluated and improved by a hydrolysis process, which led to a

significant increase in the overall biosensor performance. Another challenge is the noise in the

electric potential of the sensing solutions. A secondary reference electrode was introduced and

its potential was used to subtract the noise from the measured sensor output in the biosensing

system. Compared to a reference FET, this approach greatly reduced the system complexity and

requirement, yet still improved the limit of detection (LOD) by 50 – 70%. In the next portion of this work, investigations of the analyte sensitivity show that it can be considerably affected by the charge buffering effect from the surface hydroxyl groups. Analytical studies and numerical simulations reveal that both low pH sensitivity and large analyte buffer capacity are required to achieve a reasonable analyte sensitivity. Finally, the most significant portion of this work was the experimental demonstration of the digital biosensing concept with single serpentine NW FET biosensor. The majority of existing FET biosensors utilize the device as an analog transducer, which measures the captured analyte density to generate an output, and suffers from various noise factors, especially the nonspecific changes of the sensing solutions than cannot be reduced by averaging. Digital biosensor no longer depends on the amplitude of the sensor output and is therefore better immune to these noise factors. Instead, the individual binding events of single analyte are counted and analyzed statistically to determine the analyte concentration. The single serpentine NW FET is the ideal device design to achieve digital biosensing. It maintains the low noise level with the equivalently long channel, yet achieves a small footprint enough for binding of only a single analyte. The binding of analyte to multiple segments of the NW results in both higher sensitivity and binding avidity. The small footprint also enables high integration density of the individual digital biosensors into an array format, which is a responsive, highly sensitive, and cost-effective future biosensing platform.

TABLE OF CONTENTS

LIST OF FIGURES

CHAPTER 1

INTRODUCTION

1.1   Overview

Affinity-based silicon nanowire field effect transistors (Si NW FETs) have been proven as potential candidates of highly sensitive, rapid, label-free, miniaturized and low-cost biosensors for biological/chemical analyte sensing [1-6]. Their high sensitivity has been demonstrated by single analyte detection [7], as well as extremely low limit of detection (LOD) even down to femto molar range [5, 8, 9]. As a highly cross-disciplinary research topic, the NW FET biosensor combines the device physics of advanced semiconductor device structures, the surface chemistry to functionalize the active surface making it biologically sensitive, and the study of charge states in the biosensing system including the surface species and the biological analyte. To truly understand the advantages and limitations of the NW FET biosensor, some fundamental concepts and background information were reviewed in the immediate following sections, including the ion-sensitive FETs (ISFETs), affinity-based biosensors, biologically-sensitive FETs, ImmunoFETs, and NW FET biosensors. The first three are critical to understand the fundamentals of the general FET biosensor. Especially, the ISFET concept is directly related to the pH-sensing work in Chapter 2. ImmunoFET utilizes antibody as the sensing element, and this configuration was used in both Chapters 3 and 5. The section on NW FET biosensors reviewed the sensitivity improvement of the NW FET in biosensing, from the perspective of device physics. In the last section of this chapter, various challenges of existing NW FET biosensors were discussed, which led to the motivations of the work in the following chapters.

1.2   Ion-Sensitive Field Effect Transistors (ISFETs)

The fast and vast growth and development of semiconductor industry, which has mainly based

on Si FETs over the past decades, has been proven a great success. The idea has been introduced

long ago in the 1970s for sensing charged chemical species (ions) utilizing the FET technologies

[10], known as the ion-sensitive field-effect transistors (ISFETs). Inheriting from its parents,

ISFET also benefits from lower cost in mass production with better performance as

semiconductor process advances, as well as uniform characteristics across devices due to the

high reproducibility that the semiconductor industry relies on [11].
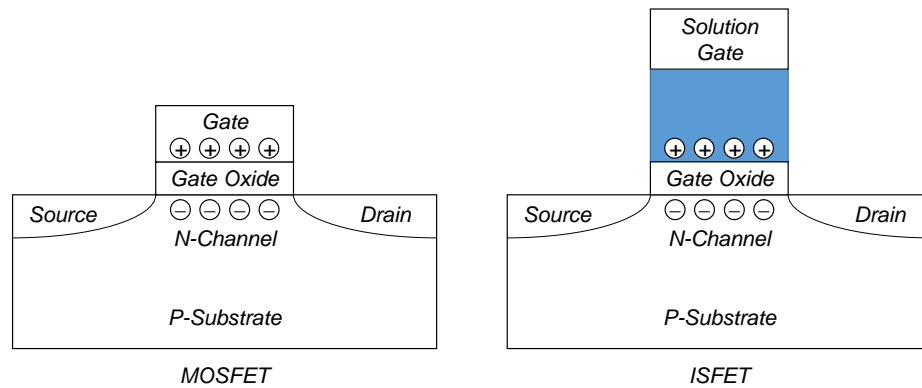
Figure 1.1. Comparison of MOSFET and ISFET structures

The structures of a conventional MOSFET and an ISFET are shown in Figure 1.1. The gate

terminal controls the current flow in the channel between the source and drain terminals. If a

constant voltage is applied between source and drain, then the current is determined solely by the

channel conductance or charge carrier concentration, which varies with the doping concentration

and the Fermi level. For a MOSFET, the abbreviation of "MOS" represents a metal-oxide-

semiconductor structure. As the gate voltage is altered, the Fermi level position (relative to

conduction/valance band) also changes at the oxide-semiconductor interface, which is then

reflected as a dramatic change in the carrier concentration. For an ISFET, however, the gate and gate oxide are not directly in contact with each other, but exposed both to a solution of ions. The solution gate (or reference electrode as used in some literatures) sets the potential of the solution that biases the device to a certain working condition. On the other hand, an electric surface charge is built up in the solution at the solution-oxide interface, which generates an electric field not only attracting the counter charges in the solution forming a double layer (DL), but also shifting the channel Fermi level through the change of surface potential, as equivalently caused by a deviation in the threshold voltage. By careful modification of the oxide surface with certain chemical species (e.g., amino groups and hydroxyl groups for pH sensing), the surface charge density can be made sensitive to certain ions in the bulk solution. Therefore, if the concentration of target ion changes in the bulk solution, the variation of the oxide surface charge will shift the Fermi level in the channel, which can then be detected from the source/drain current. This structural difference makes ISFET capable of sensing ions in solutions.

1.3   Affinity-Based Biosensors

Innovation in biosensor technology has been contributing to the revolutionary changes of methodology to detect and characterize biological molecules [12]. Its applications include the well-known commercial success of enzyme electrodes for blood glucose detection, as well as those in food processing, clinical diagnostics, environmental monitoring, antiterrorism, etc. [13]. Biosensor, or affinity-based biosensor, is the integration or interfacing of a transducer with a specific biological sensing element, such as antibody, receptor protein, enzyme, or DNA [12-14]. A biosensor utilizes the specific reaction between the target species (analytes) and the sensing element, which is then detected and converted by the transducer to a measurable electric signal.

Regardless of the specific transducer type or sensing element, the fundamental detection process of a biosensor involves the following steps [14]: (i) the collision of the analytes with the sensing elements, usually via diffusion (mass transportation), (ii) the selective and specific reaction of the analytes with the sensing elements, such as forming a chemical bond, and (iii) the transduction of the reaction, triggered either internally by the properties of the analyte, such as the dielectric constant change due to analyte binding in a capacitive sensor, or externally via label molecules as in fluorescent spectroscopy. The last step is where various biosensing platforms differ from each other. What makes biosensors the most useful in the aforementioned applications is that the analyte concentration can be related to the signal intensity recorded from the transducer [12]. Based on the different transducer types, affinity-based biosensors can be commonly categorized as electrochemical, optical-electronic, optical and acoustic [13].

1.4   Biologically-Sensitive Field-Effect Transistors (Bio-FETs)

The utilization of FET in ion detection (i.e., ISFET) can be expanded to biosensing as well. By incorporating FET as a charge sensor, binding activities of charged analytes can be detected and converted to electronic signal for quantification. Such biosensors based on charge detection with FETs are generally referred to as biologically-sensitive field-effect transistors (bio-FETs), although the same term may also denote other applications of FETs in biosensing, such as the detection of dipole under alternating-current (AC) conditions [15]. In comparison to classical electrochemical biosensors (such as enzyme electrodes), bio-FETs are miniaturized solid-state devices possessing most of the benefits from ISFETs, including cost effectiveness in mass production, ease of integration with other circuits for post processing and automation, etc.

In order to recognize specific analytes in different sensing applications, bio-FETs requires

modification with the sensing elements. The wide availability of the sensing elements, including

DNA, antibody, peptide, enzyme, aptamer, etc., makes bio-FETs versatile for the detection of

different targets, such as DNA, protein, carbohydrate, small organic molecules, etc. [16, 17].

The immobilization of sensing elements, which are by nature organic biological molecules, on

the solid-state sensor surface, is generally achieved via a layer of linker molecules, usually the

self-assembled monolayer (SAM). The active surface to be modified is normally gate dielectric

(e.g., metal oxide), though metals have also been reported which were used as gate electrode

[18]. The binding reaction between sensing elements and analytes is sensed via the charges

carried by the latter. Therefore, labelling conjugates are not required for the detection, which are

indispensable in some optical biosensors like fluorescence detection and enzyme-linked

immunosorbent assay (ELISA). As a result, bio-FETs are label-free biosensors.
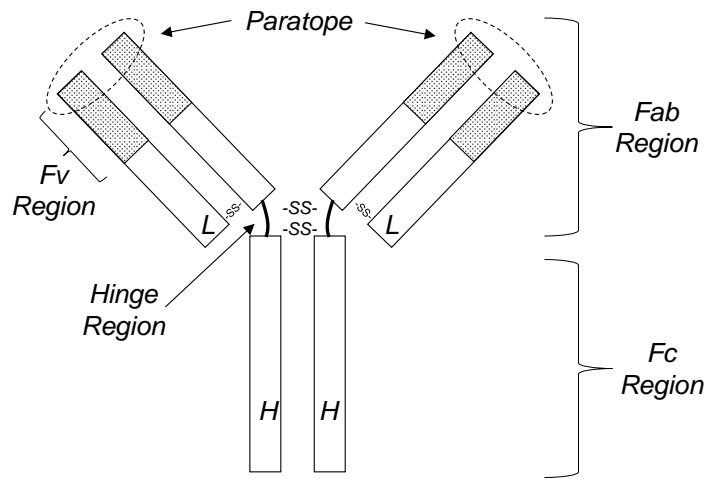
Figure 1.2. Basic structure of antibody

1.5   ImmunoFETs and Antibody

Immunosensors are biosensors based on immunochemical reaction where antibody or antigen is

immobilized to the transducer [13, 19]. Those that utilize FETs as transducers are immunoFETs.

Being a crucial part of the immune system, antibody, or immunoglobulin (Ig), is a type of Y-

shaped proteins produced by the plasma cells and is capable of binding and neutralizing

pathogens, also known as antigens [20, 21]. As shown in Figure 1.2, an antibody is constructed

from four polypeptide chains connected via disulfide bonds: two identical heavy chains (labeled

as "H") and two identical light chains (labeled as "L"). Depending on the different types of

heavy chains, antibodies can be categorized into five classes or isotypes: immunoglobulin M

(IgM), immunoglobulin D (IgD), immunoglobulin G (IgG), immunoglobulin A (IgA) and

immunoglobulin E (IgE). Each arm of the "Y" is called the fragment antigen-binding (Fab)

region, which is composed of a variable (Fv) region (shaded area) and the remaining constant

region. The binding site of the antibody, named paratope, is located at the amino terminal end of

each variable region (i.e, each tip of the "Y"), which recognizes one particular binding site on the

antigen, named epitope. The specific binding between paratope and epitope makes antibodies

highly selective to certain unique parts of the antigen, while the extensive variability of the

variable domain enables the detection of virtually any antigen structure. The base of the "Y" is

called fragment crystallizable (Fc) region, and is connected to the Fab region via the hinge

region, a flexible stretch of polypeptide chain. Due to the flexibility of the hinge region in IgA

and IgG, the two Fab arms can be adopted to different angles, therefore allowing binding to

epitopes spaced at various distances.

Among the five isotypes of immunoglobulin, IgG (with γ heavy chain) has been attracting much

attention in immunology research due to its abundance in serum. For human, mouse and rat, IgG

can be further divided into four subclasses: IgG1 to IgG4 in the order of decreasing abundance.

There are two properties of antibody that characterize its binding ability to antigens [21].

Affinity defines the binding strength of the antibody via a single paratope-epitope pair, while the

measure of the overall binding strength with more than one binding sites is termed avidity. The

latter is especially relevant to the pentameric IgM with ten binding sites, but we normally

consider the former for general one-to-one protein sensing with IgG. The binding affinity of an

antibody depends on the properties of antibody and antigen, as well as the reaction conditions

including temperature, pH and ionic strength.

Based on their clonality, antibodies can be divided into two groups: the monoclonal antibodies

are homogeneous and equally selective to the same epitope on the antigen; the polyclonal are a

mixture of antibodies with different affinities targeting at different epitopes of the antigen. In

comparison to polyclonal antibodies, monoclonal antibodies are preferred for immunosensors

due to the higher sensitivity and selectivity [22].   It has been shown that the antigen-antibody

reaction is more effective with monoclonal antibody [23], and most of the previous sensing

studies with immunoFETs favored monoclonal antibodies [7, 24-29].

The benefits of immunoFETs attributed to the nature of antibody have been discussed before.

The high specifity of paratope-epitope binding renders immunoFETs highly selective to the

preferred analytes. The variability of the Fv domain contributes to the versatility of antibodies

for almost any antigen, and their wide commercial availability greatly promotes the broad

applications of immunoFETs.

Despite the various benefits above, immunoFETs suffer from certain limitations as well. For

many antigens and even the antibodies as sensing elements, the carried charge is a function of

the solution pH, depending on the acid dissociation constants (pKa) of the various amino acid

7

present on the protein. Other charged surface species, such as the blocking agent from passivation, may also have a pH dependence. Therefore, the pH of all the sensing solutions should be consistent in order to minimize signal due to pH difference. Besides, this pH value should be determined carefully, not only to maximize the analyte charges, but also to reach an optimum condition for binding. In addition, the immunoFETs suffer from nonspecific binding which is a primary limitation in direct noncompetitive sensing [13]. The co-contaminants (any small charged molecules) non-specifically bind to the sensor surface, which cannot be distinguished from the analyte of interest by a sensor based on charge-detection. Polysorbate 20 has been reported as a washing agent to prevent nonspecific binding [25].

1.6 Nanowire FET Biosensors

Since the first experimental demonstration in 2001 [30], Si NW FET has been considered as one of the promising platform for biological analyte detection [3, 4, 31], mostly attributed to its increased sensitivity. As the diameter of the NW scales down, the surface-to-volume ratio drastically increases. As a results, the external electric field from surface-immobilized charges will not only affects the Fermi level near the wire surface, but also in the interior of the NW [32]. Consequently, NW FET have demonstrated improved charge sensitivity, which is confirmed by both simulation [33] and experiments [34].

Curreli et al. compared the sizes of different biological entities commonly for biosensors [6]. Many biological analytes of interest, such as virus and some proteins, are comparable to the typical size of NWs (tens of nanometers), which allows them to have strong modulation of the channel conductance. However, in pH sensing with protons as the target analytes, the proton-sensitive charge species are much smaller compared to the biological probes and analytes, and

their densities at the NW surface are much higher. Therefore, the improvement from scaling

effect is marginal in pH sensing [33].

1.6.1 The NW FET biosensor model

The working principle of NW FET biosensor is briefly reviewed. As charged analytes are

captured by the probes and immobilized on the sensor surface, the Fermi level of the

semiconductor channel will be shifted by the change in surface charge, resulting in the channel

conductance change. The surface potential ϕ_s, which is the potential at the oxide-electrolyte

interface, varies with the change of channel conductance. The immobilized surface charge Q_0 is

related to the surface potential change $\Delta\phi_s$ by the following relation:

$$Q_0 = \Delta\phi_s C_{FET}, \tag{1.1}$$

where C_{FET} is the capacitance between the surface charge and the NW FET/electrolyte system

[24]. As illustrated in Figure 1.3, there are three capacitances involved: the double layer (DL)

capacitance C_{DL}, the oxide capacitance C_{ox}, and the NW capacitance C_{NW}, which characterizes

the Fermi level shift respect to the carrier density change. As charge Q_0 binds to the oxide-

electrolyte surface, the carriers in the NW and the counter ions in the electrolyte will be attracted
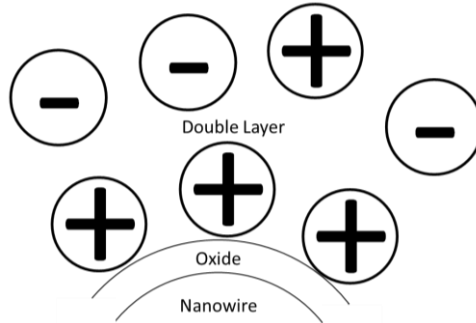
Figure 1.3. Illustration of the surface charge at nanowire oxide surface

9

and balance the surface charge, with their total charge equal to Q_0. Therefore, C_{FET} is equivalent to C_{DL} in parallel with the serial capacitance of C_{ox} and C_{NW} [24, 35, 36]:

$$C_{FET} = C_{DL} + \frac{1}{\frac{1}{C_{ox}} + \frac{1}{C_{NW}}}. \tag{1.2}$$

Gao et al. studied the change of C_{NW} for different carrier concentrations [24]. They concluded that as the NW FET was biased from linear regime (high carrier concentration) to subthreshold regime (low carrier concentration), the Debye screening length λ_{Si} will quickly increase beyond the NW diameter (full depletion), causing a rapid decrease of C_{NW}. From (1.2), $C_{FET} \sim C_{ox} + C_{DL}$ in the linear regime (large C_{NW}) and $C_{FET} \sim C_{DL}$ in the subthreshold regime (small C_{NW}). In our Si NG FET devices, the doping concentration is low (Boron, $10^{15}/cm^3$) and we bias our devices in the subthreshold regime. The screening length λ_{Si} at this low carrier concentration exceeds 100 nm [24], two to three times greater than our typical NW dimension (50 nm in width and 30 nm in height). Therefore, our Si NGFET biosensors are fully depleted, the electrostatic potential inside the Si NW remains constant, and the whole volume of NW is modulated by the surface charge.

In subthreshold regime, the drain current of the Si NW FET is

$$I_d = I_{d0}e^{\frac{\psi_s q}{k_B T}}, \tag{1.3}$$

where ψ_s is the potential at the silicon – oxide interface. Notice that for oxide with non-zero thickness, $\Delta\psi_s$ doesn't equal to $\Delta\phi_s$ and they can be related as [37]

$$A = \frac{C_{ox}}{C_{ox} + C_{NW}} = \frac{\Delta\psi_s}{\Delta\phi_s}. \tag{1.4}$$

After the binding of charged analytes which leads to the change of surface potential, the current will also change

10

$$I_{d1} = I_{d0}e^{\frac{\psi_{s1}q}{k_BT}}. \tag{1.5}$$

The signal is the difference between the two

$$\Delta I_d = I_{d1} - I_d = I_{d0}(e^{\frac{\psi_{s1}q}{k_BT}} - e^{\frac{\psi_sq}{k_BT}}). \tag{1.6}$$

We can write $\psi_{s1} = \psi_s + \Delta\psi_s$, and (1.6) becomes

$$\Delta I_d = I_{d0}e^{\frac{\psi_sq}{k_BT}}(e^{\frac{\Delta\psi_sq}{k_BT}} - 1). \tag{1.7}$$

In the field of FET biosensing, we usually care about the relative conductance change

$$\frac{\Delta G}{G} = \frac{\Delta I_d/V_{ds}}{I_d/V_{ds}} = \frac{\Delta I_d}{I_d} = e^{\frac{\Delta\psi_sq}{k_BT}} - 1. \tag{1.8}$$

By using (1.1) and (1.4), we can rewrite (1.8) as

$$\frac{\Delta G}{G} = e^{\frac{A\Delta\phi_sq}{k_BT}} - 1 = e^{\frac{AQ_0q}{C_{FET}k_BT}} - 1. \tag{1.9}$$

As discussed earlier, $C_{FET} \sim C_{DL}$ in the subthreshold regime, therefore

$$\frac{\Delta G}{G} = e^{\frac{AQ_0q}{C_{DL}k_BT}} - 1, \tag{1.10}$$

which relates the NW FET output to the charge binding to the surface.

1.7 Challenges of Existing NW FET Biosensors

One of the challenges with FET biosensors is the instability of the sensor in physiological

samples [38]. This may come from the device itself, or the surface chemistry. The majority of

FET biosensors require modification of the active surface in order to interact specifically with

the target analytes. The self-assembled monolayer (SAM) is an essential part of the surface

chemistry, and its hydrolytic stability directly limits the performance of FET biosensors by drift

and hysteresis [38-41]. To be more specific, the hydrolysis of surface species may lead to the

change of surface charge state, which alters the sensor output and affects the accuracy of detection. In Chapter 2, a hydrolysis process was developed, which was believed to remove the weakly bound SAM and stabilize the surface species. With the improved surface stability and reduced drift in pH sensing, we demonstrated detection accuracy down to ±0.008 pH, which was comparable to or exceeded some commercial ISFETs.

The other source of instability comes from the noise in the solution potential. Differential measurement can solve this problem by subtracting the common noise from an identical reference FET which, on the other hand, is insensitive to the target analyte [42]. In Chapter 3, a different differential approach was demonstrated with a secondary reference electrode. Compared to the reference FET, the secondary electrode greatly simplified the system setup, and reduced the challenges required by the reference FET. The results showed 50 – 70% reduction in LOD due to the suppressed potential noise and increased readability.

Most FET biosensors utilize silicon dioxide or other metal oxide as the gate dielectric, which has inherent pH sensitivity due to the high density of hydroxyl groups at the surface [27, 43, 44]. For analytes other than proton, this pH sensitivity may actually compete and compensate the change of surface charge due to analyte binding [45]. In Chapter 4, the site-binding model was expanded to include the analyte-probe binding, and the charge buffering effect was evaluated by both analytical studies and numerical simulation. The results suggested that analyte detection was possible only with a low pH sensitivity, but other factors such as the probe density and the equilibrium dissociation constant were also critical in the determination of analyte sensitivity.

The FET biosensors suffer from the increasing biological noise due to analyte binding/unbinding at low analyte concentration [14, 36]. To obtain accurate sensing results at low concentration,

most studies employed averaging from multiple measurements, multiple sensors or multiple NW channels [8, 9, 25, 30, 46]. Baseline is another factor that significantly affects the accuracy of the sensing result, and almost all time-dependent biosensors (excluding AC detection and simultaneous differential detection) require a separate step to establish the baseline without analytes binding to the biosensor [5, 8, 9, 25, 30, 47-49]. This can be the measurement of the channel conductance in a buffer solution before switching to the analyte solutions, or the extraction of the threshold voltage (V_T) from the measured transfer characteristics (I_{DS} - V_{GS}) prior to analyte incubation. Besides the analyte concentration, other conditions (*e.g.*, pH or ionic concentration of the solution) may have also slightly changed from baseline establishment to analyte detection, and some of them will cause a change in the sensor output as well. This change is not attributed to the binding of target analytes, and is therefore considered as a nonspecific offset from the background. More importantly, it cannot be corrected by averaging. In Chapter 5, the digital biosensing with single serpentine NW FET was demonstrated, which is inherently different from other approaches of analyte detection. The analyte concentration is determined via the counting of individual analyte binding events. This approach eliminates the nonspecific offset from the sensing results, as it no longer require a separate step to establish the baseline prior to the analyte detection. The single serpentine NW FET is considered as a perfect electrical transducer to achieve digital biosensing. By folding a long straight NW into a serpentine shape, the low device noise is maintained, while the small footprint enables single-analyte detection required by digital biosensing. The analyte is capable of binding to multiple segments of the serpentine NW, which leads to higher sensitivity and analyte binding avidity.

By integrating individual serpentine NW FETs into an array format, the digital biosensor has great potential as a novel platform to achieve fast, accurate and low-cost biosensing.

CHAPTER 2

IMPROVED HYDROLYTIC STABILITY AND REPEATABILITY: PH SENSING

WITH APTES-COATED SI NANOWIRE BIO-FETS[1]

Authors – Pengyuan Zang, Yuchen Liang, and Walter Hu

The Department of Electrical Engineering, RL10

The University of Texas at Dallas

800 West Campbell Road

Richardson, Texas 75080-3021

This chapter addresses the hydrolytic instability issue of surface chemistry and the repeatability issue of silicon (Si) nanowire (NW) biosensors. Si multi-NWs or nanograting (NG) field-effect transistors (FETs) were fabricated using semiconductor lithographic processing techniques. Then, the NG surfaces were coated with 3-aminopropyltriethoxysilane (APTES) via the vapor- and solution-phase methods. Their performance, including drift, stability, sensitivity, accuracy, and linearity of pH sensing, was evaluated. Sensors treated with both APTES deposition methods exhibit linear pH response with good sensitivity. Devices treated with vapor APTES show better linearity and sensitivity, and APTES-solution-coated devices are more stable with smaller drift. A hydrolysis process was developed to significantly improve the hydrolytic stability of the APTES-coated sensor surface. As a result, an accuracy of ±0.008 pH was achieved, which is comparable to or better than commercially available ion-sensitive FETs (ISFETs), whereas the sensor drift was significantly reduced for both sensors treated with vapor and solution APTES. This hydrolysis process has greatly improved the stability and repeatability of charge sensing of our Si NG bio-FETs.

Pengyuan Zang completed the majority of this work. Yuchen Liang participated in the solution preparation, APTES modification, and pH-sensing experiments.

2.1   Introduction

Driven by the improvement in nanostructure fabrication and characterization technologies, nanoelectronic biosensors have received much attention as a promising approach to detect biological and chemical species, with a variety of applications in disease diagnosis, drug discovery, food safety, etc. [1, 2, 9, 50]. In particular, Si NW FETs have demonstrated potential as a highly sensitive, label-free sensing platform [2, 5, 8, 9, 30, 47, 48]. Advantages include high

sensitivity attributed to the large surface-to-volume ratio and the resulting strong modulation of carrier concentration by the surface charges [1, 24], as well as facility for mass production due to the compatibility with current complementary metal-oxide semiconductor fabrication technologies [5, 8, 51, 52].

For an analog transducer, as the gain improves and the device becomes more sensitive, the output usually becomes less stable, resulting in degraded measurement repeatability and sometimes worse signal-to-noise ratio in real-world performance. The NW FET biosensors are no exception. For example, many published pH-sensing results with NW FET sensors are noisy and unstable in comparison to the conventional ISFETs [5, 8, 24, 30, 50, 53, 54]. This is a critical issue in biosensing; the high sensitivity of NW FETs may be irrelevant because of the poor stability. NW FET biosensors are more sensitive not only to the change of the target analyte but also to every aspect of the biosensing system. These changes may include variations in the devices themselves, usually from the fabrication processes. Si NWs fabricated with bottom-up techniques such as chemical vapor deposition (CVD), though they benefit from the small diameter and smooth surfaces of NWs, have the added difficulty of controlling NW properties and alignment during device integration [2, 30]. In comparison, top-down lithography provides better positioning accuracy as well as flexibility of pattern design [5, 48, 50], and the diameter of the NWs has been improved to be comparable to CVD [55].

Another factor that causes performance variation and instability exclusively in the Si NW FET is the discrete dopant fluctuation [8], a result of low dopant concentration in the NW channel as required by the high sensitivity [5, 24]. This challenge can be overcome by incorporating multiple NW channels in the device design, such as NGFETs [9]. Besides the reduced device-to-

device variation and stability improvement in aqueous solution, Si NG FETs also exhibit performance boosts, including higher current, higher On/Off ratio, lower threshold voltage (VT), and smaller subthreshold swing (SS) [9].

The hydrolytic instability of surface chemistry also significantly affects the stability of NW FET biosensors. Generally, the surface chemistry for NW FET biosensors uses a silane-based self-assembled monolayer (SAM) for sensing pH or as a linker molecule to attach the probe for biomolecule detection. For pH sensing, the unstable reaction of the proton-binding sites on the sensor surface over time can induce drift and hysteresis in the sensor output [38-41]. For biological molecule sensing, the surface chemistry becomes complicated, and the hydrolytic instability issues can be even more significant considering the variation of pH and salt concentrations in the solution as they interact with the SAM and the probes on the surface [8]. In comparison, to the problem of device variation, the SAM hydrolytic instability issue requires significantly more attention because the surface chemistry is much less controllable than the semiconductor fabrication process.

Since the first demonstration in 2001[30], pH sensing with Si NW FETs has been reported by various groups [5, 8, 50, 53], and it is a key tool to verify and evaluate charge-sensing capability, which is fundamental for biological analyte detection. Furthermore, several biosensors and applications, such as the enzyme FET (ENFET) and DNA sequencing, directly rely on the reliable quantification of proton concentration. In ENFETs, the enzyme catalyzes a specific reaction with the target analyte, converting its concentration to a local pH change, which can be detected by NW FETs configured as pH sensors [56]. For DNA sequencing, a proton is released during the reaction of DNA polymerization when the complementary deoxyribonucleotide

triphosphate is introduced. To generate enough protons for a detectable pH change, the reaction usually involves duplicates of the same DNA template by polymerase chain reaction amplification [57]. The reliable and accurate quantification of pH with NW FET biosensors, therefore, possesses appreciable significance in the biosensing field.

In this article, we study the hydrolytic stability of the SAM in pH sensing with different coating methods, as well as how it affects the performance of Si NG FET biosensors. We first fabricated Si NG FETs using lithographic semiconductor processes developed previously [9]. Then, we chemically functionalized the NW surface with the popular APTES as the SAM for our pH-sensing study. APTES has been widely used not only in pH sensing [30, 49, 50] but also as a linker molecule in protein sensing and DNA sequencing [26, 58]. Therefore, the results of this work may be applied beyond pH sensing to other biosensing areas. In comparison to bare Si oxide, adding the surface amino groups from covalently attached APTES yields a linear amphoteric response to pH and results in a linear response to a wide pH range [2, 8, 30, 33].

To functionalize NW surface with APTES, both solution- and vapor-phase deposition processes were used. The solution-phase method is most commonly used in the literature [30, 49, 50], whereas the vapor-phase method can produce better morphology of APTES films [59, 60] due to the absence of excess water and reduced polymerization of APTES molecules [61, 62]. Most previous studies that investigated the surface quality of these two deposition methods [59, 60, 62] focused on surface characterization and analysis. However, the impact of surface modification on the sensor performance still remains largely unknown with these two methods. Very recently, we established processes to coat the device surfaces with APTES via both the vapor- and solution-phase methods [63]. Their pH sensing performance was evaluated and

compared, including hysteresis, linearity and sensitivity. However, there was still notable global

drift in sensor signals for both phases of APTES.

We have achieved significant improvement in the hydrolytic stability and sensing repeatability

through our newly developed hydrolysis process. For the hydrolysis conditions, Etienne and

Walcarius reported that only a strongly acidic environment (pH = 1) is capable of

counterbalancing the basicity of surface amine groups locally confined with a high

concentration, while pure water (floating pH) enables the amine functions to express their total

basic power, resulting in remarkably increased amine liberation in the solution [64].

Nevertheless, we have deliberately chosen de-ionized water as the hydrolysis solution for two

reasons. First, the pH sensor should work stably in an amphoteric range (including pH > 8).

Hydrolysis in acid would have a limited effect in stabilizing the mine-terminated surface in the

basic sensing solutions. Second, the reduction in surface APTES density does not necessarily

affect sensor performance in a negative way. As discussed later in detail, the accuracy of the pH

sensor is actually improved. With the new sensing results after the hydrolysis process, we

demonstrate pH sensing with accuracy comparable to or better than commercially available

ISFETs, as well as excellent repeatability and stability over a long period of time.

2.2   Material and Methods

2.2.1   Fabrication of Si NG FETs

We used Si NG FETs in this study for improved stability and high performance compared to

single-NW FETs. Si NG FETs were fabricated on a Si-on-insulator wafer, consisting of a 70-

nm-thick top Si layer and a 145-nm-thick buried oxide (BOx) layer. The p-type top Si layer had

a low boron concentration of $10^{15}/cm^3$, which was used as the channel doping. Detailed fabrication processes were also reported elsewhere [9]. Device patterns were defined in the top Si layer by photolithography and chlorine plasma etching, including channel area, source/drain (S/D) regions, and leads to contact pads. The S/D junctions were formed by ion implantation with phosphorous ($10^{19}/cm^3$). The NG channels were then patterned by e-beam lithography (EBL) with hydrogen silsesquioxane (HSQ) on a Raith150 Two EBL tool (30 KeV and ~250 pA). HSQ was developed in tetramethyl-ammonium-hydroxide (25 wt. %) heated at 38 °C for 60 s, and the patterns were transferred to the top Si layer by plasma etching. A two-step etch process was used to avoid etching of the BOx layer and floating of the NGs [9]. The NG consists of 100 NWs per device, with each NW of ~ 50 nm in width, ~ 30 nm in height and ~ 20 μm in length. Gate oxide of 3 nm was thermally grown around the NWs after the formation of the NGs. Different from previous devices [9], leads and contact pads were formed from nickel silicide instead of metal to improve the compatibility with oxidizing chemicals from surface modification process.

Silicon nitride (Si_3N_4, 300 nm) was deposited as passivation material on areas other than the NG channel and contact pads. Finally, the devices were annealed in forming gas at 400 °C for 60 min, which reduced surface charges and improved device stability. An electron micrograph of a finished Si NG FET is shown in Figure 2.1a, and the magnified NG region with individual NWs is in Figure 2.1b. All the Si NG FET chips used in this study were fabricated in the same batch on the same wafer to reduce process variations.

2.2.2 Experimental Setup

To isolate all electrical contacts of Si NG FETs from sensing solutions flowing across the NGs, a
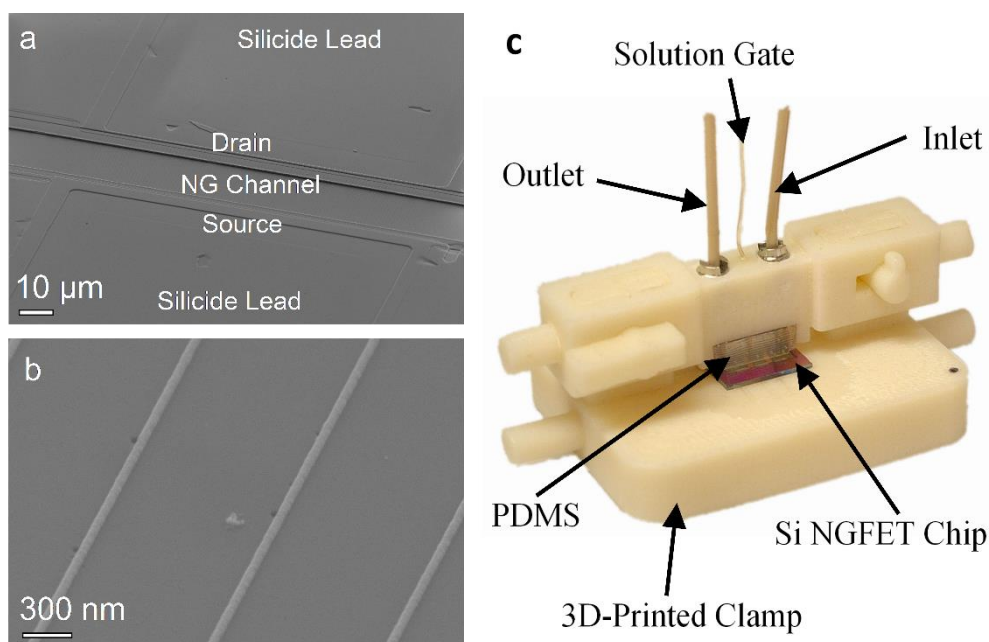
Figure 2.1. The Si NG FET and experimental setup: (a) An electron micrograph of an Si NG FET device. (b) An electron micrograph of the NG region showing individual NWs. Each NW is ~50 nm in width, ~30 nm in height, and ~20 nm in length. (c) A 3-D-printed fluidic clamp for solution delivery and electrical characterization. PDMS: polydimethylsiloxane.

special clamp was designed and made by three-dimensional (3-D) printing, as shown in Figure 2.1c. All S/D contact pads on the chip were designed edgeways for easy probing, away from the central microfluidic channel defined in polydimethylsiloxane (PDMS). This channel was 500 µm in width/height and ~ 1 cm in length, and the two ends were connected to polyetheretherketone tubing as inlet/outlet for the sensing solution. The PDMS channel was sealed on the chip by a top beam, which was locked to the clamp base by two latches. To provide proper gate control of the Si NG FETs, a silver (Ag)/silver chloride (AgCl) wire (< 0.5 mm in diameter) was mounted at the top of the channel as a solution gate. All parts of the clamp were made from ABS plastic, which was not conducting and would not react with the sensing solutions. In the experiment, the clamp was fixed on a probe station (Cascade Microtech) for

S/D probing and gate connection, and a Keithley 4200-SCS device characterization system was used for the electrical measurements. Figure 2.2 shows a schematic of the pH sensing setup (not in scale). With the Ag/AgCl electrode biased at a constant voltage (V_{SG}), the drain current (I_{DS}) of the APTES-modified Si NG FET was measured while flowing different pH solutions across the NG. The source terminal was grounded, and the drain terminal was biased constantly at 0.1 V (V_{DS}).

To reliably deliver sensing solutions to the clamp at a desired flow rate, an air pressure of 2 lbf/in^2 was applied to each of the sealed solution bottles by a peristaltic pump. A selector valve (Valco Instruments) was used to switch between different pH solutions.

Figure 2.2. A schematic of the pH-sensing setup for the APTES-coated Si NG FET.

2.2.3 Surface Modification with APTES

Piranha cleaning (hydrogen peroxide : sulfuric acid = 1 : 3) was performed on the Si NG FET chips for 20 s before both depositions, followed by N_2 drying to remove excess water. APTES (1%, Sigma-Aldrich) in anhydrous ethanol (95%) was used for the solution-phase deposition. The chip was soaked in 25 mL of APTES solution for 30 min. For the vapor-phase deposition, the chip was placed in a closed glass container with 250 µL APTES liquid not in direct contact with the devices, and the container was heated to 100 °C on a hotplate for 35 minutes. After deposition, both chips were rinsed individually with ethanol (four times) and isopropyl alcohol (once) and then dried in a vacuum oven at 120 °C for 60 min.

2.2.4 Solution Preparation for pH Sensing

Phosphate buffer solutions (10 mM) of different pH values containing 100 mM sodium chloride were prepared for pH sensing. The Debye screening length at 100 mM ionic concentration is ~ 1 nm [33], which is larger than the chain length of APTES (~ 5 Å) [62]. The pH of each solution was measured with a pH meter (OAKTON pH 700) before the experiment. The pH range of solutions used in the experiments was approximately 4-9 (before hydrolytic stability improvement) or 2-9 (after hydrolytic stability improvement).

2.2.5 Hydrolytic Stability Improvement

A hydrolysis process was used to improve the hydrolytic stability of the pH sensors. Chips with APTES coating by both solution- and vapor-phase deposition were soaked in deionized water for 12 h, followed by N_2 drying.

2.3   Results

To determine the proper biasing voltage (V_{SG}) for the Si NG FET, the transfer characteristics (I_{DS}

- V_{SG}) of the device were first obtained in the lowest-pH solution. The biasing point was set in

the subthreshold regime for higher signal response (exponential I-V change) compared to the

linear regime (linear I-V change). In the sensing experiment, the drain current (I_{DS}) was recorded

while sweeping a set of different pH solutions (flowing one by one), repeatedly (five or six

times) to evaluate the long-term stability and repeatability. Figure 2.3 shows an example of the
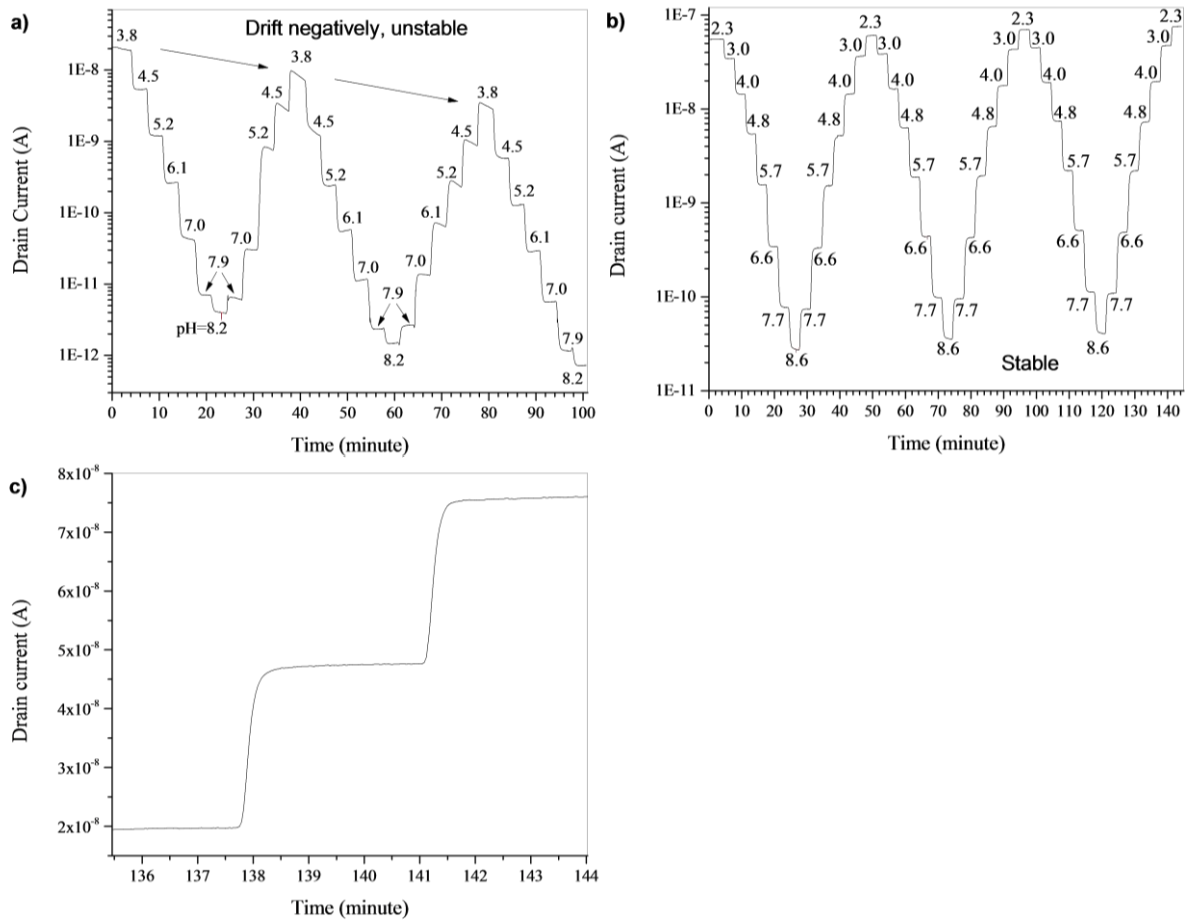
Figure 2.3. The measured drain current (I_{DS}) of the vapor APTES device over time, (a) before and (b) after the hydrolytic stability improvement. (c) is a magnified view of (b). Solutions of different pH levels (labeled inside the plots) were sequentially flowing through the sensor surface, and I_{DS} was measured at the same time.

25

measured drain current for a APTES-vapor-coated chip before and after the hydrolytic stability improvement. The results demonstrate that the simple hydrolysis process can greatly enhance the temporal stability and test repeatability (further discussed in the next section). After the experiment, the current level of each pH was extracted from the measured I_{DS} and converted to relative surface potential (Ψ_0) using the measured transfer characteristics. The potential of the first data point at the lowest pH was set as a reference ($\Psi_0 = 0$ V). This conversion to surface potential eliminates the effects of device variation, i.e., the converted results were irrelevant of the device performance and only depended on surface properties, allowing us to focus on the difference of pH response induced by the APTES coating. In addition, the converted voltage response to pH can faithfully reflect the linear correlation between surface potential and pH. Therefore, for each sweep of the set of different pH solutions, a linear fit was performed to quantify the linearity of pH response.

2.3.1 Before Hydrolytic Stability Improvement

Figure 2.4a and c shows the transfer characteristics of n-type Si NG FETs modified in APTES-ethanol solution and via APTES vapor, respectively, before the hydrolytic stability improvement. The tests were performed in low pH solutions (4.1 for ethanol and 3.8 for vapor), and V_{DS} was set to be 0.1 V. Both devices modified in ethanol and vapor demonstrated excellent performance, with small SS of 64 and 69 mV/Dec and six orders of magnitude for the on/off ratio. A major difference between them is the threshold voltage (V_T): V_T of the device treated with ethanol is 0.416 V, which is 0.25 V smaller. This V_T difference is not caused by the variation of device fabrication, as the V_T variation range of bare devices before functionalization is normally within 15 mV [9]. It is likely due to the higher density of positively charged APTES attached to the
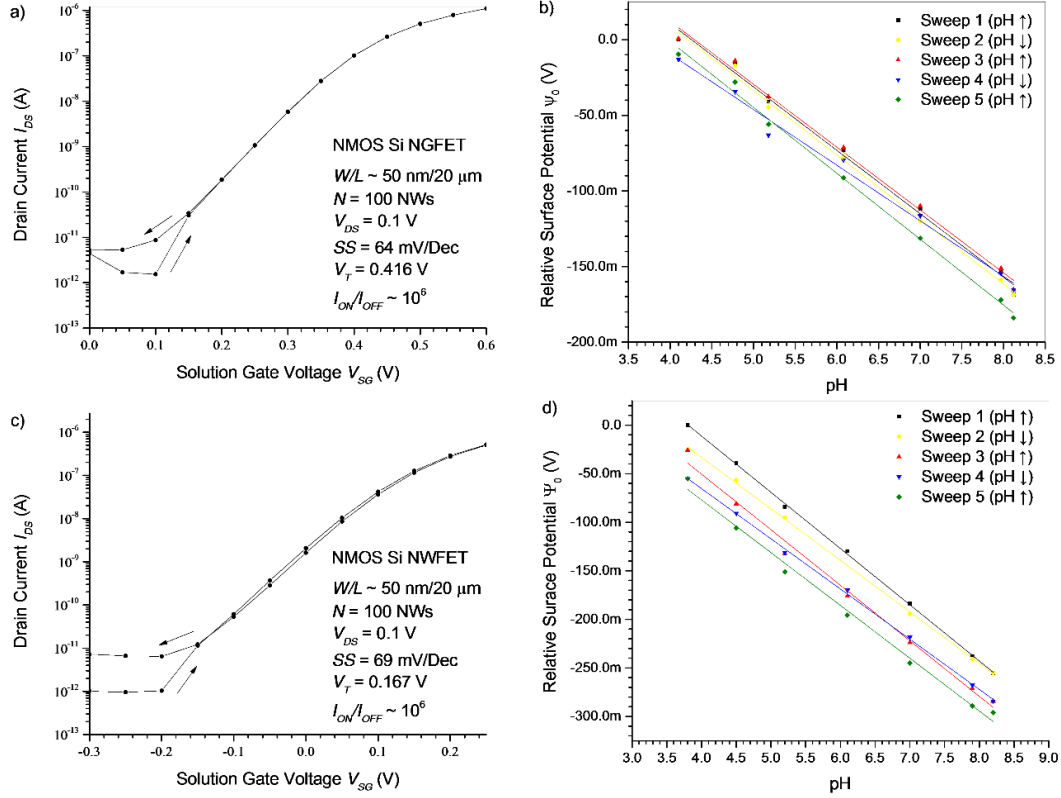
Figure 2.4. Test results of the APTES-modified Si NGFETs before the hydrolytic stability improvement process. Test results of the APTES-modified Si NG FETs before the hydrolytic stability improvement process: (a) and (b) the devices modified in ethanol and (c) and (d) the devices modified in vapor. The results include transfer characteristics (I_{DS} - V_{SG}) in (a) and (c) and the pH-sensing results (Ψ_0 – pH) in (b) and (d).

gate oxide surface during the vapor phase deposition, which equivalently shifts the transfer

characteristics in the negative direction.

Because of the difference in V_T, the V_{SG} biasing points for pH sensing were set differently (0.4 V

for the ethanol device and 0.15 V for the vapor device). Figure 2.4b and d shows the pH

responses of devices with APTES deposited in ethanol solution and in vapor, respectively. In

both experiments, five pH sweeps with the same range from pH 4 to 9 were performed in total,

starting from the lowest-pH solution.

2.3.2　After Hydrolytic Stability Improvement

Figure 2.5a and c shows the transfer characteristics of n-type Si NG FETs, modified in the APTES-ethanol solution and via APTES vapor, respectively, after hydrolytic stability improvement. Both tests were performed in a solution of pH 2.3, and V_{DS} was set to be 0.1 V. Compared to the device (Figure 2.4a) before hydrolysis, the ethanol device showed a slightly larger SS of 71 mV/Dec, a larger V_T of 0.464 V, and the same six orders of magnitude for the on/off ratio. Similarly, the vapor device also showed a lightly larger SS of 74 mV/Dec, a much
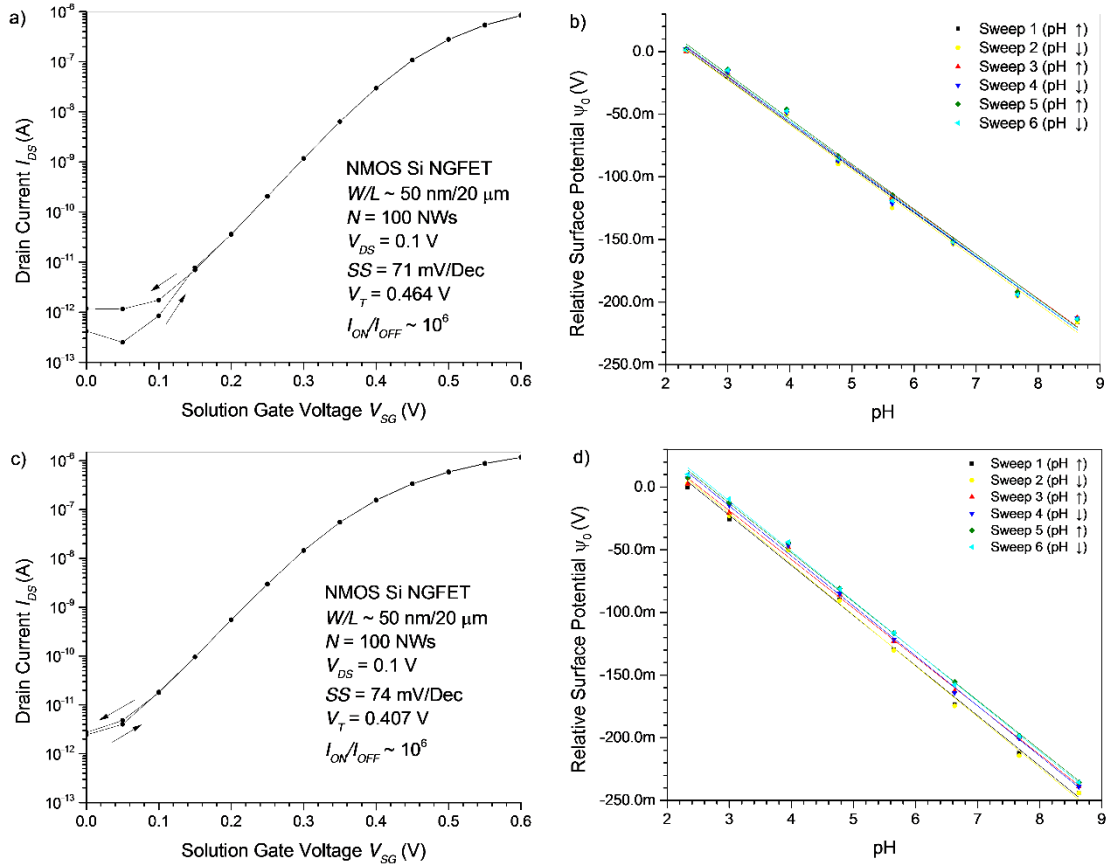
Figure 2.5. Test results of the APTES-modified Si NG FETs after the hydrolytic stability improvement process: (a) and (b) the devices modified in ethanol and (c) and (d) the devices modified in vapor. The results include transfer characteristics (I_{DS} - V_{SG}) in (a) and (c) and the pH-sensing results (Ψ_0 – pH) in (b) and (d).

28

larger V_T of 0.407 V (0.24-V increase from the original device before hydrolysis), and the same

on/off ratio. Figure 2.5b and d shows the pH responses of the NG FET with APTES deposited in

ethanol and in vapor, respectively, after hydrolytic stability improvement. In both experiments,

six pH sweeps ranging from pH 2 to 9 were performed, starting from the lowest-pH solution. The

V_{SG} biasing point was set at 0.45 V for the ethanol device and 0.35 V for the vapor device. The

increase of V_T of the vapor device after the hydrolysis process suggests that the density of

APTES attached to the oxide surface is reduced by the hydrolysis process in two possible ways.

First, covalently attached APTES can be partially removed during the hydrolysis process, as the

amine functionality is able to catalyze the hydrolysis of the attached APTES molecules both

inter- and intramolecularly [62]. Second, the weakly attached APTES molecules through

hydrogen bonding can also be removed after hydrolysis, as the high molecular mobility in

solution during soaking can disrupt hydrogen bonds more effectively [62]. Similarly, studies

have shown that rinsing the surface after silanization facilitates the displacement of weakly

bonded silane molecules [8, 62].

To better understand this APTES-removal process during hydrolysis, we like to refer back to the

pH-sensing experiments of the vapor device without the hydrolysis process, as shown in Figure

2.3a and Figure 2.4d. In this experiment, the vapor device was rinsed for about 2 h during the pH

sensing. The global negative drifting of the drain current across the five pH sweeps as illustrated

in Figure 2.3a is a direct result of the gradual removal of positively charged APTES during pH

sensing.

2.4   Discussions

To evaluate and compare the hydrolytic stability as well as the performance of Si NG FETs

modified by APTES via the vapor- and solution-phase methods, before and after hydrolytic stability improvement, the results were further analyzed and discussed in terms of drift and stability, sensitivity, accuracy, and linearity.

2.4.1 Drift and Stability

Figure 2.3a shows significant drift of sensor output for the same pH measured repeatedly over time. This drift will cause poor repeatability of the pH sensor, which must be constantly corrected by calibration. Figure 2.6a and b shows the averaged relative surface potential (Ψ_0) versus pH for both ethanol (red) and vapor (black) APTES coated devices, before and after hydrolytic stability improvement. The data points represent the mean of Ψ_0, while the error bars represent the standard deviations of Ψ_0 for each pH. The wider error bars of vapor compared to ethanol APTES-coated devices before hydrolysis (~ 50 mV versus ~ 17 mV) indicated larger drift and, therefore, worse stability of vapor APTES, possibly due to the high density of weakly bond APTES molecules formed during the vapor phase deposition. However, after hydrolysis, both types of devices showed significant stability improvement, as illustrated by the large decrease of error bars from ~50 mV down to ~ 13 mV for the vapor device and from ~17 mV down to ~ 5 mV for the ethanol device, as shown in Figure 2.6b. Such a large improvement of hydrolytic stability is direct proof that hydrolysis is capable of removing weakly bound APTES that could be in the form of oligomers or polymers as suggested in [62]. As a result, the APTES-coated NG FET after hydrolysis has shown excellent long-term stability and repeatability in pH sensing, as shown in Figure 2.3b compared to Figure 2.3a before the hydrolysis. The reduction of drift can be better viewed in the magnified Figure 2.3c. We believe this hydrolysis improvement

method can be useful in the development and application of practical biosensor because it

significantly mitigate the fundamental issue of surface stability and reliability.
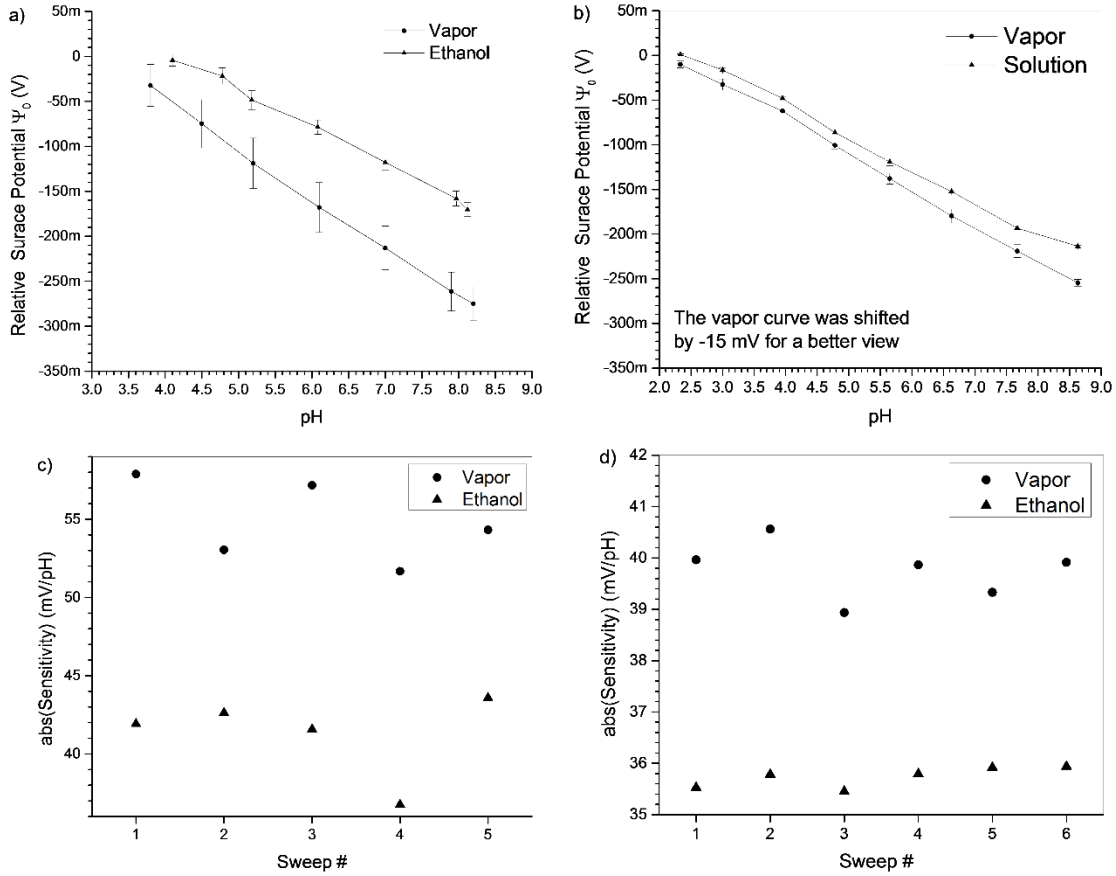
Figure 2.6. A comparison of the drift and sensitivity of APTES-coated NG FET devices for pH sensing: (a) and (c) before and (b) and (d) after the hydrolytic stability improvement step

2.4.2   Sensitivity and Accuracy

The pH sensitivity of an ISFET is generally defined as [11]:

$$\partial \Psi_0 / \partial pH_B = -2.3\alpha kT/q, \tag{2.1}$$

with

$$1/\alpha = 1 + 2.3kTC_{dif}/q^2\beta_{int}. \tag{2.2}$$

It depends mainly on the surface properties instead of device working conditions, as the differential double-layer capacitance C_{dif} and the intrinsic buffer capacity β_{int} are strongly related to oxide-electrolyte interface. With the absolute temperature T, Boltzmann constant k and electron charge q, α is a dimensionless parameter varying between zero and one. At room temperature ($T = 300$ K), the maximum achievable sensitivity known as the Nernstian sensitivity can be calculated as 59.5 mV/pH, by setting $\alpha = 1$.

Figure 2.6c and d show the absolute values of sensitivity for both ethanol and vapor APTES-coated devices extracted from the slopes of linear fits for each pH sweep, before and after the hydrolytic stability improvement. Before the hydrolysis, vapor APTES exhibited sensitivity close to the Nernstian limit (54.82 ± 2.66 mV/pH, in the format of average ± standard deviation), which is much higher than that of ethanol APTES (41.30 ± 2.65 mV/pH). However, both sensitivities decreased after hydrolysis [by ~ 31% (vapor) and ~ 14% (ethanol)]. The vapor APTES device still slightly out-performed ethanol device (39.76 ± 0.56 mV/pH versus 35.74 ± 0.20 mV/pH). More importantly, their varying ranges (the standard deviation) were greatly reduced after hydrolysis due to more hydrolytically stable surfaces. The reduction of sensitivity is a consequence of reduced surface APTES density. From the perspective of SAM quality, this is a valid conclusion based on the results.

Intuitively, one may assume that the reduced surface APTES density has a negative impact on the sensor performance due to the decreased sensitivity. Quite the contrary, the accuracy of the pH sensors has actually improved, due to the resulting stability improvement. To be more specific, the fluctuation of the pH sensitivity (4.8% for vapor and 6.4% for ethanol) was greatly reduced after the hydrolysis process (1.4% for vapor and 0.6% for ethanol). Assuming we

calibrate our pH sensors with standard calibration solutions of pH 4, 7, and 10, the maximum

offset from the calibration points is 1.5 pH. With the most stable pH sensor from our results

(ethanol, after hydrolysis), the best accuracy we have achieved is ±0.008 pH. This pH-sensing

accuracy is comparable to (Sentron ± 0.01pH) or better than (ISFETCOM Co., Ltd. ± 0.02 pH)

the ISFETs (not NW FETs) commercially available. Therefore, despite the reduction of the

APTES surface density and the pH sensitivity after the hydrolysis process, the accuracy of the

pH sensor has greatly improved.

2.4.3   Linearity

Table 2.1. Coefficient of Determination (R^2)

APTES-Modified Si NG FET	Before Hydrolysis		After Hydrolysis	
	Mean	Standard Deviation	Mean	Standard Deviation
Vapor	0.99677	0.00361	0.99746	0.00120
Ethanol	0.99444	0.00249	0.99516	0.00111

The calculation was based on five pH sweeps (before hydrolysis) or six pH sweeps (after hydrolysis).

Linearity characterizes the deviation of pH response from a linear relation and can be quantified

by the coefficient of determination (R^2). Unlike previous studies that assessed the overall

linearity in the form of conductance determined by both the device performance and the SAM

quality [2, 30, 33, 50], relative surface potential (Ψ_0) was used in this study, reflecting only the

qualities of APTES and other surface species and excluding effects from device variation. R^2 of

each linear fit (for each pH sweep) in all four experiments were extracted, and the mean/standard

deviations were calculated for each experiment, as shown in Table 2.1. The vapor-phase

APTES-coated device exhibited slightly better linearity of pH sensing compared to the device

with APTES deposited in ethanol (higher mean of R^2 closer to 1), yet the standard deviation was larger. After the hydrolysis, both the linearity and standard deviation significantly improved for APTES deposited in both methods. The weakly bonded APTES deposited in vapor was unstable in the first pH-sensing experiment (before hydrolysis), which yielded a 45% higher standard deviation (0.00361 versus 0.00249) compared to the ethanol APTES. After hydrolysis, most of the unstable APTES molecules from vapor deposition (attached via hydrogen bond) were removed, resulting in a comparable standard deviation to ethanol APTES (0.00120 and 0.00111). This observation is in good agreement with previous analyses of results. The 55% decrease of the standard deviation of the ethanol APTES after hydrolysis indicated that surface rinsing of even 6,000 s in pH sensing was not enough to completely remove the loosely attached APTES, which required a sufficiently long hydrolysis process. However, from a practical point of view, both APTES deposition methods, even before hydrolysis, showed good linearity ($R^2 > 0.99$) with well-controlled standard deviation (< 0.005) of minor differences. Importantly, the hydrolysis process is found to stabilize surface-charge species, resulting in the notable decrease in standard deviation (67% reduction for vapor and 55% reduction for ethanol).

2.5   Conclusions

In summary, pH-sensing performance was compared between Si NG FETs coated with vapor- and solution-phase APTES, and a hydrolysis process was developed to improve hydrolytic stability of surface APTES in pH sensing. Devices with both APTES deposition methods exhibited linear pH response with good sensitivity. Vapor APTES showed better linearity and sensitivity than ethanol APTES, yet surface stability in terms of drift was better in the latter. The hydrolysis process was demonstrated to significantly improve surface stability from reduced drift

34

in pH sensing on both vapor and ethanol APTES sensors and to greatly enhance the accuracy down to ±0.008 pH, which is comparable to or better than commercially available ISFETs. This process was believed to remove weakly bound APTES molecules from the surface, therefore stabilizing the surface-charge species that are sensitive to pH change.

2.6 Acknowledgments

CHAPTER 3

NOISE SUPPRESSION WITH ADDITIONAL REFERENCE ELECTRODE FOR TIME-DEPENDENT PROTEIN SENSING TESTS WITH SI NANOGRATING FETS[2]

Authors – Pengyuan Zang, Silu Zhang, Yuchen Liang, and Walter Hu

The Department of Electrical Engineering, RL10

The University of Texas at Dallas

800 West Campbell Road

Richardson, Texas 75080-3021

We propose a method to suppress the electrolyte potential noise in time-dependent protein sensing tests with an additional reference electrode, which doesn't have the challenging requirements as for the reference FET (REFET). The noise is recorded by the additional electrode and then suppressed in the sensing results. This noise is likely due to the electrochemical reaction at the electrolyte – solution gate interface. Results suggest increased readability with reduced signal level variation and increased credibility. The limit of detection (LOD) decreases by 50% ~ 70%.

Pengyuan Zang completed the majority of this work including the design and fabrication of the biosensing clamp with dual electrodes, the protein sensing experiments with this clamp, data analysis, and writing of the manuscript. The antibody-protein chemistry used in this work was developed by Silu Zhang.

3.1 Introduction

Over the past few decades, the development and improvement in nanoelectronic biosensors have made them promising candidates in the applications of disease diagnose, new drug discovery, health care, etc. Emerging among them are the Si nanowires (SiNWs) biologically-sensitive field effect transistors (bio-FETs), which has demonstrated great potential as ultrasensitive, label-free, rapid and miniature electronic sensors to detect chemical and biological species [2, 11, 65]. In certain applications such as protein sensing where the analyte concentration is extremely low (~ fM), enhanced sensitivity is preferred, which can be achieved in the form of exponential gain by biasing the bioFET in the subthreshold regime [24]. However, while benefiting from the high sensitivity, the noise in the electrolyte potential, which is amplified along with the small analyte signals to detect, also starts to emerge as a problem.
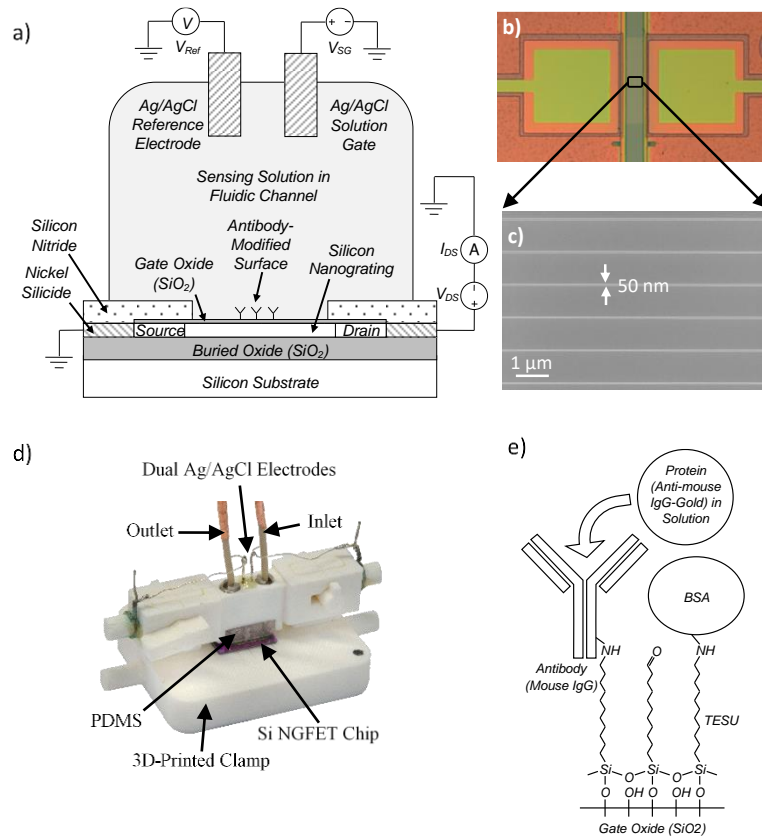
Figure 3.1. a) Schematic of protein sensing with a Si nanograting FET (NGFET) and dual Ag/AgCl electrodes.The oxide-electrolyte surface of the nanograting is functionalized with antibody. The FET is biased in subthreshold region by a solution gate at the top of the fluidic channel. The other electrode monitors the bulk solution potential. b) Optical image and c) electron micrograph of a typical Si NGFET with 100 nanowires in the grating. Each nanowire is of 50 nm in width, 30 nm in height and 20 µm in length. d) 3D-printed clamp for protein sensing with dual Ag/AgCl electrodes. e) Species at the gate oxide surface after modification with TESU, antibody (mouse IgG) and passivation (with BSA). The corresponding antigen used in this study is anti-mouse IgG with gold.

A widely accepted solution is to incorporate a second reference FET (REFET), which doesn't respond to the analyte to be detected [11]. Differential measurement is applied between the bioFET and REFET, eliminating the effects of unstable electrode/electrolyte potential which appears as a common signal in the output of both FETs. A well-known example is the direct detection of penicillin with enzymatically modified ion-sensitive FET (ISFET) by Caras and

Janata [42]. Nevertheless, a few challenges still remain regarding the REFET. First, the

differential measurement requires that the REFET is electrically identical to the bioFET [11].

Second, the REFET requires careful surface modification in order to stay chemically inert to the

analyte, while at the same time equally sensitive as the bioFET to other electrolyte changes (e.g.,

ionic strength, pH and temperature) [66]. In this study, we investigated a different approach.

Instead of a second FET, we used a second electrode to monitor and suppress the electrolyte

potential noise. In comparison to REFET, the second electrode is easier to make, reduces overall

system complexity, and doesn't have the challenging requirements as for the REFETs. This

approach was studied in the time-dependent protein sensing tests of our interest. The additional-

electrode measurement scheme with ISFET has been reported before in transfer-characteristics-

based tests [67], but to our best knowledge, time-dependent sensing test has not yet been

reported, nor has the noise suppression method proposed in this study.

3.2   Experimental

3.2.1   Device Fabrication and Experimental Setup

Si nanograting FETs (NGFETs) each with 100 nanowires were used for the improved reliability

and uniformity [9]. Detailed fabrication process has been reported previously [9, 63]. Figure

3.1a illustrates the schematic of protein sensing setup with a Si NGFET and dual Ag/AgCl

electrodes. The Si NGFETs were fabricated on a silicon-on-insulator (SOI) wafer with top-down

e-beam lithography (nanograting channel) and photolithography (S/D pads, leads, probe pads,

etc.). Each nanowire in the grating channel is ~ 50 nm in width, 30 nm in height and 20 µm in

length. The nanograting channel has a low boron concentration of $10^{15}/cm^3$ from the substrate

doping, and the source/drain junctions were highly doped with phosphorous by ion implantation. The electric connections were made from nickel silicide, and a silicon nitride layer was deposited on top to provide insulation and protection. Figure 3.1b and Figure 3.1c show an optical image of a typical Si NGFET and an electron micrograph of the nanograting.

Figure 3.1d shows an image of the 3D-printed sensing clamp. A fluidic channel (500 µm in both width and height) defined in polydimethylsiloxane (PDMS) was connected to a pair of inlet/outlet for solution delivery, and sealed on the Si NGFET chip by the sensing clamp. Two identical Ag/AgCl electrodes were mounted at the top of the fluidic channel, one as the solution gate (that sets the electrolyte potential) and one as the reference electrode (to monitor the electrolyte potential). The source/drain probe pads were located near the chip edges and could be easily probed.

3.2.2 Gate Oxide Surface Modification

The dual-electrode setup was utilized in time-dependent protein sensing tests, and for this purpose the channel gate oxide surface was modified with antibody. Figure 3.1e shows the surface species after the modification. Bare SiO_2 gate surface was first cleaned in Piranha solution (sulfuric acid : hydrogen peroxide = 3 : 1) for 30 seconds, converting surface siloxane bonds to hydroxyl groups. After that, 0.1% 11-triethoxysilylundecanal (TESU) in toluene was applied to the chip for 5 hours, forming self-assembled monolayer (SAM) on the surface. The chip was then treated with 50 µg/mL mouse IgG (dissolved in 2 mM KPB with $NaCNBH_3$ as reducing agent) for 3 hours. Finally, the chip was treated similarly with ethanolamine or bovine serum albumin (BSA) for 3 hours to passivate the remaining unreacted aldehyde groups on TESU.

3.2.3   Sensing Solution Preparation

Table 3.1. Solutions for a Sample Test

Solution	Protein Concentration	BSA (w/v)	pH	Conductivity
PBS	None	0%	7.14	204 µS/cm
PBS with BSA	None	0.01%	7.14	207 µS/cm
Protein 1	1 pM	0.01%	7.15	208 µS/cm
Protein 2	10 pM	0.01%	7.13	210 µS/cm
Protein 3	100 pM	0.011%	7.12	228 µS/cm

Anti-mouse IgG with gold was used as the analyte or target protein to be detected. The

antibody-antigen binding was verified in separate control tests with scanning electron

microscopy (SEM). Protein solutions were prepared by cascade dilution in PBS (with salt

concentration ~ mM level). Because the stock protein solution also contains BSA, extra BSA

was added to equalize the BSA concentration in all protein solutions. Two PBS buffer solutions

were prepared, one with added BSA and one without. To minimize the effects from changes in

pH, ionic strength and temperature, the pH and conductivity of all solutions were measured and

adjusted, and all solutions were stored under the same condition. Table 3.1 lists the solutions

prepared for a sample protein sensing test. The details of protein sensing is not further discussed

here because the mV range of signal induced by pH variance is still comparable to protein signal,

and therefore the repeatability of results is being studied and verified.

3.3   Results

To understand and take advantage of the additional electrode in the noise suppression, data from

a sample test (with solutions as shown in Table 3.1) are presented in this section. First, the

transfer characteristics of the Si NGFET were extracted to determine the appropriate biasing

point of solution gate (V_{SG}) in the subthreshold region. Then, the time-dependent protein flow

test was performed. The results are discussed in the next section.

3.3.1   Transfer Characteristics ($I_{DS} – V_{SG}$ and V_{Ref})

Antibody-modified n-channel Si NGFETs were biased with $V_{DS} = 0.1$ V and source terminal

grounded. A bidirectional voltage sweep was performed on the solution gate and the drain

current was measured, covering the regions of accumulation, depletion (subthreshold) and

inversion in the transfer characteristics. Within the subthreshold region, the biasing point of the

solution gate (V_{SG}) was determined and later used in the time-dependent sensing test. The

reference electrode was configured as zero current (actual current $<$ fA), and its voltage (V_{Ref})

was recorded at the same time. Figure 3.2 shows the transfer characteristics for the sample test,
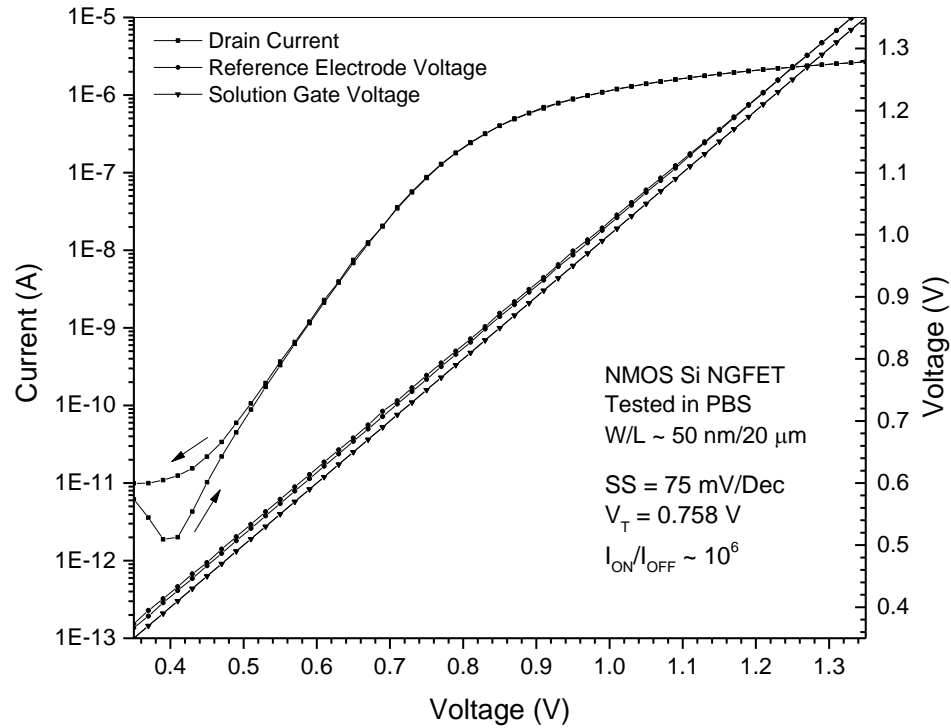
Figure 3.2. Transfer characteristics ($I_{DS} – V_{SG}$) and reference electrode voltage (V_{Ref}) by the Si NGFET modified with TESU and mouse IgG, tested in 2 mM PBS

in 2 mM PBS. The sensor performed well with zero hysteresis, good subthreshold swing (SS) of

75 mV/Dec and large on/off ratio of 6 orders of magnitude. V_{SG} was chosen to be 0.62 V for the

time-dependent test. V_{Ref} followed well the sweeping voltage of solution gate with a nearly

constant voltage gap ($\sim$ 20 mV), indicating that the reference electrode was reflecting the bulk

solution potential set by the solution gate.

3.3.2   Time-Dependent Protein Flow Sensing Test ($I_{DS} - t$)

The Si NGFETs were biased and operated under similar conditions as the transfer characteristics

test, with the exception that the solution gate was biased at the constant voltage of pre-

determined V_{SG}. As a time-dependent measurement, different sensing solutions were delivered to

the sensor in a flowing state during different time windows. Besides the drain current, V_{Ref} was
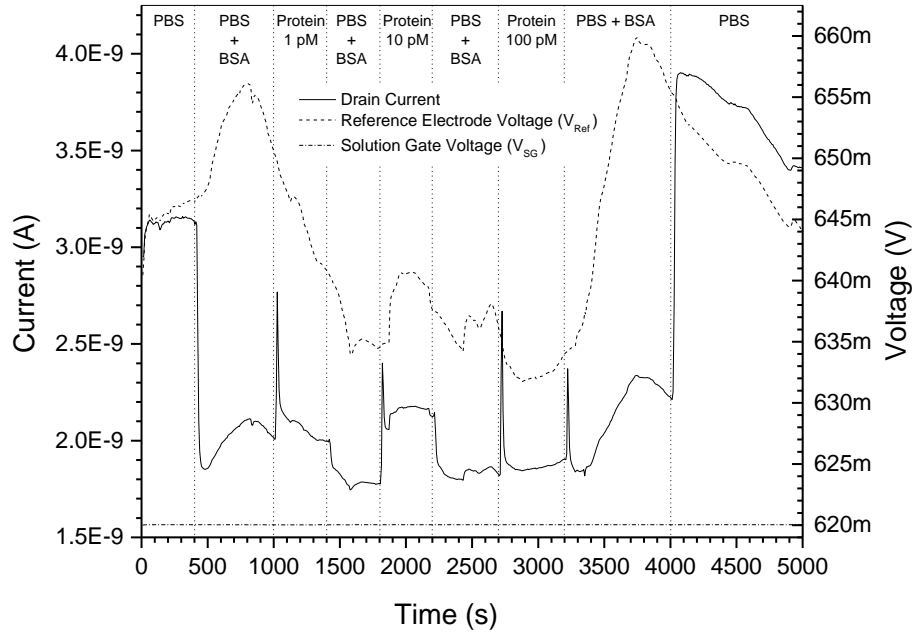
Figure 3.3. Time-dependent measurement of drain current (I_D - t) and reference electrode voltage
(V_{Ref} - t), for different sensing solutions. The actual solution gate voltage (VSG) is also recorded.

43

also recorded during the whole test. Figure 3.3 illustrates the time-dependent sensing results of the sample test (with solutions in Table 3.1), including totally 9 time windows. Baseline solutions were tested before and after each protein solution of different concentrations. Applied V_{SG} was also measured at the same time which stayed perfectly constant ($\Delta V_{SG} < 10$ µV).

3.4 Discussion

Prior to any formal discussion of the results, a key assumption must be clearly stated. At the electrolyte – reference electrode interface, the bulk solution potential U_{Sol} and reference electrode voltage V_{Ref} are related as

$$U_{Sol} = V_{Ref} + \Psi_{Ref}, \tag{3.1}$$

in which Ψ_{Ref} represents the surface potential at the electrode – electrolyte interface. As the reference electrode was configured as zero current, there should be no electrochemical reaction at the interface that gave rise to any change in Ψ_{Ref}. On the other hand, the pH and conductivity of all sensing solutions were controlled, and thus unable to cause change in Ψ_{Ref}. Therefore, we assume that Ψ_{Ref} was constant during the tests, which suggests that the change in V_{Ref} truly reflects the change in U_{Sol}.

In the following context, first the electrolyte potential noise in the results is discussed. Then a method to suppress the noise is presented, based on the discussion.

3.4.1 The Electrolyte Potential Noise

Results in Figure 3.3 suggest that despite the constant V_{SG} applied to the solutions, V_{Ref} varied dramatically (~ 30 mV) during the test. To understand this noise, we apply similar analysis to

44

the electrolyte – solution gate interface:

$$U_{Sol} = V_{SG} + \Psi_{SG}, \tag{3.2}$$

in which Ψ_{SG} is the surface potential at the solution gate. Similar to the reference electrode, pH or conductivity weren't the cause of this noise. However, there was current (> 0.1 nA) flowing across the solution gate – electrolyte interface, which was necessary to maintain the constant V_{SG}. Because the charge carriers in electrode (electrons) and electrolyte (ions) are inherently different, this current is a sign of electrochemical reactions at the interface, which enabled the conversion between the different carrier types. Combining (3.1) and (3.2):

$$V_{Ref} + \Psi_{Ref} = U_{Sol} = V_{SG} + \Psi_{SG}, \tag{3.3}$$

since Ψ_{Ref} and V_{SG} are constant, the observed noise on V_{Ref} can be attributed to Ψ_{SG} and is very likely due to the electrochemical reactions at the electrolyte – solution gate interface. Another clue is the tiny hysteresis of V_{Ref} in Figure 3.2, which indicates that Ψ_{SG} changed slightly when the solution gate voltage swept back.

As shown in Figure 3.3, the remarkable resemblance of drain current (I_{DS}) to V_{Ref} in shape indicates that I_{DS} was also affected by the same noise. This is not surprising, as the solution gate biased the Si NGFET via the electrolyte, and its potential U_{Sol} was directly perceived by the sensor.

3.4.2 Noise Suppression with V_{Ref}

The advantage of the additional electrode is that V_{Ref} can be used to suppress the same noise present in I_{DS}, which will be used for protein signal analysis. From (3.3) we can write

$$\Delta V_{Ref} = \Delta U_{Sol} = \Delta \Psi_{SG}. \tag{3.4}$$

Notice that V_{Ref} (V) and I_{DS} (A) have different units, so the first step is unit conversion. Since I_{DS} responds exponentially to the channel surface potential Ψ_0, it's preferred to convert the former to the latter which changes linearly, for the simplicity of data manipulation in future steps. For the sample test, the measured $V_{Ref} - I_{DS}$ relation from Figure 3.2 is used for the conversion and the resulting Ψ_0 is plotted in the upper graph of Figure 3.4. Because only the relative change of surface potential matters, the starting point of Ψ_0 is set as the reference point (zero point). Also plotted on the same graph is the scaled ΔV_{Ref} (relative to the starting point as well), or V_{Noise}. The reason for the scaling is that the noise amplitude of V_{Ref} is greater than that of Ψ_0. Although U_{Sol} stays constant for its DC component in the bulk solution, ΔU_{Sol} may not as the AC components
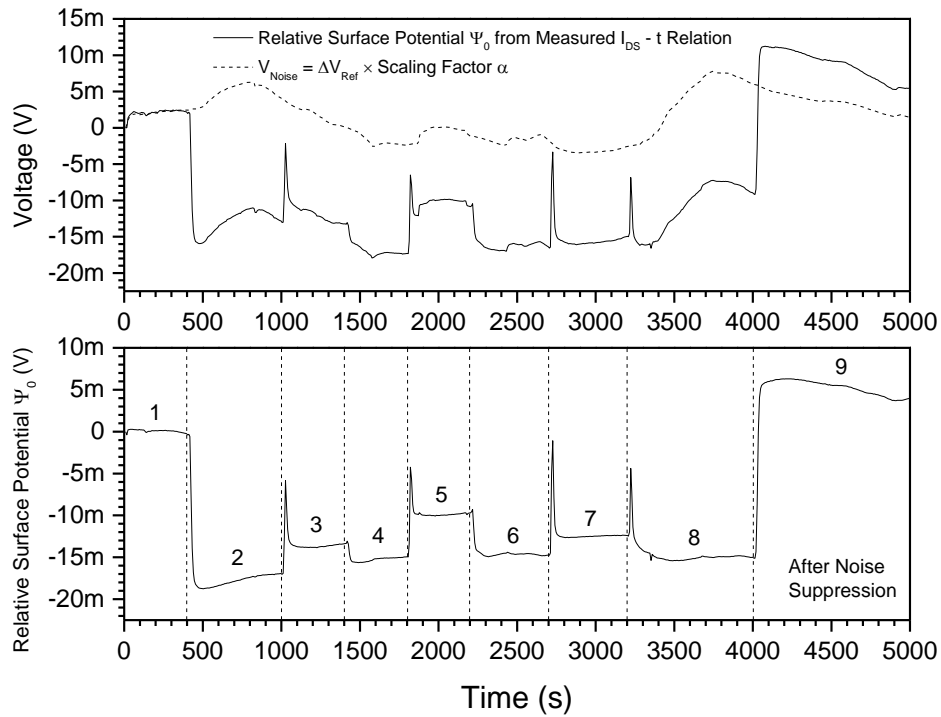
Figure 3.4. Noise suppression for the sample test results in Figure 3.3. The relative surface potential and scaled VRef are plotted in the upper graph, with $\alpha = 0.4$. The lower graph shows the results after noise suppression, with the time windows labeled.

will attenuate during propagation in the solution. As a result, ΔU_{Sol} seen by the reference electrode and the sensor may have attenuated differently, depending on their locations relative to the solution gate. This is the reason that a scaling factor α of 0.4 is applied to ΔV_{Ref} in Figure 3.4, which, at this moment, can only be determined empirically. Finally, the noise signal V_{Noise} is subtracted from Ψ_0, and the result is plotted on the lower graph of Figure 3.4, with labeled time windows. Compared to the one without the noise suppression, this result is more readable, and more credible as explained below.

Figure 3.5 illustrates the averaged signal level and standard deviation (as error bar) of Ψ_0 within each time window, before and after the noise suppression. One prominent improvement after the noise suppression is that the error bars shrink dramatically, indicating a huge decrease in noise level. The second improvement is that all signal levels of PBS with BSA (even window #s) are closer to each other, which increases the credibility of this result, as ideally these levels should be the same. In Figure 3.6, the average standard deviation of Ψ_0 for this test is calculated, before and after the noise suppression, together with results from two other tests. These results show 50% ~ 70% decrease in the average standard deviation. The resolution for a biosensor can be defined as the smallest detectable change of analyte (protein) concentration with a reasonable certainty [68]. Practically, setting three times of standard deviation as the resolution yields a confidence level of 99.86%. Despite the lack of improvement in protein sensitivity due to unaltered relative difference between signal levels, results in Figure 3.6 suggest the resolution of the Si NGFET protein sensors has improved (decreased) by 50% ~ 70% after the noise suppression.
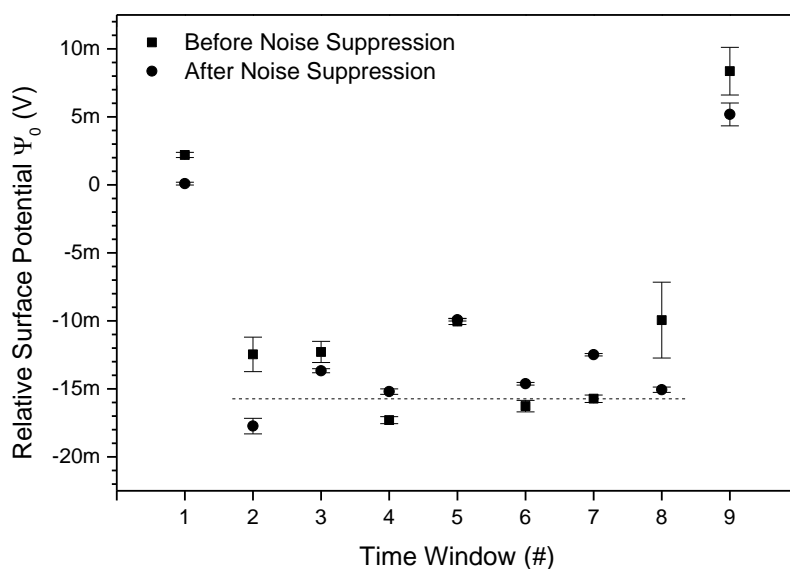
Figure 3.5. Average signal level and standard deviation (error bar) of Ψ_0 (the sample test) within each time windows, before and after noise suppression
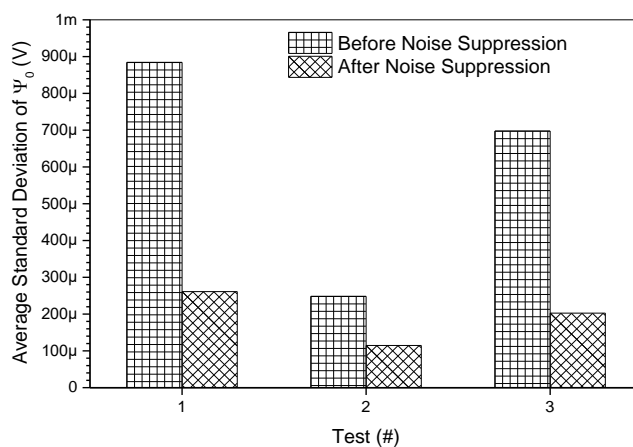
Figure 3.6. Average standard deviation of Ψ_0 for the sample test (test 1) and two other tests, before and after noise suppression

3.5   Conclusion

In summary, we propose a method to suppress the electrolyte potential noise in time-dependent

protein sensing tests with an additional reference electrode. This noise is likely due to the

electrochemical reaction at the electrolyte – solution gate interface, implied by the solution gate

current. Results after the noise suppression suggest increased readability with reduced signal level variation as well as increased credibility. The resolution improves by 50% ~ 70% as confirmed by several test results.

3.6   Acknowledgments

CHAPTER 4

IMPACT OF SURFACE CHARGE BUFFER ON BIOLOGICAL FIELD EFFECT TRANSISTORS

We propose a site-binding model for biological field effect transistors (BioFETs), to study how the protonation and deprotonation of the surface hydroxyl groups affect the analyte detection sensitivity. Analytical studies were performed to investigate the effect of buffer capacity from various surface species on the analyte sensitivity, which were verified by numerical simulation. The results suggest that large buffer capacity of proton from the high density of surface hydroxyl groups is beneficial for pH sensing. However, it is undesirable for the detection of non-proton analytes. Coupled by the surface potential, the capture of the charged analytes on the BioFET surface will rebalance the protonation and deprotonation of surface hydroxyl groups in the opposing direction, effectively compensating and buffering the charges from the analyte. Therefore, a low proton sensitivity from the surface hydroxyl groups is the prerequisite for analyte detection. On the other hand, the analyte sensitivity is also determined by the buffer capacity of the analytes from the surface probes. A high analyte buffer capacity requires both high density of surface probes, as well as the surface analyte concentration at close range to the equilibrium dissociation constant. For charge-based analyte detection with BioFETs, this work can be useful in the evaluation of the charge buffering effect on analyte detection by the surface hydroxyl groups.

Keywords: Charge Buffer; Buffer Capacity; Field Effect Transistor; Biosensor;

4.1 Introduction

ISFETs and other affinity-based Bio-FETs have received much attention in the biosensor community, due to their great potential as highly-sensitive, label free and real-time biosensing platform [2-4, 6, 69]. They all utilize FET as the transducer to covert the charge carried by the ion or molecule of interest into an electric signal. To selectively detect a type of ions or biomolecules, the sensing membrane (typically the gate oxide) is modified with a linker or probe that specifically react with the target analyte [13]. Common materials for the sensing membrane include silicon dioxide, silicon nitride, aluminum oxide, hafnium oxide, as well as other metal oxides [27, 43, 44]. The high density of hydroxyl groups on many oxide surfaces react with protons in aqueous solutions through protonation and deprotonation, and this change of surface charge states makes most of these oxides naturally pH-sensitive. However, if the target analyte is other than proton and reacts with separate probes modified on the oxide surface, the intrinsic proton – hydroxyl group reaction will compensate and buffer the change of charge state due to the probe-analyte reaction. Bergveld et al. discussed the Donnan effect from adsorbed protein layer on the membrane, and attributed the low sensor response (order of mV) to the compensating effect from the ion sensitivity of ISFET, such as the pH-sensitive ISFET [70, 71]. With numerical simulation, Wipf demonstrated the insensitivity of surface potential to the analyte binding for a Nernstian surface. Then, by fitting the simulation model to the experimental data of protein sensing with gold surface, he showed that higher analyte sensitivity can be achieved from the reduction in the density of surface hydroxyl groups and the resulting pH sensitivity [45]. In this work, analytical studies were performed for the analyte charge sensitivity on a generic oxide surface modified with the specific probing molecule. The

analytical solutions show that the sensitivity is greatly dependent on and compensated by the proton buffering capability, which is further illustrated by numerical simulation results. In the following context, first briefly reviewed is the site-binding model for ISFET with amphoteric metal oxide, developed by Bergveld et al. [43]. Then, the model is expanded to include the probe-analyte reaction, as well as the different number of charges carried by the probe and analyte, which is an extension from the model by Wipf [45]. In addition to the numerical simulation as done by Wipf, analytical expressions are also derived to mathematically demonstrate the impact of pH sensitivity on analyte charge sensing. In reality, both the probe and the analyte biomolecules have an isoelectric point (pI), and therefore the charges they carry are pH-dependent. The model is then further modified to take into account this pH-dependency. Finally, the simulation results are analyzed and discussed in detail.

4.2   The Bare Oxide Model

When in direct contact with aqueous solutions, there are the intrinsic deprotonation and protonation reactions associated with the hydroxyl groups (A-OH) on the oxide surface:

$$A - OH \; \rightleftharpoons \; A - O^- \; + \; H_s^+, \text{and} \tag{4.1}$$

$$A - OH_2^+ \rightleftharpoons A - OH \; + \; H_s^+. \tag{4.2}$$
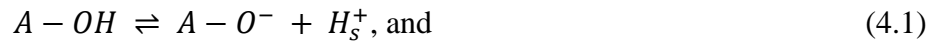
The dissociation constants for the two reactions are

$$K_a = \frac{[A-O^-][H_s^+]}{[A-OH]}, \text{and} \tag{4.3}$$

$$K_b = \frac{[A-OH][H_s^+]}{[A-OH_2^+]}, \tag{4.4}$$

in which [] denotes the areal density (#/cm^2), except for [H$_s^+$] which is the molar concentration (mol/L) of [H$_3$O$^+$] in direct proximity to the oxide surface. Notice that the definition of K_b in

(4.4) is the reciprocal of Bergveld's definition [43]. Practically it is sometimes more convenient to use the logarithmic form:

$$pK_a = -log_{10} K_a, \text{ and} \tag{4.5}$$

$$pK_b = -log_{10} K_b. \tag{4.6}$$

The total surface group density, N_s, is therefore

$$N_s = [A - O^-] + [A - OH] + [A - OH_2^+]. \tag{4.7}$$

From (4.3), (4.4) and (4.7), we can rewrite each group density as

$$[A - O^-] = N_s \frac{K_a K_b}{[H_s^+]^2 + K_b[H_s^+] + K_a K_b}, \tag{4.8}$$

$$[A - OH] = N_s \frac{K_b[H_s^+]}{[H_s^+]^2 + K_b[H_s^+] + K_a K_b}, \text{ and} \tag{4.9}$$

$$[A - OH_2^+] = N_s \frac{[H_s^+]^2}{[H_s^+]^2 + K_b[H_s^+] + K_a K_b}. \tag{4.10}$$

As two of the three surface groups carry charges, the total surface charge density σ_s can be written as:

$$\sigma_s = e\{[A - OH_2^+] - [A - O^-]\} = eN_s \frac{[H_s^+]^2 - K_a K_b}{[H_s^+]^2 + K_b[H_s^+] + K_a K_b}, \tag{4.11}$$

by plugging in (4.8) and (4.10).

Similar to the definition for buffer solution with a weak acid, Bergveld defined the intrinsic buffer capacity of the surface, β_s, as the resistance of surface pH change to strong base d[B] (or acid) [43]:

$$\beta_s = \frac{d[B]}{dpH_s}. \tag{4.12}$$

Here, [B] is actually the density of the net surface charge:

$$[B] = [A - O^-] - [A - OH_2^+] = -\frac{\sigma_s}{e}, \tag{4.13}$$

and the intrinsic buffer capacity becomes

$$\beta_s = \frac{-d\sigma_s}{e \cdot dpH_s} = 2.303 N_s [H_s^+] \frac{K_b([H_s^+]^2 + 4K_a[H_s^+] + K_a K_b)}{([H_s^+]^2 + K_b[H_s^+] + K_a K_b)^2}. \tag{4.14}$$

One thing to notice is that the intrinsic buffer capacity is defined on the pH directly adjacent to

the oxide surface (pH$_s$), which is different from and should not be confused with the pH in the

bulk solution (pH$_b$). About the negative sign in (4.14), as [H$_s^+$] increases, pH$_s$ decreases (dpH$_s$ <

0). The surface charge becomes more positive ($d\sigma_s > 0$), and this definition ensures a positive

β$_s$.
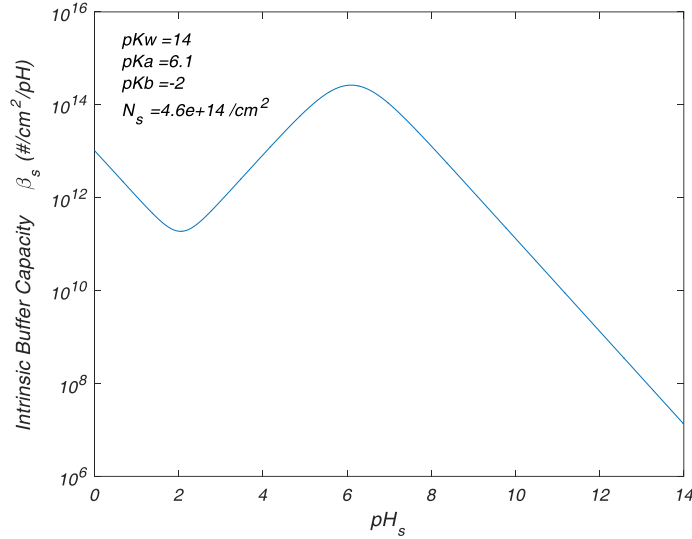
Figure 4.1. The intrinsic buffer capacity versus surface pH for SiO$_2$

Figure 4.1 shows the simulated intrinsic buffer capacity over a wide range of surface pH for

SiO$_2$. The pK_a and pK_b are assumed to be 6.8 and -2, and the total hydroxyl group density (N_s) is

assumed to be 4.6×10^{14}/cm^2 [33]. Similar to the buffer capacity of a buffer solution, the intrinsic

buffer capacity reaches the maximums near the pK_a and pK_b (out of plot range), suggesting

strong buffer effect of protons. As a result, if protons are added at these surface pH values, most

of them will be buffered by the surface hydroxyl groups via (4.1) and (4.2), making it very difficult to alter the surface pH.

After charged analytes bind to the oxide surface, the surface charge density changes, which leads to the redistribution of the ions and analytes within the electrical double layer. Consequently, this also changes the potential drop across the double layer, known as the surface potential Ψ_s. For ISFETs and Bio-FETs, the change of Ψ_s is equivalent to the shift of threshold voltage V_T, and can be measured via multiple ways. For bare oxide surface, proton is the analyte, and Ψ_s relates the surface proton concentration $[H_s^+]$ to the proton concentration in the bulk solution $[H_b^+]$, via Boltzmann distribution:

$$[H_s^+] = [H_b^+]e^{-\frac{e\Psi_s}{kT}}. \tag{4.15}$$

Taking the logarithm of both sides yields the relation between surface and bulk pH:

$$pH_s = pH_b + \frac{e\Psi_s}{2.303kT}. \tag{4.16}$$

Re-organize (4.16), we get

$$\Psi_s = 2.303\frac{kT}{e}(pH_s - pH_b). \tag{4.17}$$

By approximating the electric double layer as a capacitor, Ψ_s can also be related to the surface charge density σ_s via the double layer capacitance C_{dl}:

$$\sigma_s = \Psi_s \cdot C_{dl}. \tag{4.18}$$

Gouy-Chapman-Stern model suggests C_{dl} can be considered as two capacitor in series:

$$\frac{1}{C_{dl}} = \frac{1}{C_{st}} + \frac{1}{C_{diff}}, \tag{4.19}$$

including the Stern layer capacitance C_{st} and the diffuse layer capacitance C_{diff}. C_{diff} is highly dependent on the ionic strength of the solution, which determines the Debye screening length λ_D:

$$\lambda_D = \sqrt{\frac{\varepsilon_0 \varepsilon_r k_B T}{2 N_A e^2 I}}, \tag{4.20}$$

where ε_0 is the vacuum permittivity, k_B is the Boltzmann constant, N_A is the Avogadro number, and I is the ionic strength of the solution.

Using (4.11), (4.15) and (4.18), the one-to-one relation between $[H_b^+]$ and Ψ_s can be found:

$$[H_b^+] = e^{\frac{e\Psi_s}{kT}} \frac{K_b \frac{C_{dl}}{eN_s}\Psi_s + \sqrt{K_b^2 \left(\frac{C_{dl}}{eN_s}\Psi_s\right)^2 - 4\left(\frac{C_{dl}}{eN_s}\Psi_s\right)^2 K_a K_b + 4 K_a K_b}}{2\left(1 - \frac{C_{dl}}{eN_s}\Psi_s\right)}. \tag{4.21}$$
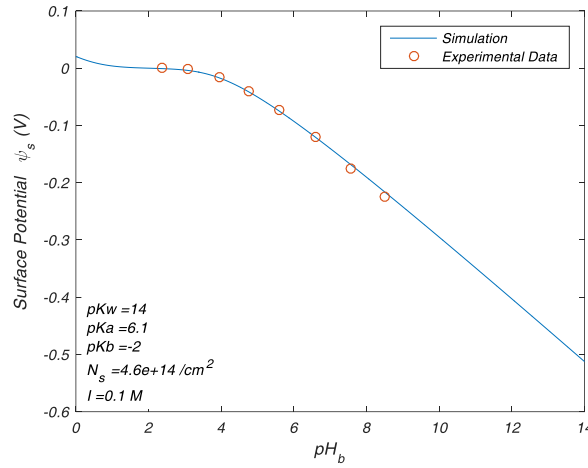
Figure 4.2. Surface potential of bare SiO_2 versus pH of bulk solution. The simulation highly agrees with the data from pH sensing experiments by Yuchen Liang, using Si nano-grating FET with 0.1M phosphate buffer solutions.

Simulation is performed to illustrate the relation between surface potential Ψ_s and bulk solution pH, and compared to the experimental data by Yuchen Liang, as shown in Figure 4.2. The pKa is adjusted to 6.1, which results in a good fit. More to our interest is the slope of the curve, $d\Psi_s$/dpH$_b$, which defines the pH sensitivity of the surface. From (4.17), the pH sensitivity can be written as

$$\frac{d\Psi_s}{dpH_b} = \frac{2.303kT}{e}\left(\frac{dpH_s}{dpH_b} - 1\right) = \frac{2.303kT}{e}\left(\frac{dpH_s}{d\Psi_s}\frac{d\Psi_s}{dpH_b} - 1\right), \tag{4.22}$$

and after re-organizing the terms, it becomes

$$\frac{d\Psi_s}{dpH_b} = \frac{2.303kT}{e}\frac{1}{\frac{2.303kTdpH_s}{e}\frac{1}{d\Psi_s}-1}.$$

(4.23)

From (4.14) and (4.18), the intrinsic buffer capacity can be written as

$$\beta_s = \frac{-d\sigma_s}{e\cdot dpH_s} = \frac{-d(\Psi_s\cdot C_{dl})}{e\cdot dpH_s} = -\frac{C_{dl}}{e}\frac{d\Psi_s}{dpH_s},$$

(4.24)

and therefore, we can find

$$\frac{dpH_s}{d\Psi_s} = -\frac{C_{dl}}{e\beta_s}.$$

(4.25)

Plug (4.25) back into (4.23), the pH sensitivity is:

$$\frac{d\Psi_s}{dpH_b} = \frac{2.303kT}{e}\frac{1}{-\frac{2.303kTC_{dl}}{e}\frac{1}{e\beta_s}-1}$$

$$= \frac{-2.303kT}{e}\frac{1}{1+\frac{2.303kTC_{dl}}{e}\frac{1}{e\beta_s}} = \frac{-2.303kT}{e}\alpha, \text{ with}$$

(4.26)

$$\alpha = \frac{1}{1+\frac{2.303kTC_{dl}}{e}\frac{1}{e\beta_s}}.$$

(4.27)

Notice that α varies between 0 and 1. For very large β_s, α approaches 1 and the maximum pH

sensitivity is 59.3 mV/pH under room temperate, known as the Nernstian limit [43].
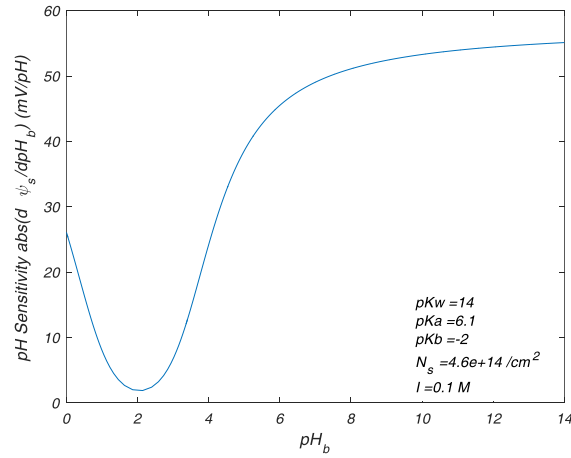
Figure 4.3. pH sensitivity versus the bulk solution pH for SiO_2

57

Figure 4.3 illustrates the pH sensitivity with respect to the bulk solution pH. From (4.27), the pH sensitivity at room temperature is determined by α, which is then mainly determined by β_s. Why does the high pH sensitivity in bulk solution span over a wide range (pH$_b$ over 6), yet β_s is large only near its pKa value of 6.1? The simple answer is that surface pH (pH$_s$, which β_s is defined on) and bulk pH (pH$_b$, which pH sensitivity is defined on) are not linearly related. (4.16) suggests that pH$_s$ and pH$_b$ are linked via the surface potential Ψ_s. Figure 4.2 shows a fast decreasing Ψ_s, as pH$_b$ increases in the basic region (pH$_b$ > 6). The decrease in Ψ_s cancels out the increase of pH$_b$ according to (4.16), which leaves pH$_s$ mostly unchanged, and equivalently expands the pH$_s$ to a wider range of pH$_b$. Hence, one must be careful when discussing any parameter defined on pH$_s$ in the scope of pH$_b$, as often the relation between the two are highly non-linear.

4.3   The Oxide Model Modified with Biological Probe

Besides protons to which the oxide surface has intrinsic sensitivity, the analytes for FET biosensors also include a large variety of other ions as well as biological molecules, such as Na^+, protein, DNA, etc. In this section, the site-binding model from section 4.2 is expanded to take into account these other types of analytes, by adding the reaction between the target analyte (T) and the immobilized linker on the oxide surface (L):

$$AL - T \; \rightleftharpoons \; AL \, + \, T. \tag{4.28}$$

As a generic model, the number of electron charges carried by the linker, the target analyte and the complex are assumed to be s, v, and t, respectively. This is an extension from Wipf's model, in which the linker is electrically neutral, and the target analyte carries one negative charge [45]. Similarly, we can define the equilibrium dissociation constant K_D:

$$k_D = \frac{[AL^s][T_s^v]}{[AL-T^t]}, \text{ and} \tag{4.29}$$

$$pk_D = -log_{10} \, k_D. \tag{4.30}$$

In (4.29), $[T_s^v]$ is the analyte concentration in close proximity to the surface, while the other

quantities are areal densities. Because the linker is usually immobilized via the reaction with

existing hydroxyl groups on the surface, the total surface group density N_s becomes:

$$N_s = [A-O^-] + [A-OH] + [A-OH_2^+] + [AL-T^t] + [AL^s]. \tag{4.31}$$

We can define the total linker group density N_l as:

$$N_l = [AL-T^t] + [AL^s]. \tag{4.32}$$

By using (4.3), (4.4), (4.7), (4.29), (4.31) and (4.32), we can find the surface density for each

group:

$$[A-O^-] = (N_s - N_l)\frac{K_a K_b}{[H_s^+]^2 + K_b[H_s^+] + K_a K_b}, \tag{4.33}$$

$$[A-OH] = (N_s - N_l)\frac{K_b[H_s^+]}{[H_s^+]^2 + K_b[H_s^+] + K_a K_b}, \tag{4.34}$$

$$[A-OH_2^+] = (N_s - N_l)\frac{[H_s^+]^2}{[H_s^+]^2 + K_b[H_s^+] + K_a K_b}, \tag{4.35}$$

$$[AL^s] = N_l \frac{K_D}{K_D + [T_s^v]}, \text{ and} \tag{4.36}$$

$$[AL-T^t] = N_l \frac{[T_s^v]}{K_D + [T_s^v]}. \tag{4.37}$$

The total surface charge density σ_s becomes:

$$\sigma_s = e\{[A-OH_2^+] - [A-O^-] + t \cdot [AL-T^t] + s \cdot [AL^s]\} =$$

$$e(N_s - N_l)\frac{[H_s^+]^2 - K_a K_b}{[H_s^+]^2 + K_b[H_s^+] + K_a K_b} + eN_l\frac{s \cdot K_D + t \cdot [T_s^v]}{K_D + [T_s^v]} = \sigma_H + \sigma_T, \text{ with} \tag{4.38}$$

$$\sigma_H = e(N_s - N_l)\frac{[H_s^+]^2 - K_a K_b}{[H_s^+]^2 + K_b[H_s^+] + K_a K_b}, \text{ and} \tag{4.39}$$

$$\sigma_T = eN_l \frac{s \cdot K_D + t \cdot [T_s^v]}{K_D + [T_s^v]}. \tag{4.40}$$

The surface and bulk analyte concentrations also obey Boltzmann distribution:

$$[T_s^v] = [T_b^v] e^{-\frac{ev\Psi_s}{kT}}. \tag{4.41}$$

Note that the electric potential energy in the exponential term includes v, and therefore if the analyte carries more charges the surface concentration will be lower. Similarly, we can find

$$pT_s = pT_b + \frac{ev\Psi_s}{2.303kT}, \text{ and} \tag{4.42}$$

$$\Psi_s = 2.303 \frac{kT}{ev} (pT_s - pT_b). \tag{4.43}$$

From (4.15) and (4.41), it becomes obvious that the hydroxyl group – proton reaction and the probe – analyte reaction are coupled, via the surface potential Ψ_s. This is how the pH sensitivity can compensate and buffer the analyte charge sensing.

From (4.15), (4.18), (4.38), and (4.41), the relation between $[H_b^+]$, $[T_b^v]$, and Ψ_s can be found. The surface potential can be solved for given pH and analyte concentrations in the bulk solution. In the analysis of bare oxide model, the intrinsic buffer capacity β_s is critical in the derivation of pH sensitivity, as it directly indicates the buffering capability of proton by the surface hydroxyl groups. Here we can develop similar concepts for both proton and analyte, using (4.39) and (4.40):

$$\beta_H = \frac{-d\sigma_H}{e \cdot dpH_s} = \frac{-d\sigma_H}{e \cdot d[H_s^+]} \frac{d[H_s^+]}{dpH_s}$$

$$= 2.303(N_s - N_l)[H_s^+] \frac{K_b([H_s^+]^2 + 4K_a[H_s^+] + K_aK_b)}{([H_s^+]^2 + K_b[H_s^+] + K_aK_b)^2}, \text{ and} \tag{4.44}$$

$$\beta_T = \frac{-d\sigma_T}{e \cdot dpT_s} = \frac{-d\sigma_T}{e \cdot d[T_s^v]} \frac{d[T_s^v]}{dpT_s} = 2.303N_l[T_s^v] \frac{(t-s)K_D}{(K_D + [T_s^v])^2}. \tag{4.45}$$

60

β_H is the buffer capacity of proton from the surface hydroxyl groups and β_T is the buffer

capacity of analyte from the surface probes. Because both reactions are coupled and the surface

charges respond to the analyte binding as a whole, we are more interested in the analyte buffer

capacity β_s from all surface species, including both the hydroxyl groups and the probes:

$$\beta_s = \frac{-d\sigma_s}{e \cdot dpT_s} = \frac{-d(\sigma_H + \sigma_T)}{e \cdot dpT_s} = \beta_T - \frac{d(\sigma_H)}{e \cdot dpT_s}$$

$$= \beta_T + \frac{-d(\sigma_H)}{e \cdot dpH_s} \frac{dpH_s}{dpT_s} = \beta_T + \beta_H \frac{dpH_s}{dpT_s}. \tag{4.46}$$

By taking the derivative on (4.16), assuming the bulk pH is controlled and constant, and by

applying (4.18), we can rewrite (4.46) as:

$$\beta_s = \beta_T + \beta_H \frac{dpH_s}{dpT_s} = \beta_T + \frac{e}{2.303kTC_{dl}} \frac{d\sigma_s}{dpT_s} \beta_H$$

$$= \beta_T + \frac{-e^2}{2.303kTC_{dl}} \beta_s \beta_H. \tag{4.47}$$

Re-organizing the terms, we get

$$\beta_s = \frac{\beta_T}{1 + \frac{e^2}{2.303kTC_{dl}} \beta_H} = \beta_T \cdot \alpha_H, \text{ with} \tag{4.48}$$

$$\alpha_H = \frac{1}{1 + \frac{e^2}{2.303kTC_{dl}} \beta_H}. \tag{4.49}$$

From (4.48) and (4.49), we can clearly see that β_s is directly determined by β_T, the buffer

capacity of analyte from only the surface probes. To achieve a high β_T, either the surface has

high surface probe density N_l, or the surface analyte concentration $[T_s^v]$ is close to K_D.

Besides β_T, (4.48) suggests that β_s is also determined by a factor α_H which varies between 0 and

1. Interestingly, α_H is controlled by β_H, the proton buffer capacity from the hydroxyl groups.

With large β_H, α_H approaches 0 and β_s is greatly attenuated from β_T. To achieve overall high

buffer capacity of analyte, β_H must be well controlled to eliminate the effect of proton buffering. This analysis is critical as it relates to the discussion of pH sensitivity in the later context.

β_S is a significant property of the oxide surface for FET-based biosensors, as it indicates the change of total surface net charge due to the change of surface analyte concentration. However, it is defined on the surface concentration and surface charge, and inconvenient for the study of practical problems. In the sensing experiments, the bulk analyte concentration is controlled and the change of surface potential is measured. Similar to pH sensing, we can also define a practical sensitivity for analytes: $-d\Psi_s/dpT_b$. From (4.18) and (4.46), we can write

$$\frac{-d\Psi_s}{dpT_b} = \frac{-1}{C_{dl}}\frac{d\sigma_s}{dpT_s}\frac{dpT_s}{dpT_b} = \frac{e}{C_{dl}}\beta_s\frac{dpT_s}{dpT_b}. \tag{4.50}$$

Take the derivative on (4.42), and we can find

$$\frac{dpT_s}{dpT_b} = 1 + \frac{ev}{2.303kT}\frac{d\Psi_s}{dpT_b}. \tag{4.51}$$

Plug (4.51) back to (4.50), and we can solve for the analyte sensitivity:

$$\frac{-d\Psi_s}{dpT_b} = \frac{2.303kT}{ev}\frac{1}{1+\frac{2.303kTC_{dl}}{ev}\frac{1}{e\beta_S}} = \frac{2.303kT}{ev}\alpha_T, \text{ with} \tag{4.52}$$

$$\alpha_T = \frac{1}{1+\frac{2.303kTC_{dl}}{ev}\frac{1}{e\beta_S}}. \tag{4.53}$$

From (4.52) and (4.53), the analyte sensitivity has a Nernstian limit of 59.3/v mV per order change of bulk analyte concentration, which agrees with the Nernstian equation. There is also a factor α_T between 0 and 1, which highly depends on β_S, the analyte buffer capacity from all surface groups. The analyte sensitivity approaches the Nernstian limit when a high β_S is achieved. From previous discussions, this requires a large β_T and a small β_H. The large β_T may come from high probe density N_l and/or surface analyte concentration [T_s^v] close to K_D, and the

small β_H implies suppressed pH sensitivity. A surface highly sensitive to proton, though

beneficial in pH sensing, will greatly compensate and buffer the change of surface charge due to

the analyte binding. For example, as analytes carrying positive charges bind to the surface and

make the surface charge density σ_s more positive, the surface potential Ψ_s will also be more

positive according to (4.18). In a sensing solution with controlled bulk pH, (4.16) suggests the

surface pH will increase. In other words, the surface proton concentration $[H_s^+]$ will decrease.

According to Le Chatelier's principle, the equilibrium established in (4.1) and (4.2) will shift to

the right to compensate for the loss of $[H_s^+]$. For both of these reactions, this equilibrium shift

will cause the surface hydroxyl groups to be more negative charged, which effectively

compensate the effect from the binding of the positively-charged analytes.

Simulation for sensing of non-proton analyte is carried out based on the analysis in this section,

and the results are shown in Figure 4.4 and Figure 4.5. The same SiO_2 surface in Figure 4.2 is

used, with the same pK_a, pK_b and N_s. Some of the surface hydroxyl groups are occupied by

probes, with density N_l assumed to be $1 \times 10^{12}/cm^2$, which is practically near the highest probe

density achievable and reported in experiments [7]. The ionic strength is set to be 10 mM which

is reasonable for sensing small (nm-size) biomolecules. K_D is 100 pM which is within the

reasonable range for antibody – protein reactions. Here the probe is assumed to carry one

positive elementary charge, while the analyte carries 20. Figure 4.4a shows the surface potential

Ψ_s versus the pH of the bulk solution, which resembles Figure 4.2. The curves slightly split in

the acidic region where the buffer capacity of proton is relatively lower. The relation between

surface and bulk pH is shown in Figure 4.4b. As discussed previously, the fast changing of Ψ_s in

the base region cancels out the increase of pH_b, which expands the surface pH (4.8 – 5.2) to a
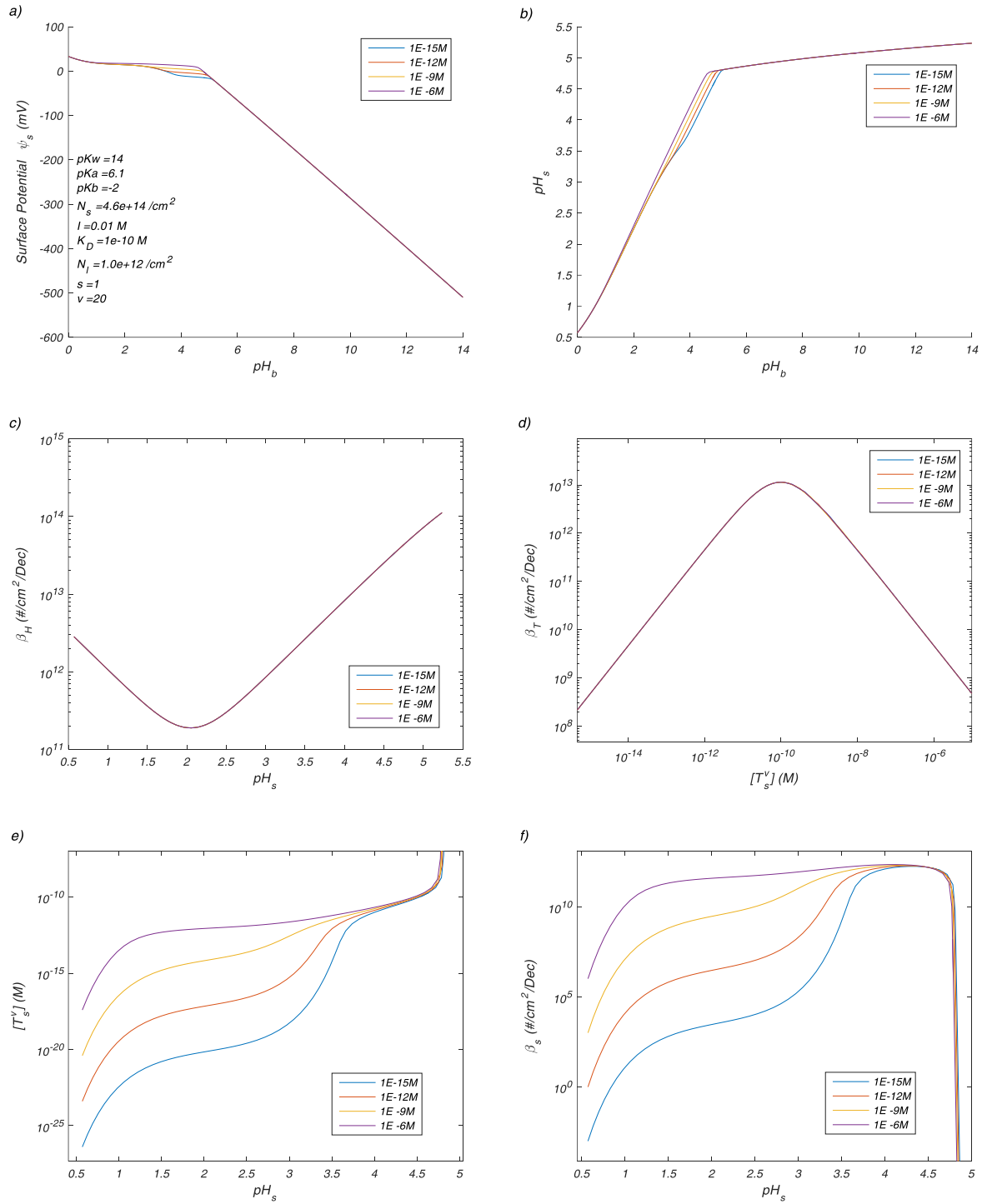
Figure 4.4. Simulation of non-proton analyte sensing using FET biosensor with SiO$_2$ surface. The simulated analyte concentrations are 1 μM, 1 nM, 1 pM and 1 fM.
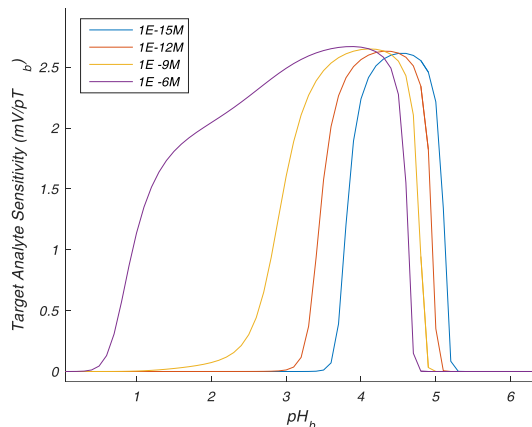
Figure 4.5. Simulation of analyte sensitivity for FET biosensor. The conditions are the same as Figure 4.4.

wide range of bulk pH (5.1 – 14). Figure 4.4c and d shows β_H and β_T respectively. Both

approach the maximum at the corresponding dissociation constants (pK_a, pK_b and K_D), and

greatly reduce near the midpoint between them. The surface analyte concentration [T_s^v] is shown

in Figure 4.4e with varying surface pH. From previous discussions this is one of the factors that

may greatly impact β_s, which is plotted in Figure 4.4f. It is noticeable that at different bulk

analyte concentrations, large β_s spans over different surface pH regions. This is further

translated to the analyte sensitivity in Figure 4.5, which shows wider sensitive regions shifting in

the more acidic direction as the bulk analyte concentration increases. These results will be

discussed in detail in section 4.5.

4.4   pH-dependent Charge Carried by Analyte and Probe

Unlike certain ions (*e.g.,* Na⁺) which always carry the same charge regardless of pH, in

biomolecules some functional groups (*e.g.,* amine) may react with proton and change their

charge state. The final pH dependence of the net charge carried by the molecule is then

65

determined by the different dissociation constants, numbers and types of these groups. At a particular pH named isoelectric point (pI), the molecule is electrically neutral. As the pH of the surrounding solution deviates from pI, the net charge can become positive or negative, depending on the gain or loss of the protons. In the modified oxide model discussed previously, the charges carried by probe and analyte are fixed for simplicity. Here, the more generic case is considered where these charges are dependent on the pH close to the oxide surface. To be more specific, the charges carried by probe (s), analyte (v) and complex (t) are all functions of pH_s. With this change in mind, the net surface charge density σ_s is the same as (4.38), although s and t now vary with $[H_s^+]$. β_H still has the same expression as (4.44), but due to the pH_s dependence, β_T changes dramatically:

$$\beta_T = \frac{-d\sigma_T}{e \cdot dpT_s} = \frac{-d\sigma_T}{e \cdot d[T_s^v]} \frac{d[T_s^v]}{dpT_s}$$

$$= 2.303 N_l [T_s^v] \frac{(t-s)K_D}{(K_D+[T_s^v])^2} - N_l \frac{dpH_s}{dpT_s} \frac{ds}{dpH_s} - \frac{N_l[T_s^v]}{K_D+[T_s^v]} \frac{dpH_s}{dpT_s} \frac{dv}{dpH_s}$$

$$= \beta_{T0} - N_l \frac{dpH_s}{dpT_s} \frac{ds}{dpH_s} - \frac{N_l[T_s^v]}{K_D+[T_s^v]} \frac{dpH_s}{dpT_s} \frac{dv}{dpH_s}. \tag{4.54}$$

Here β_{T0} is the renamed β_T from (4.45) in the previous section. As one would expect, β_s also changes:

$$\beta_s = \frac{-d\sigma_s}{e \cdot dpT_s} = \beta_T + \beta_H \frac{dpH_s}{dpT_s}$$

$$= \beta_{T0} + \beta_H \frac{dpH_s}{dpT_s} - N_l \frac{dpH_s}{dpT_s} \frac{ds}{dpH_s} - \frac{N_l[T_s^v]}{K_D+[T_s^v]} \frac{dpH_s}{dpT_s} \frac{dv}{dpH_s}. \tag{4.55}$$

Using the same trick we did for (4.46), the expression of β_s can be found:

$$\beta_s = \beta_{T0} \cdot \alpha_H, \text{ with} \tag{4.56}$$

$$\alpha_H = \frac{1}{1+\frac{e^2}{2.303kTC_{dl}}\beta_H - N_l\frac{e^2}{2.303kTC_{dl}}\frac{ds}{dpH_s} - N_l\frac{[T_s^v]}{K_D+[T_s^v]}\frac{e^2}{2.303kTC_{dl}}\frac{dv}{dpH_s}}. \tag{4.57}$$

One would notice that if there is no pH_s dependency of s and v, the last two terms in the

denominator will go away, and (4.57) falls back to (4.49). As pH_s increases, s and v will likely

decrease, make these two terms positive. Therefore, the pH sensitivity of analyte and probe will

have similar effect as the proton buffer capacity, reducing α_H and therefore the analyte buffer

capacity from all surface groups.

The expression of analyte sensitivity stays the same as in (4.52) and (4.53), if we assume that v is

solely a function of pH_s and doesn't change across the double layer. This is a reasonable

assumption for the purpose of this study, because otherwise (4.41) will not hold and the

distribution will be too complicated for analytical solutions.

For both probe and analyte, the pH dependence of net charge varies by molecule type. For

simplicity in simulation, protonation and deprotonation of one surface group are assumed,

similar to our previous analysis on bare oxide. For example, the following proton reactions for

analyte molecules are assumed:

$$A - H_2^+ \rightleftharpoons A - H + H_s^+, \text{ and} \tag{4.58}$$

$$A - H \rightleftharpoons A^- + H_s^+. \tag{4.59}$$

The dissociation constants of the two reactions are:

$$K_{a1} = \frac{[A-H][H_s^+]}{[A-H_2^+]}, pK_{a1} = -log_{10} K_{a1}, \text{ and} \tag{4.60}$$

$$K_{a2} = \frac{[A^-][H_s^+]}{[A-H]}, pK_{a2} = -log_{10} K_{a2}. \tag{4.61}$$

A single analyte molecule has totally v of these functional groups:

$$v = [A^-] + [A - H] + [A - H_2^+]. \tag{4.62}$$

The same assumptions are made for probe as well, with s functional groups that react with

67

proton. To be consistent with our previous simulation, s is set to 1 and v is set to 20. For simplicity, pK_{a1} and pK_{a2} are set to 7 for both analyte and probe, and the resulting pI of 7 falls within the range reported for antibody (IgG) [72].
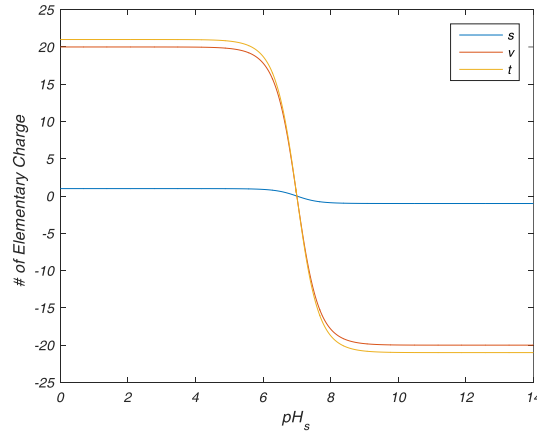
Figure 4.6. Charge carried by probe (s), analyte (v) and complex (t) over the full pH range

Figure 4.6 shows the charge carried by probe (s), analyte (v) and complex (v) over the full range of surface pH. Here v is assumed to be the sum of s and v. Based on these pH dependencies, the simulation is carried out and the results are shown in Figure 4.7.
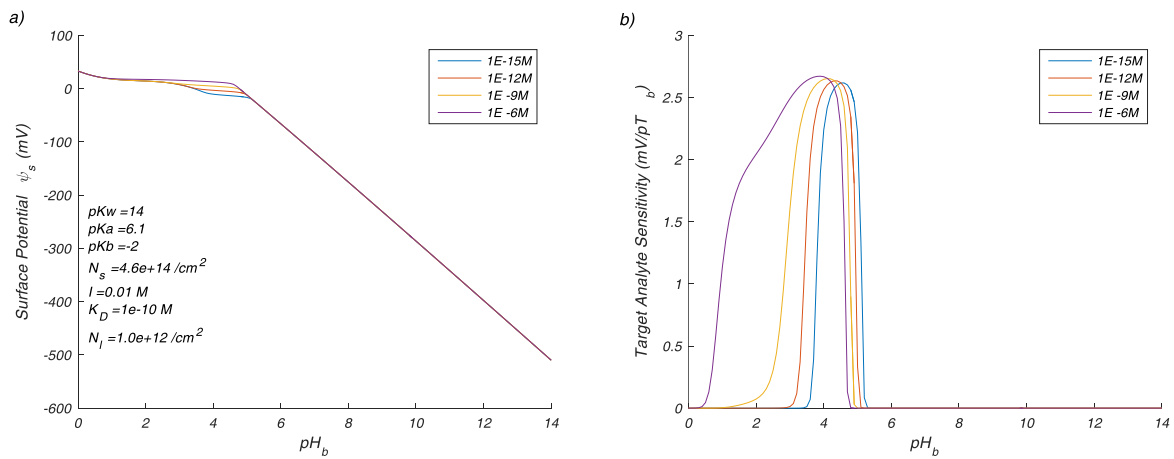
Figure 4.7 Simulation of surface potential and charge sensitivity with pH-dependent charges carried by probe and anlyte

In comparison to Figure 4.4 and Figure 4.5, results in Figure 4.7 are almost identical. This is reasonable, as Figure 4.6 suggests the charges carried by both probe and analyte saturate for pH below 6. According to Figure 4.4b, the surface pH never increases beyond 5.5. Therefore, in the actual pH_s range the analyte and probe charges can be considered fixed, which results in the similar simulation results. Due to this similarity, Figure 4.4 and Figure 4.5 of the fixed-charge model will be discussed in the next section.

On the other hand, the analytical model in this section is still a useful tool to study the sensing capability of generic analytes, which may have more complicated charge states beyond the scope of this discussion.

4.5 Discussion

From Figure 4.5, the optimal pH range for analyte detection of all simulated concentrations lies in the acidic region. At first glance, this is no surprise because of the high proton buffer capacity in the basic region. Figure 4.3 shows that the pH sensitivity exceeds 40 mV/pH and approaches Nernstian limit for bare SiO_2 as pH goes above 5, suggesting high proton buffer capacity. The peak analyte sensitivity measures about 2.5 mV/pT, which is lower but at the order of Nernstian limit (59.3/20=3.0 mV/pT). However, if we look closely, we can see that the peak analyte sensitivity does not align with the minimum of β_H at pH_s of 2, which converts approximately to pH_b of 2 as shown in Figure 4.4c and b. In addition, as the analyte concentration increases, the sensitive region shifts to the lower pH, and the range of this region expands.

From Figure 4.4b, the relation between surface and bulk pH can be roughly divided into two regions. For pH_b less than 4.8, the pH_s changes almost linearly with pH_b, due to the low proton buffer capacity. As pH_b increases over 4.8, any changes of proton concentration at the oxide

surface are buffered by the high buffer capacity of the surface hydroxyl groups, resulting in a relatively stable pH_s over a large range of pH_b. This can be backed-up by Figure 4.4c. Plotted in logarithmic scale, β_H quickly increases towards maximum as pH_s moves in the basic direction. This exponential increase of β_H directly affects α_H, leading to the fast decay of β_s at pH_s of 4.8, as shown in Figure 4.4f. However, in the analyte-sensitive region where β_H is small and α_H approaches one, β_T also demonstrates significant effect on β_s. From our previous discussions, a large probe density N_l will improve β_T, but in a real sensing experiment N_l is constant which we assume for our simulation. Another factor that may affect β_T is the surface analyte concentration $[T_s^v]$. Figure 4.4d shows that β_T reaches its maximum at K_D (1×10^{-10}M). Similar to our previous analysis for proton, this suggests that when the surface analyte concentration $[T_s^v]$ is close to K_D, it is less affected by the change of bulk analyte concentration $[T_b^v]$ due to the strong analyte buffering effect. As an illustration, the curves in Figure 4.4e for different bulk analyte concentrations overlap when $[T_s^v]$ is close to K_D of 1×10^{-10}M. On the other hand, in the corresponding pH_s range around $4 - 4.5$, β_T reaches its maximum, leading to a high β_s as well as high analyte sensitivity in the pH_b range of $3.8 - 4.3$. This is the why the maximum analyte sensitivity doesn't align with the minimum of β_H around pH_s of 2. Indeed, the low proton buffer capacity of surface is a prerequisite for analyte sensing. However, even when this requirement is fulfilled, the analyte sensitivity is also largely affected by β_T. In Figure 4.4e, there is a relatively "flat" region around pH_s of 2 for all analyte concentrations, where β_H reaches its minimum and changes slowly. However, since $[T_s^v]$ is off by a lot from K_D, we don't see a very high β_s or analyte sensitivity in this region for all analyte concentrations.

As the analyte concentration increases, the analyte sensitive regions shifts to the acidic direction, and the ranges expand, as shown in Figure 4.5. The latter can be traced back to the buffer effect of the surface hydroxyl groups. Since the pK_a for deprotonation (4.1) is 6.1 and pK_b for protonation (4.2) is -2, in the analyte sensitive regions (roughly pH_b 2 – 5, pH_s 2.3 – 4.8) the deprotonation reaction (4.1) dominates. The analytes are positively charged in these regions. If the bulk analyte concentration $[T_b^v]$ increases by one order, instead of following the one-order increase, the surface analyte concentration $[T_s^v]$ will stay mostly constant when it's close to K_D, as discussed previously. As a result, (4.42) predicts that Ψ_s will shift positively, resulting in a lower $[H_s^+]$ if bulk pH is controlled. To compensate for the loss of protons near the surface, reaction (4.10) will shift to the right, resulting in more negative surface charges buffering the positive analytes. If the starting concentration of analyte in the bulk solution is high, a larger portion of the neutrally-charged hydroxyl groups (-OH) have already been consumed to buffer the surface analytes, with less available to further buffer even the higher change of analyte concentration. The effectively-reduced buffer capacity of the hydroxyl groups leads to a wider range of the analyte sensitive regions, as well as slightly higher peak sensitivity. The acidic shift of the sensitive regions in Figure 4.5 comes from the slower decay of $[T_s^v]$ from K_D towards the acidic direction with the increase of bulk analyte concentration, as shown in Figure 4.4e. This effectively broadens the range of β_T close to K_D, resulting in wider and more acidic regions with analyte sensitivity.

4.6   Conclusion

The high density of intrinsic hydroxyl groups on oxide surfaces, as well as their protonation and deprotonation reactions, are beneficial for ISFET biosensors in pH sensing. Depending on the

dissociation constants for the two reactions, a high surface buffer capacity can be achieved in certain pH regions resulting in near-Nernstian pH sensitivity. However, this high buffer capacity for proton is undesirable for the detection of non-proton analytes. Coupled by the surface potential, the immobilization of charged analytes on the oxide surface will induce the readjustment of the opposing protonation and/or deprotonation reactions, effectively buffering and compensating the added analyte charges. Though the detection of analytes is possible only with a low proton buffer capacity, the analyte sensitivity is also dependent on the buffer capacity of analytes from the surface probes. The analytical study in this work, as well as the numerical simulation for a sample SiO_2 surface, are useful tools to evaluate the feasibility of analyte detection with existing surface setup, and may guide the design of future FET-based biosensors.

CHAPTER 5

DIGITAL BIOSENSING OF INFLUENZA VIRUS WITH SINGLE SERPENTINE SILICON NANOWIRE FIELD EFFECT TRANSISTOR

We propose the digital biosensing concept with the biological field effect transistor (BioFET), by counting the individual binding events of single analyte. Because the detection is no longer based on the amplitude of the sensor output, the system is better immune to several noises, especially the non-specific shift in the output that cannot be reduced by averaging. We also demonstrate the single serpentine nanowire (NW) FET as an ideal BioFET design to achieve digital biosensing. The device was fabricated by top-down lithography, which is compatible with the CMOS processing technologies. By "folding" a long straight NW into a serpentine form, the low device noise is maintained, while the small footprint not only increases the integration density, but also allows the binding of a single analyte, which is required by the digital detection. The binding of an analyte to several segments of the NW improves both the sensitivity and the binding avidity of the biosensor. By integrating individual serpentine NW FETs into an array format, the high throughput system has a great potential to become a real-time, highly sensitive and cost-effect future biosensing platform.

Keyword: digital biosensor; serpentine; nanowire; field effect transistor; virus sensing;

5.1 Introduction

Nanowire field effect transistor (NW FET) biosensor has been widely considered as a promising candidate to replace the planar FET biosensor in the future. Besides the direct, real-time and label-free detection, the full-electrical interface, the low cost of mass production, and

considerable miniaturization of sensor devices, the NW biological FETs (BioFETs) further boost the analyte sensitivity, and enable on-chip integration at an even higher density [1-4, 6]. Despite the great potential of NW FET biosensors, however, several limitations have come to our attention in the development of practical NW BioFETs, which may hinder the advancement and commercialization of this technology.

The first limitation is related to the device scaling. Over the past 50 years, the advancement of semiconductor industry has kept pace with the downscaling of transistors, as predicted by the widely-accepted Moore's Law. Reducing manufacturing cost has been one of the driving force behind the scaling, as more transistors can be fabricated on the wafer of the same size. In 2015, the leading foundries already started shipping chips utilizing the 16/14 nm FinFET technology nodes for logic device, and 11/10 nm node has been predicted in 2017 by the International Technology Roadmap for Semiconductors (ITRS) [73]. In the field of BioFETs, the scaling and miniaturization of the sensory device have led to the NW BioFET [30], the variant of FinFET with tri-gating effect from the analytes. The most significant benefit comes from the increased surface-to-volume ratio, which enhances the device sensitivity to the surface charges [33, 34]. The BioFET industry, however, has significantly lagged behind in the implementation of the advanced technology nodes. For example, Ion Torrent, now part of Thermo Fisher Scientific, has successfully developed and commercialized pH-sensitive FETs for genome sequencing [74]. The 3 series chips (314, 316 and 318) available in 2011 – 2012, were fabricated with the 350 nm CMOS technology node. The newer Proton I and II chips, which came out around 2013, jumped to the 110 nm node that can be dated back to 2001 [75]. Downscaling of the sensory transistors

in BioFETs has been proven challenging, and one of the challenges actually comes from the increasing noise level with the device scaling.

The Schönenberger group conducted comprehensive studies on the dominating 1/f noise in the Si nanowire sensors [76]. They revealed that the observed 1/f noise was primarily due to the trapping and release of charge carriers by the trap states at the Si-oxide interface, and therefore was in accordance with the trap state noise model. The gate-referred voltage noise S_{VG}, converted from the source-drain current noise, is related to the channel size by

$$S_{VG} = \frac{e^2 N_{ot}}{W_{eff} L C_{OX}^2} \frac{1}{f}. \tag{5.1}$$

The equation includes the elementary charge e, the trap state density per area N_{ot}, the gate oxide capacitance per area C_{OX}, the channel length L, and the effective gated width $W_{eff} = W_{top} + 2W_{side}$ for a tri-gating nanowire FET. As the channel area scales down, $S_{VG} \propto 1/(W_{eff} \cdot L)$ scales up. On the other hand, for the majority of existing BioFETs, the sensor response to analyte is generally dependent on the analyte density at the gated surface, and independent of the sensor size for the same device structure. Therefore, the signal-to-noise ratio (SNR) deteriorates with the miniaturization of device. The root cause of this problem is that these BioFETs are used as analog transducers, which generally have less tolerance margin for noise than logic devices, and therefore must overcome more challenges to keep up with the scaling pace.

The lack of specificity is another limitation for not only NW, but planar BioFETs as well. BioFETs quantify the analytes by measuring the change of surface potential, ideally due to the analyte binding only. There are multiple ways to achieve this. Most commonly, one may analyze the change of device channel conductance at different analyte concentrations under a constant gate bias, or the shift of device threshold voltage from the transfer characteristics after

analytes are introduced to the biosensor. The characterization can be performed in a steady state after the association and dissociation of analytes reach an equilibrium [5, 30], or in a transient state controlled by the reaction kinetics [45]. Both approaches require a baseline to be established prior to the binding reaction, typically in a buffer solution with identical pH and ionic strength as the solution with the analytes. One exception is the differential detection with an addition reference FET (REFET) alongside the BioFET, which eliminates the noise and other non-analyte sensor responses appearing as a common signal in the output of both FETs. To achieve this, the REFET must have identical electrical characteristics as the BioFET [11], and the active surface of the REFET must be inert to the target analyte, while equally sensitive to other properties of the sensing solution (pH, ionic strength, etc.) [66]. Otherwise, the differential mechanism cannot fully eliminate the sensor response non-specific to the target analyte, which appears as an offset in the output. In practice, modifying two closely-located BioFETs with different surface chemistries alone is challenging, not to mention the harsh requirements on the surface of REFET.

For the majority of other biosensors, the baseline establishment process is mandatory, but similar problems still exist. Ideally, the BioFET is sensitive only to the target analyte. In reality, however, other differences between the baseline and analyte solutions can also introduce sensor response. The high density of hydroxyl groups at the gate oxide – solution interface, at the order of $10^{14}/cm^2$ for SiO_2 and some metal oxides, render the surface highly sensitive to pH. In Figure 5.1, both SiO_2 surfaces modified with IgG and passivated with either bovine serum albumin (BSA) (a) or $NaBH_4$ (b) demonstrated pH sensitivity of 30 mV/pH or higher. Tarasov et al. observed over 20 mV/Dec of threshold voltage shift when KCl concentration in the solution

increased from 10 mM, and attributed this ion sensitivity to the adsorption of Cl⁻ [54].

Furthermore, the ionic strength of the solution determines the Debye screening length, which has

a strong influence on the double layer capacitance C_{DL}. The sensor output can be greatly

affected by C_{DL}, because it directly relates the surface potential to the surface charge density,

which is the result from several competing and coupling reactions of the surface species.
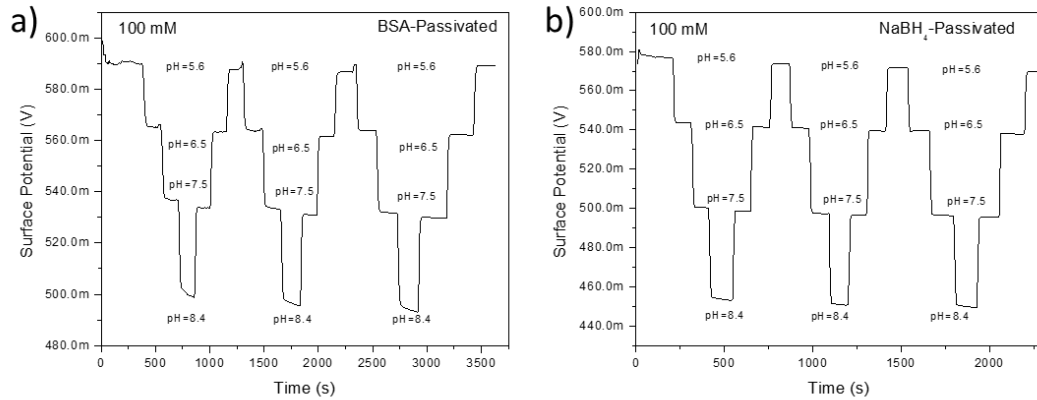
Figure 5.1. pH dependence of protein biosensor surfaces with different passivation agents. The SiO2 surface of the Si NGFETs was modified with mouse IgG, and passivated with a) BSA (~ 90 mV/3 pH) or b) NaBH4 (~ 130 mV/3 pH). Courtesy of Silu Zhang.

To minimize these differences across baseline and analyte solutions, buffer solutions are widely

used in biosensing experiments with BioFETs, as they pose strong resistance to the change of

solution pH. The buffer capacity, which quantifies this resistance, is proportional to the

concentration of the buffering weak acid (ignoring the buffer effect of water at the extreme pHs)

[77]. For higher buffer capacity and better pH stability, a higher concentration of the weak acid

is preferred. However, this high concentration also contributes to the total ionic strength of the

solution, which is another factor to consider in the preparation of the sensing solutions. The

Debye screening length, λ_D, determined by the ionic strength of the solution, must be carefully

selected to make sure the majority of the charge from the target analyte is unscreened [78]. For the detection of ions that are typically small, solutions with high buffer capacity and small Debye screening length can be used. However, to detect bigger analytes such as protein, a large Debye length limits the solution ionic strength and therefore the buffer capacity. For example, 10 nm Debye length requires ionic strength to be lower than 1 mM [45], at which the pH will be difficult to control and adjust due to the dissolution of CO_2 from air. With an uncontrollable pH difference between baseline and analyte solutions, the observed sensor response can no longer be attributed only to the binding analytes.

In this work, we propose and demonstrate the idea of digital biosensing with BioFETs to address these limitations. For the optical transducers, the digital biosensing idea has been demonstrated with the digital enzyme-linked immunosorbent assay (digital ELISA) [79]. Protein-modified beads were isolated in an array of micro wells, with each well holding a single bead. Each bead captures one protein molecule at most, and fluorescence imaging was performed on the array to label those beads with a single protein. This sensing approach is digital because the individual protein molecules are counted to determine the concentration, while an analog approach would depend on the light density determined by the captured protein density. With the electrical FET transducer, the digital biosensing can be achieved by counting the individual analyte, or the individual binding event of analyte as well. This approach eliminates the nonspecific offset that appears as part of the sensor output, as the analyte concentration is determined by the count of the sensor output, instead of the amplitude.

To be able to differentiate individual analyte or binding event required by the digital biosensing, the transducer must be sensitive enough to detect the binding of a single analyte, or quantize the

binding of a few. With electrical transducers, the detection of a single DNA molecule has been achieved and demonstrated for the carbon nanotube FET [80]. The sensor conductance clearly shows dual-level fluctuations that correspond to the binding and nonbinding state. Single-molecule detection has been extremely challenging for NW BioFETs, which requires the downscaling of nanowire diameter to achieve the ultra-high sensitivity. The detection of single influenza virus has been demonstrated with single NW BioFET, which was synthesized by chemical vapor deposition (CVD) [7]. The CVD NW BioFET was functionalized with anti-hemagglutinin antibody, and multi-level switching of conductance was observed after the introduction of the influenza virus solution. The optical imaging of the nanowire area further confirmed that the NW FET was capable of differentiating up to two viruses, a step beyond single analyte detection. However, this NW FET design may not be the optimal candidate to implement the digital biosensing idea. First, the straight single NW has a length of 2 µm, which is much greater than the analyte size (80 – 120 nm for influenza A virus). Although this may help with the device noise, the long NW may bind many analytes at the same time and lose the digital counting capability. In addition, the large footprint resulting from the straight NW design limits the integration density of the sensors in an array. Second, the downscaling of nanowire diameter (no greater than 20 nm) for the high sensitivity leads to a very small binding area, and therefore requires a high probe density at the order of 1×10^{12}/cm^2 for reasonable binding avidity. Third, the CVD process to grow the NWs is incompatible with the CMOS process for system integration. In this work, we designed and fabricated the single serpentine Si NW FET, a new design that addressed all these issues. The serpentine design allows a long NW for small device noise, further compensated by the large noise margin of the digital transducer, a small footprint

that can bind only one analyte and enables high integration density, as well as increased

sensitivity and binding avidity from the multiple NW segments to bind the analyte. We

demonstrated the digital biosensing concept with single serpentine NW BioFET, which can be

further integrated into an array using standard semiconductor processes for high throughput

digital sensing.

In the following contexts, the theory of digital biosensing with BioFETs is explained, followed

by the fabrication and experimental results of the single serpentine Si NW FET biosensor. These

results are discussed to demonstrate the digital biosensing concept.

5.2 Theory

5.2.1 Noise Sources in BioFET

As discussed previously, the most significant advancement of NW BioFETs comes from the

improved analyte sensitivity. The limit of detection (LOD), for example, is a critical parameter

to evaluate the sensitivity of a BioFET, as it defines the smallest analyte concentration a

biosensor can reliably detect [4, 36]. What ultimately limits the LOD is the largest of the noise

sources in the biosensing system. For BioFET, the major noise sources usually include the

transducer noise, the biological noise, and the nonspecific noise. The transducer noise is the

electrical device noise of the BioFET. From previous discussion, the transducer noise increases

with the downscaling of the NW channel dimensions. The nonspecific noise refers to the sensor

response from any difference between the baseline and analyte solutions, excluding the presence

of the target analytes. This may include pH, ionic strength, temperature, or other charged solutes

in the analyte solution that may be adsorbed on the active surface.

The biological noise originates from the probabilistic bindings of the analytes to the active surface of the BioFETs, which causes the mesoscopic signal fluctuation in the sensor output. Hassibi et al. conducted a comprehensive study on the statistical behavior of the biological shot-noise, and derived the quantum-limited signal-to-noise ratio (SNR) due to the binding/unbinding of discrete analytes [14]:

$$SNR_{QL} = \frac{(n\rho_{c,E})^2}{n\rho_{c,E}(1-\rho_{c,E})} = n\frac{\rho_{c,E}}{1-\rho_{c,E}}. \tag{5.2}$$

Here, $\rho_{c,E}$ is the probability of analytes at captured state in equilibrium. Assuming there are n independent analytes in the biosensing system at equilibrium, $n\rho_{c,E}$ is the expected number of analytes captured by the binding sites. The SNR is defined as the ratio of signal power over the noise power, which is the variance of the process. Equation (5.2) can be expanded to include
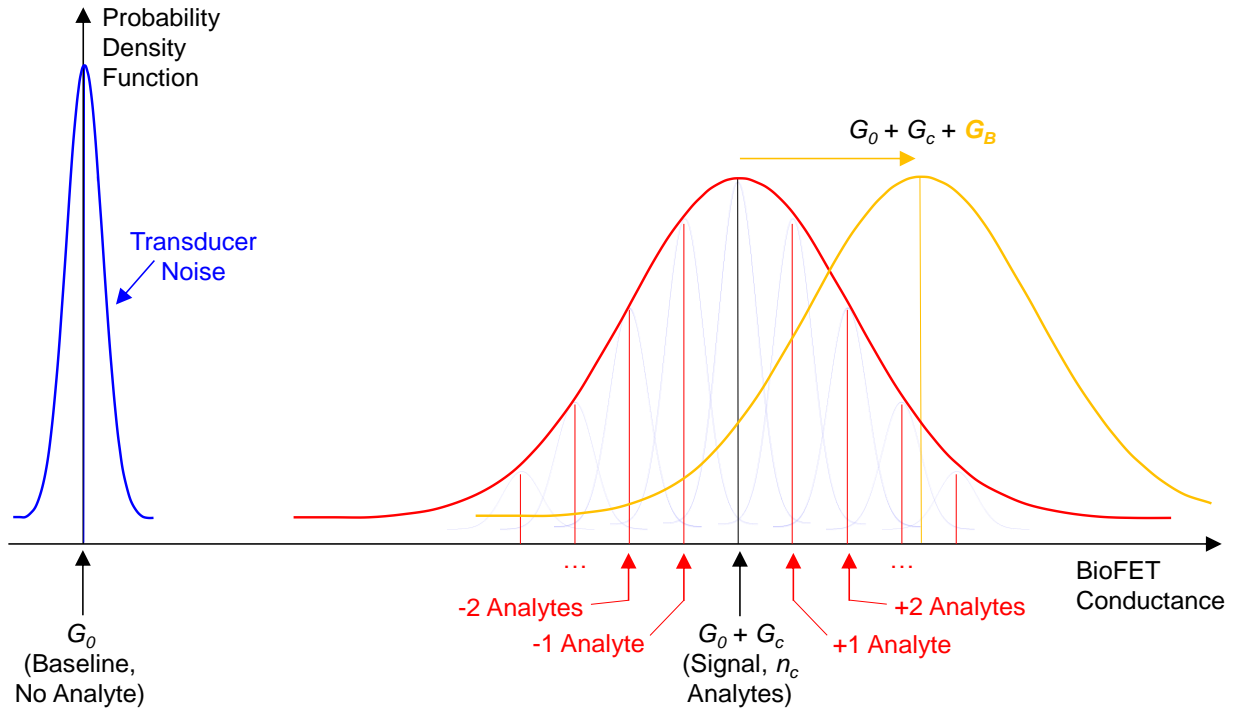
Figure 5.2. Illustration of transducer, biological and nonspecific noise in BioFETs

other noise sources. The transducer noise σ_T^2 can be taken into account, which is independent of the mass transport and binding processes. For the nonspecific noise, each of the $\tilde{n}$ background particles in the system is assumed to bind to the BioFET with probability $\tilde{\rho}_{c,E}$. The SNR with all three noise sources becomes

$$SNR = \frac{(n\rho_{c,E})^2}{n\rho_{c,E}(1-\rho_{c,E})+\tilde{n}\tilde{\rho}_{c,E}(1-\tilde{\rho}_{c,E})+\sigma_T^2}. \qquad (5.3)$$

Different from the binding of non-complementary DNA segments in the cited work [14], the nonspecific noise in this discussion refers to the general sensor response of any non-analyte changes, and appears as an offset in the sensor output.

Figure 5.2 illustrates the probability density function (PDF) of these noise sources present in the BioFET. For simplicity, we will study the device conductance at constant gate bias under equilibrium of the analyte binding reaction. For an analog FET transducer, the amplitude of the output shift is used to extract the analyte concentration. Therefore, a baseline must be established prior to the introduction of the analyte solution. In the baseline solution without analyte, the BioFET should ideally operate at G_0 with probability 1. However, due to the existence of transducer noise, fluctuations will be observed in the sensor output, resulting in the blue distribution. After the analyte binding reaches equilibrium with an average of n_c analytes captured on the BioFET, the conductance should ideally stabilize at $G_0 + G_c$. This shift G_c is the signal for the extraction of analyte concentration. However, the biological noise predicts that at any given time of measurement, there are probably a few more or less analytes binding to the biosensor, which leads to a fluctuation of the sensor conductance, as shown by the red lines in Figure 5.2. Combined with the transducer noise (light blue curves), the expected distribution of sensor conductance is the red curve. The nonspecific noise shows up in the sensor conductance

82

as an offset G_B, marked by the gold line. With all three noise sources taken into account, the final conductance distribution at equilibrium of analyte binding is illustrated by the gold curve, shifted by G_B from the red.

5.2.2 The Averaging Approach to Reduce Noise in BioFETs

Averaging is a common approach to reduce the noises in BioFETs. Depending on the device configuration, the sensor output can be averaged across different devices , multiple measurements of the same device, or internally via the device design such as the nano-grating [4, 8, 9]. From Figure 5.2, the transducer noise at the sensing baseline can be reduced via averaging, leading to the accurate reconstruction of G_0. However, the noise condition becomes more complicated after analyte is introduced. Hassibi et al. predicted a Lorentzian profile for the biological noise distribution [14]. Combined with the transducer noise, these two noises can also be readily reduced via averaging. The offset from the nonspecific noise, on the other hand, leads to the shift of PDF in Figure 5.2 that cannot be removed by averaging. The final sensor signal can be extracted as $G_c + G_N$, after averaging the sensor conductance in the baseline and analyte solutions at equilibrium. Under certain sensing conditions, this nonspecific noise shift may greatly affect the accuracy of the BioFET. For example, in a protein sensing experiment with solutions containing 1 mM NaCl and 100 µM phosphate (~ 10 nm Debye screening length), there is an uncontrollable pH difference of 0.1 or higher across the baseline and protein solutions, due to the low phosphate concentration and dissolution of carbon dioxide from air. The protein signals are in the mV-range [70]. The sensor surface has pH sensitivity of 30 mV/pH as shown in Figure 5.1a, and therefore may cause a nonspecific shift of 3 mV or higher due to the pH

difference. This random and uncontrollable shift is comparable to the signal level, and can

greatly affect the accuracy of the bioFET.

5.2.3   The Digital Biosensor with Single Serpentine NW BioFET
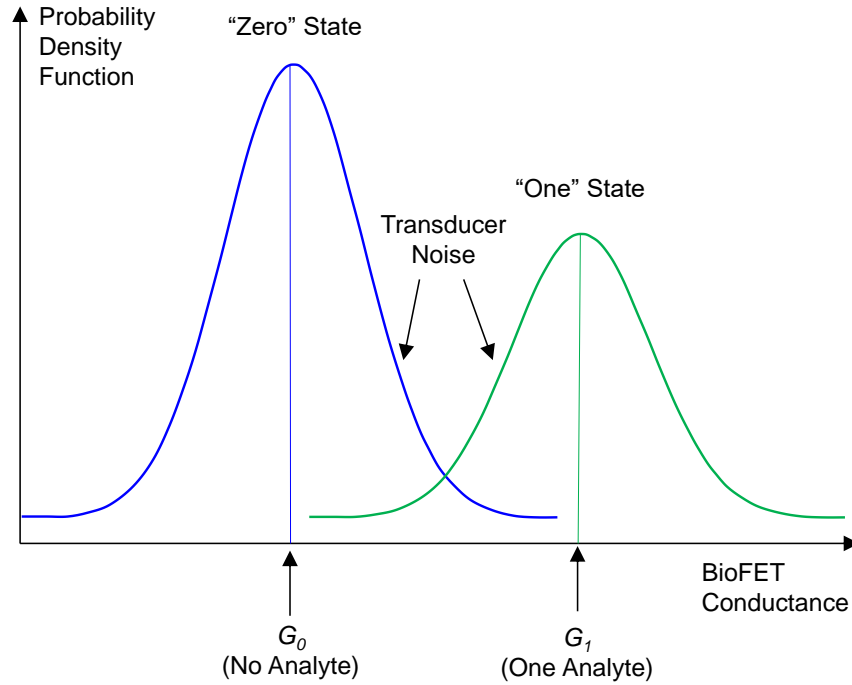
Figure 5.3. Illustration of the noises in digital biosensor

The digital biosensing idea is proposed to address the limitation from the nonspecific noise.

Assume we maintain the probe density on the NW surface by using the same surface chemistry

process, and downscale the NW dimensions until statistically only one analyte may bind to the

NW. The noise distribution will change dramatically and we no longer need a separate solution

to establish the baseline. As shown in Figure 5.3, the BioFET will have two possible states after

the analyte binding reaches equilibrium. With one analyte binding to the NW, the device is in

the "one" state with channel conductance G_1. However, even in the analyte solution, the device

will sometimes jump to the "zero" state of G_0 without analyte binding due to the random

binding/unbinding from the biological noise. For this reason, we can eliminate the baseline

establishment process prior to the analyte binding, as well as the nonspecific shift that comes

with the multiple solutions. In digital biosensing, the difference between G_1 and G_0 is no longer

characterized. Instead, the percentage of "one" state in all the measured states is used to extract

the analyte concentration via the binding curve.

To understand the binding curve, consider a general non-digital BioFET which has an active

surface of area A modified with n_p probes, each of which can bind one analyte. After the analyte

binding reaches equilibrium, there are n_c analytes on average captured by the same number of

probes. The analyte concentration c is related to n_c by the binding curve [4]. We can define the

equilibrium dissociation constant K_D:

$$k_D = \frac{([Probe]-[Probe-Analyte])[Analyte]}{[Probe-Analyte]}. \tag{5.4}$$

in which [Analyte] is the analyte volumic concentration c, [Probe] is the areal density of probes,

and [Probe-Analyte] is the areal density of the probe-analyte complex. The resulting K_D still has

the same unit of volumic concentration (*e.g.*, mole per litter) as c. Using these definitions, we

can rewrite (5.4) as

$$K_D = \frac{(n_p/A-n_c/A)c}{n_c/A} = \frac{(n_p-n_c)c}{n_c} = c\left(\frac{n_p}{n_c} - 1\right). \tag{5.5}$$

Using (5.5) we can define the surface coverage α_s:

$$\alpha_s = \frac{n_c}{n_p} = \frac{1}{1+\frac{K_D}{c}}. \tag{5.6}$$

From (5.6), we can find the relation between α_s and analyte concentration c, namely the binding

curve, as illustrated in Figure 5.4.
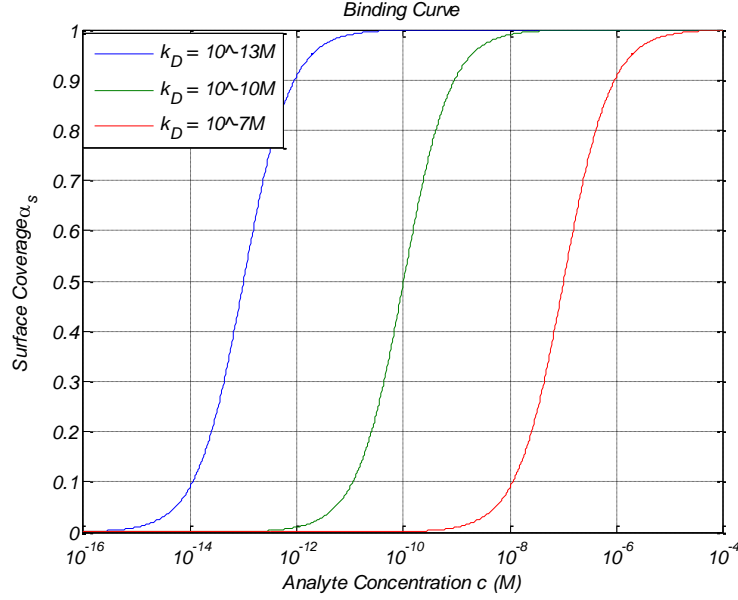
Figure 5.4. Binding curves for K_D = 100 fM, 100 pM and 100 nM

By definition, the surface coverage α_s is the ratio of the probes that capture an analyte. This is

equivalent to the probability of one probe capturing an analyte. Now, assume we evenly divide

the active area A of the BioFET into an array of n_p identical small pixels, each with one probe

that may capture one analyte. By counting the number of "one" pixels with one captured analyte

n_c, and dividing it by the total number of pixels n_p, we find the percentage of "one" pixels. By

definition, this percentage of "one" pixels or "one" states is equivalent to α_s, and therefore can be

used to extract the analyte concentration directly from the binding curve. Besides counting over

an array of identical digital biosensors, the percentage of "one" states may also be obtained from

the output of one digital biosensor counted over time. These two approaches demonstrate the

trade-off between cost (complex to fabricate and read from an array of sensors) and time (slow to

read from only one sensor). The most efficient digital biosensing will take advantage of both by

utilizing the output of an array over time. In our experimental demonstration of the digital

86

biosensor, however, we only used one sensor due to the extremely challenging fabrication and low yield.
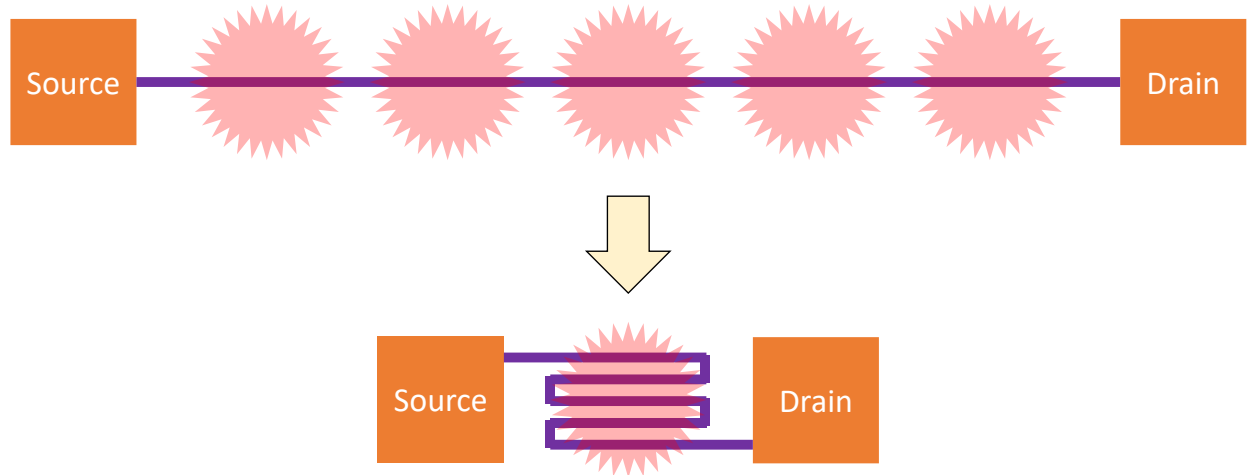
Figure 5.5. Illustration of Single Serpentine NW BioFET

The digital biosensor also brings new challenges to the transducer design. Despite the wider noise margin from the digital sensing scheme, the transducer noise must be controlled in order for the "zero" and "one" state to be differentiated, as illustrated in Figure 5.3. However, (5.1) suggests that the device noise will increase with the downscaling of the NW which, on the other hand, is required by the digital biosensor to achieve the digital detection of single analyte. To address this conflict between device scaling and noise, we proposed the design of serpentine single NW BioFET for digital biosensing. As illustrated in Figure 5.5, we "folded" a long NW into a serpentine form. This innovation of serpentine NW leads to many advantages over the previous design. First, it solves the conflict between transducer noise and device scaling. Despite the increased threshold voltage and scattering of charge carriers due to the added turns in the NW, the device noise can be maintained at a low level because the serpentine NW has the equivalent length as a long straight NW. On the other hand, the folding of NW results in a small

device footprint enough for capturing only one analyte, which is required for the digital detection of a single analyte. The small footprint also enables high integration density of multiple BioFETs in an array format. Second, the folding of NW allows one analyte to bind to multiple segments of the NW, which improves sensitivity and binding avidity. As shown in Figure 5.5, the binding of one analyte only modulates a small portion of the straight NW. For the serpentine design, however, the same analyte can modulate multiple segments that make up the bulk portion of the NW, resulting in a more significant conductance change and much higher sensitivity. Besides, the analyte binds to more binding sites at the same time on multiple segments of the NW, which increases the binding avidity. Alternatively, we may loosen the requirement on surface chemistry to achieve the same binding avidity with lower probe density. With these advantages and benefits, we believe the single serpentine NW is the perfect candidate to achieve digital biosensing with BioFETs.

5.3   Materials and Methods

5.3.1   Device Fabrication

Significant downscaling of NW cross section is required to achieve the single-analyte sensitivity, as well as to fit the serpentine NW in a small area for single-analyte binding. This poses a high risk in device fabrication. To reduce the risk and simplify the fabrication process, we utilized our existing biosensing platform previously reported [9, 81, 82]. As a brief review, these biosensor chips were fabricated on silicon-on-insulator (SOI) wafers with 70 nm top Si and 145 nm buried oxide. Photolithography defines the source/drain region, the channel region, the leads and probe pads. The source/drain region was doped by ion implantation with phosphorous to

10^{19}/cm^3, while the top Si with 10^{15}/cm^3 of boron was used as channel without further doping. The channel patterns were defined by e-beam lithography, including single nanowire, nano-grating and thin-film. These patterns were transferred to the top Si layer via a two-step dry etch process. 3 nm thermal oxide was then formed as the gate dielectric. Nickel silicide was formed on the leads and probe pads to provide connection to the device. Silicon nitride was used to passivate the chip and provide insulation on the connections, exposing only the device channel and probe pads.

Figure 5.6a illustrates the single serpentine Si NW FET, which was fabricated via further modification of the Si thin-film channel on existing BioFETs. The thin-film channels were 20 µm long, 5 µm wide and 30 nm thick. After stripping the gate oxide with diluted hydrofluoric acid, the Si thin film was patterned by e-beam lithography again to form the NW patterns for the digital biosensor. The NW pattern only takes up a small portion of the channel, so the thin film connecting the NW on each side was patterned like triangles for relatively smooth transition, as shown in Figure 5.6b. Since the NW has the smallest linewidth, it was the most sensitive spot
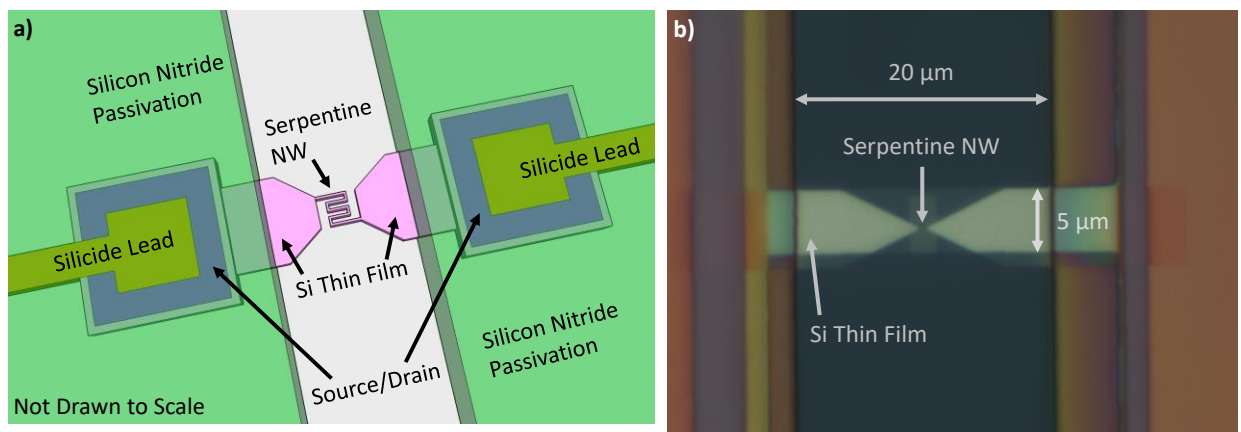
Figure 5.6. (a) 3-D illustration of the single serpentine Si NW FET, and (b) optical micrograph of the device channel. (a) is not drawn to scale.
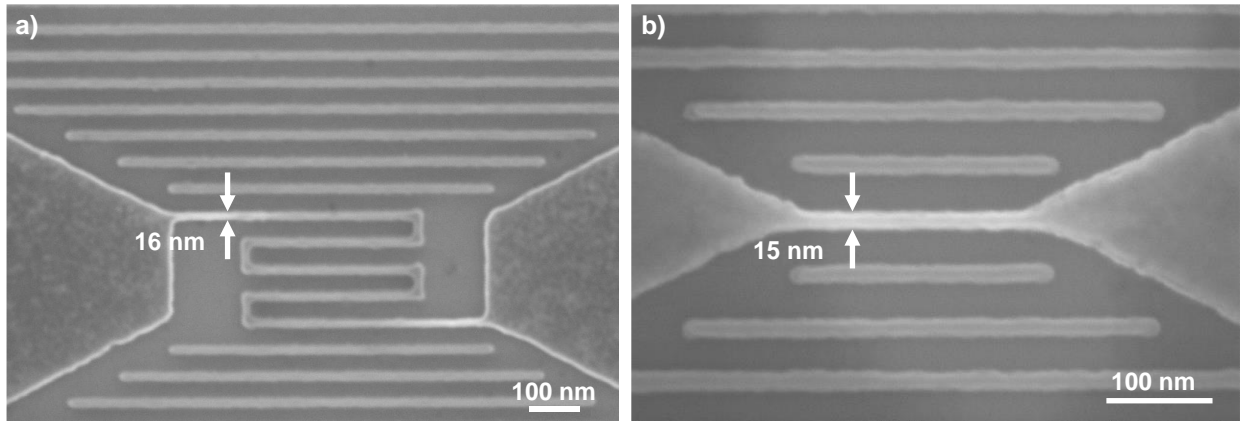
Figure 5.7. Electron Micrographs of Serpentine (a) and Straight (b) Si NW BioFET. The linewidths of both NWs are around 15 nm, and the length is 200 nm for the straight NW and 1.96 µm for the 5-fold serpentine NW.

along the device channel. To improve surface adhesion, a priming agent (SurPass 3000 from

DisChem) was applied prior to the spin-coating of hydrogen silsesquioxane (HSQ) e-beam resist.

The patterns were exposed by a Raith 150-TWO e-beam lithography system, with 10 µm

aperture, 10 mm working distance (WD) and 30 keV beam energy. The resist was then

developed in 25% TMAH at 38°C for 1 min, and dried in a Tousimis critical point dryer. After

inspection, the HSQ pattern was transferred to the Si thin film by one-step inductively-coupled

plasma (ICP) etch with chlorine chemistry. Figure 5.7a shows the etched single serpentine NW

pattern in Si. The 5-fold NW has a pitch of 50 nm, linewidth around 15 nm and total length

close to 2 µm. The gratings outside the NW region were patterned to expand the process

window for more tolerance of process variation. Figure 5.7b shows a straight NW with 200 nm

length and 15 nm linewidth, as a comparison to the serpentine design. 10 nm gate dielectric was

formed via atomic layer deposition of Al_2O_3 at 250°C, followed by forming gas annealing at

400°C for 1 hour.

90

5.3.2 Surface Modification and Solution Preparation

Due to the limitation of the critical dimension in our device fabrication, the size of the analyte

should be over tens of nanometers. Therefore, we chose the similar antibody – influenza A virus

chemistry which had been proven in single-analyte detection with BioFET [7]. The anti-

influenza A virus hemagglutinin (anti-HA) antibody (mouse monoclonal IgG1) was purchased

from Abcam. According to the manufacturer, it was tested positive for the H1N1 strain (A/New

Caledonia/20/99, inactivated) we purchased from ProSpec. The viral particle concentration was

approximately 3×10^{10} per ml according to ProSpec. We also purchased a secondary antibody

(polyclonal anti-mouse IgG) with 10 nm gold particle to label the primary anti-HA antibody.
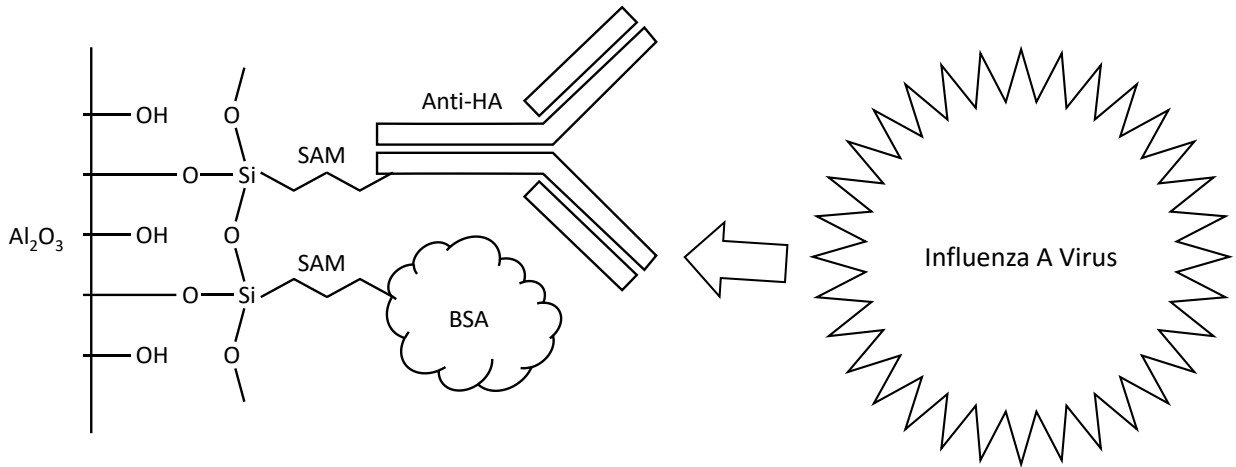
Figure 5.8. Al_2O_3 functionalized with anti-HA for virus detection

To functionalize the NW surface for virus detection, the Al_2O_3 surface was cleaned in ozone at

200°C for 30 min, followed by the immobilization of self-assembled monolayer (SAM). Two

SAM surface chemistries were used. In our well-developed SAM process, the chip was

incubated with 0.1% 11-(triethoxysilyl)undecanal (TESU) in toluene for 5 hrs [8]. We also tried

the SAM process reported for the CVD NW BioFET [7, 83]. In this process, the chip was

incubated with 1% trimethoxysilyl alkyl aldehyde in 190-proof ethyl alcohol for 30 mins, and

then heated to 120°C for 15 min. In the antibody modification, the chip was incubated with 50

µg/ml anti-HA in 10 mM potassium phosphate buffer (KPB) at pH 8.4 with 4 mM $NaCNBH_3$ for

3 hrs. Then, the non-reacted aldehyde groups were passivated by 10 µg/ml BSA in the same

KPB solution with $NaCNBH_3$ for 3 hrs. Figure 5.8 illustrates the functionalized Al_2O_3 surface

for the detection of influenza A virus.

We were able to achieve antibody density in the range of $0.6 – 1 \times 10^{11}/cm^2$ with both SAMs,

although with TESU the antibody density appeared to be slightly higher. Figure 5.9a shows the

electron micrograph of anti-HA-modified surface with TESU chemistry, labeled with gold-

tagged secondary antibody. The density was estimated to be $1.07 \times 10^{11}/cm^2$, which was one-order

lower than the one reported for the CVD NW BioFET [7]. However, owing to the serpentine

nanowire design, the lower antibody density can be compensated by the binding to the multiple

segments of the NW, as discussed before.
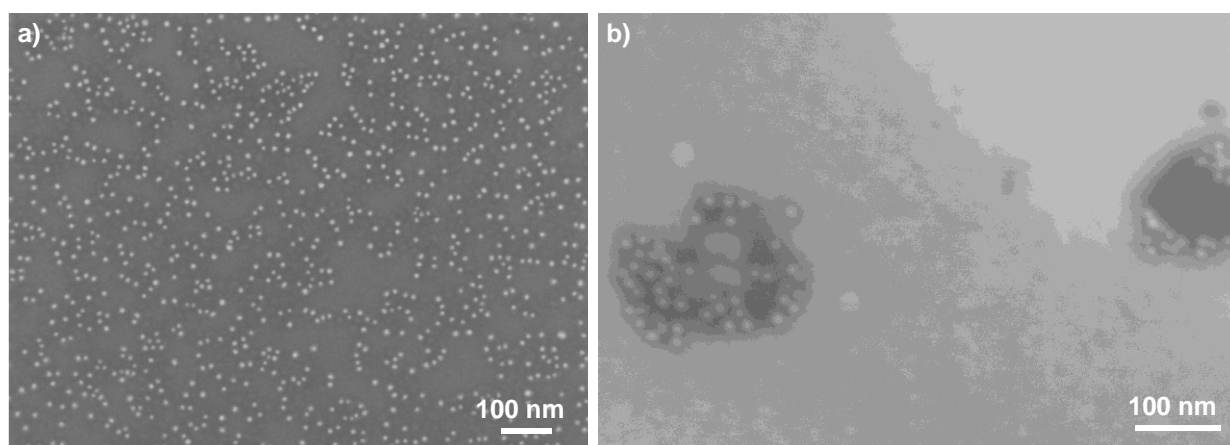
Figure 5.9. Characterization of Anti-Influenza A Hemagglutinin Antibody – H1N1 Chemistry. (a) Electron micrograph of immobilized anti-HA antibodies on Al_2O_3 surface, labeled with gold-tagged secondary antibody. The gold particle density was estimated to be $1.07 \times 10^{11}/cm^2$; (b) Electron micrograph of H1N1 virus incubated with anti-HA antibody, and labeled with the same secondary antibody

92

Although it was tested positive by the manufacturer, the binding between the antibody and virus was verified experimentally. As shown in Figure 5.9b, the virus was immobilized on the SAM-modified surface, followed by BSA passivation of the aldehyde groups. After that, the virus was incubated with the anti-HA antibody, which was then labeled by the gold-tagged secondary antibody. The high density of gold particles exclusively on the dark viral fragments was the proof of antibody-virus binding.

The size of influenza A virus is typically in the range of 80 – 120 nm. Therefore, 10 µM ionic strength is adequate for the sensing solutions as the resulting Debye screening length is roughly 30 nm. Zeta potential measurements suggested the virus was negatively charged in pH 7.94, and pH 5.41 was close to the isoelectric point (pI). We discovered that phosphate at 10 µM had very low buffer capacity, and could barely stabilize the pH due to the dissolution of CO_2 from air. Eventually we were able to achieve pH 8.17 with KOH at approximately 10 µM level. The stock virus solution was diluted to 9,000, 900 and 90 viral particles per micro liter with the KOH solution. According to the manufacturer, the virus came in STE buffer with 0.1 % sodium azide and 0.005 % thimerosal. After the dilution, the STE concentration in the 9,000/µL solution should be approximately at the similar level as the KOH. However, because digital biosensing relies on the count of binding states instead of the output amplitude, there was no need to equalize the pH or ionic strength across the sensing solutions.

5.3.3   The Biosensing Setup

The biosensor chip was fixed on a 3D-printed clamp with Ag/AgCl solution gate in a PDMS fluidic channel [81, 82], and a syringe pump delivered the virus solutions to the biosensor at 0.15 ml/hr. The electrical measurements were carried out by a Keithley 4200-SCS semiconductor

characterization system with a Cascade-Microtech probe station. The drain-source voltage was set to 0.1 V. To find the biasing point in the subthreshold regime, the transfer characteristic was measured by sweeping the gate voltage. Then, the device was biased at a constant gate voltage, and drain/source currents were recorded while flowing the virus solution through the fluidic channel.

5.4   Results and Discussion

Figure 5.10a shows the transfer characteristics of both serpentine and straight single Si NW FET we fabricated. We did not sweep the gate voltage beyond 3 V into the linear regime, due to the risk of gate oxide breakdown at high voltages. Nevertheless, the subthreshold regime was adequate for our study because of the optimal sensitivity [24]. The straight NW shows slightly smaller subthreshold swing of 180 mV/Dec, compared to the serpentine NW of 200 mV/Dec. Due to the one-order increase in the equivalent length of the NWs (1.96 µm versus 200 nm), the serpentine NW demonstrates roughly one-order smaller current than the straight NW at 3 V gate
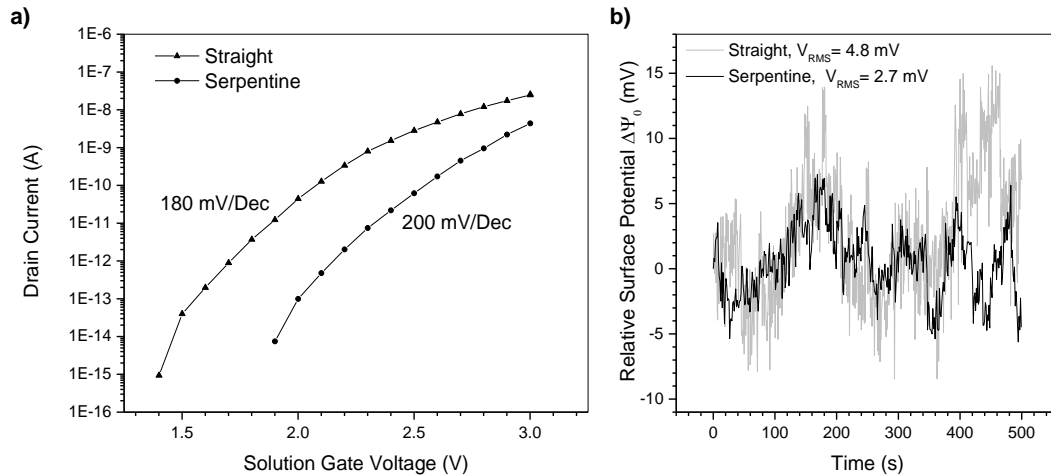
Figure 5.10. Transfer Characteristics (a) and RMS Noise (b) of Serpentine and Straight Si NWFETs. The devices were biased by a Ag/AgCl electrode in DI water saturated with air.

voltage. The serpentine *I-V* curve also shifts in the positive direction by 0.4 V. This suggests an increase of the threshold voltage, likely caused by the turns in the serpentine NW. From the transfer characteristics, we biased the devices in the 10^{-11} A current level for virus sensing. Figure 5.10b shows the gate-voltage-referred noise of both devices measured over 500s in de-ionized (DI) water. The serpentine device clearly shows a lower noise level than the straight. However, the change of noise power from 23.04 mV^2 to 7.29 mV^2 doesn't quite follow (5.1). One possible reason is the additional electron scattering from the turns and change of crystalline orientation in the serpentine NW. Nevertheless, the serpentine NW with similar footprint still demonstrates lower noise level than the straight NW, which is essential in the achievement of digital biosensing with NW BioFETs.

The virus sensing result with the straight NW FET is inconclusive for the digital detection of virus, and therefore not shown. Due to the large transducer noise, we were unable to differentiate the virus binding peaks positively. On the other hand, the virus binding probability was quite low due to the small active area on the straight NW. As a quantitative estimation, the NW linewidth is assumed to increase by 10 nm on each side after Al_2O_3 deposition, resulting in an active area of 35 nm by 200 nm. With 1×10^{11}/cm^2 antibody density, there are roughly 7 antibodies scattered over the 200 nm-long NW. As the virus size is in the range of 80 – 120 nm, at most 5 of the 7 antibodies may actually contribute to the virus binding. This weak binding leads to a large equilibrium dissociation constant K_D, and according to the binding curve, the binding probability α_s will be quite low. In comparison, if we make the same linewidth assumption for the serpentine NW, there will be only a 15 nm gap between the adjacent parallel segments of the NW, resulting in a significant increase of coverage in the area. The number of

binding antibodies may double or even triple depending on the binding location and virus size.

Besides, the longer serpentine NW suffers less from the variation of the antibody density.

Consequently, the binding avidity of serpentine biosensor is greatly enhanced.
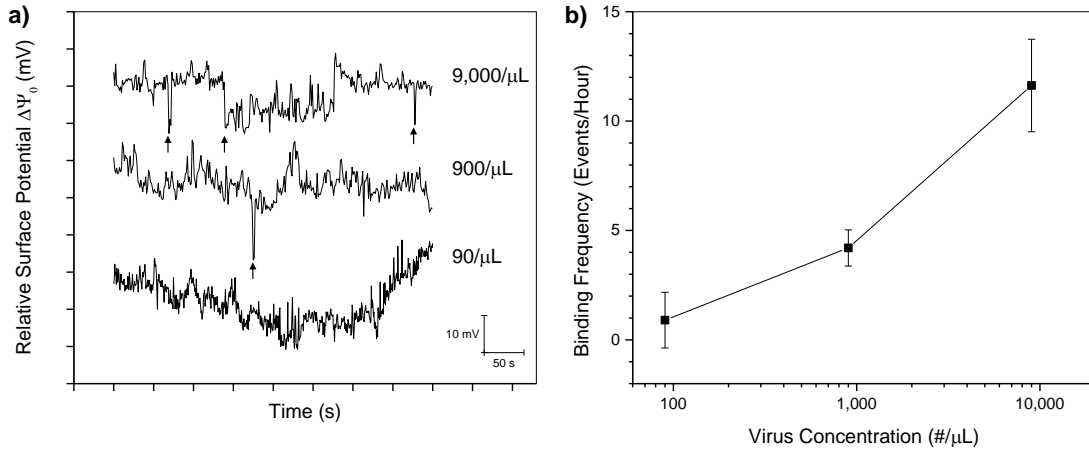
Figure 5.11. Influenza Virus Sensing Results of the Serpentine Nanowire FET Modified with Anti-Influenza A Hemagglutinin Antibody. (a) Exemplary raw sensor output at three different viral concentrations; (b) Plot of the binding frequency vs the viral concentration, showing a monotonic relationship.

Figure 5.11a shows the raw sensing results of single serpentine NW FET. The channel

conductance at three different virus concentrations is converted to surface potential for direct

comparison. As the virus concentration increases, the binding events can be observed more

frequently in the sensor output, as indicated by the arrows. Thanks to the reduced transducer

noise, these binding peaks can be identified with certainty. Practically there are two approaches

to extract the probability of "one" state from the sensing result. In Figure 5.11b, the frequency of

the binding events is summarized for each concentration, and results from multiple

measurements are used to generate the error bars. A monotonic relation between virus

concentration and binding frequency can be clearly observed. In comparison to the published

results of the CVD NW BioFET [7], the binding frequency here is approximately one-order lower for the same virus concentration. The small footprint of the serpentine NW is likely the primary cause. Despite the similar total length, the straight CVD NW spans over 2 µm, and therefore has a higher probability of interaction with viral particles from the mass-transport process. The other approach is to study the distribution of the two states. Figure 5.12 shows the histogram of the serpentine NW FET conductance at two higher virus concentrations. Due to the low frequency drifting of the baseline, measurements over 650s are used for the generation of the plot. A separate virus binding state can be clearly identified for the 9,000/µL concentration. At 900/µL, the distribution height for the binding state reduces notably. We didn't plot the histogram for 90/µL because the binding state can no longer be identified. Due to the limited data points and small binding state at the lower concentrations, the data is not further processed. However, with enough data points, the two states can be reconstructed accurately by fitting the histogram to known distributions, such as Gaussian, and the relative height of the distribution is linked to the analyte concentration via binding curve [80].

From Figure 5.11 and Figure 5.12, we can see that digital biosensing relies on the statistical analysis of the sensor output, and thus demands considerable amount of data to achieve high sensing accuracy. The dual-state nature of the digital BioFET requires long measurement to recover the accurate ratio of the states. The long measurement may also lead to device stability problem. To reduce the response time, multiplex detection may be utilized with an array of identical digital BioFETs. Here, we defined the single serpentine NW FET using the top-down (lithography) approach, which is compatible with the industrial semiconductor processes, and enables integration into an array format with other peripheral circuits. It is not feasible, however,

to synthesize the serpentine NW with the bottom-up (CVD) approach, which has no control over the NW bending.

In this work, we did not study the selectivity of the digital BioFET by sensing a non-binding virus, mainly due to the low sampling rate of our setup. However, the CVD NW BioFET work suggests that as the non-binding virus passes by and/or rapidly touches the NW, the device demonstrates different temporal behavior of shorter conductance change that can be readily distinguished. Therefore, it is feasible to detect "dirty" samples with nonspecific species using digital BioFETs. In addition, machine learning has been demonstrated as a robust tool and can be used for the identification of the specific binding signals from the huge amount of digital sensing data [84].
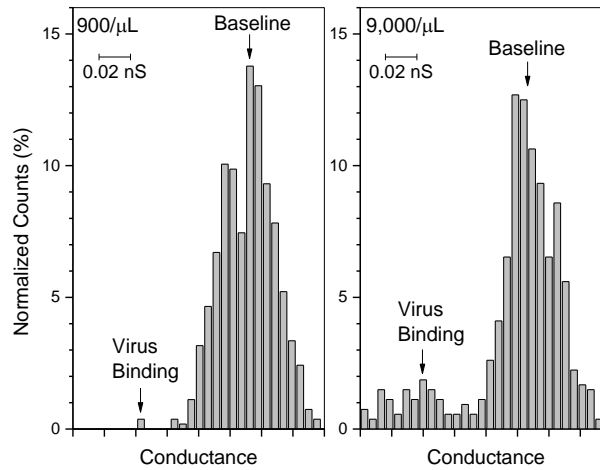
Figure 5.12. Histogram of Influenza Virus Sensing Results with Single Serpentine NW Digital BioFET. The histogram is generated from time-resolved measurements over 650 s at the concentrations of 900 and 9,000 viral particles per micro liter.

5.5   Conclusion

We demonstrate the great potential of the serpentine NW design as the perfect candidate to

achieve digital biosensing with NW BioFETs. The lower transducer noise of 2.7 mV compared to 4.8 mV of straight NW contributes to the differentiation of the binding and nonbinding states with viral concentration ranging from 90/µL to 9,000/µL. The small footprint not only guarantees single-analyte detection required by the digital biosensor, but also enables high-density device integration. The serpentine channel design allows the analyte to bind to multiple segments of the NW, which improves the binding avidity from the increased binding area, as well as the analyte sensitivity due to the increased modulation. Multiplex digital biosensing can be achieved with an array of digital BioFETs, which has a promising future as a novel platform for real-time, highly accurate and low-cost biosensing.

CHAPTER 6

CONCLUSION AND FUTURE WORK

In summary, this dissertation covered the study of Si NW FET in several aspects of biosensing.

Chapter 2 focused on the hydrolytic stability issue of the surface species as the sensing elements.

Contrary to one's intuition, despite the slight reduction of sensitivity, the overall performance of

the nano-grating pH sensor was greatly improved in terms of detection accuracy, after the

removal of loosely bound sensing elements by the hydrolysis process. In Chapter 3, a new

differential biosensing approach was reported to suppress noise in solution potential with a

secondary reference electrode. Compared to a secondary reference FET, this approach greatly

simplified the system setup, while improved the signal integrity resulting in a 50 – 70%

reduction of limit of detection. Chapter 4 studied the buffering effect of analyte charges by the

protonation and deprotonation of hydroxyl groups on the sensing surface. Coupled by the

surface potential, the high density of surface hydroxyl groups results in a high pH sensitivity,

which significantly compensate for the change of surface charge due to the binding of charged

analytes. In addition, the analyte sensitivity also heavily depends on the buffer capacity of the

analytes. Chapter 5 introduced the new digital biosensing concept to the biological FET.

Existing analog FET transducers utilized the amplitude of the sensor output, determined by the

immobilized analyte density on the sensor surface. With digital FET biosensor, the binding

event of individual analyte is counted and statistically analyzed to determine the analyte

concentration. The single serpentine NW FET was proposed as a potential candidate to achieve

digital biosensing. While maintaining the low device noise, the small footprint enables binding

of a single analyte required by the digital counting, and leads to high integration density of the

digital FET biosensors. In addition, with analyte binding to multiple segments of the NW, both the analyte sensitivity and the binding avidity can be improved. By integration of single serpentine NW FETs into an array format, the digital biosensor has great potential as a highly accurate, real-time and cost-effective biosensing platform.

Several topics can be extended from the studies in this dissertation, which are interesting to explore in the future. Chapter 4 involved analytical derivations and numerical simulations to study the charge buffering by the hydroxyl groups. It will be interesting to verify this effect directly via experiments, by tuning the available hydroxyl group density via passivation with a self-assembled monolayer. Extending from Chapter 5, the interaction of single serpentine NW FET with non-target virus may be researched. This requires the improvement of the device setup for a higher sampling frequency, as the duration is likely shorter than the target analyte. Besides, an array of digital FET biosensors with peripheral circuits may be designed and fabricated to achieve the higher data throughput for reduced response time. It may also be used for real-time "imaging" of the analyte spatial distribution.

REFERENCES

[1]   F. Patolsky, G. Zheng, and C. M. Lieber, "Nanowire-based biosensors," *Analytical Chemistry,* vol. 78, pp. 4260-4269, 2006.

[2]   F. Patolsky and C. M. Lieber, "Nanowire nanosensors," *Materials Today,* vol. 8, pp. 20-28, 2005.

[3]   M.-Y. Shen, B.-R. Li, and Y.-K. Li, "Silicon nanowire field-effect-transistor based biosensors: From sensitive to ultra-sensitive," *Biosensors and Bioelectronics,* vol. 60, pp. 101-111, 10/15/2014.

[4]   N. K. Rajan, X. Duan, and M. A. Reed, "Performance limitations for nanowire/nanoribbon biosensors," *Wiley Interdisciplinary Reviews: Nanomedicine and Nanobiotechnology,* vol. 5, pp. 629-645, 2013.

[5]   E. Stern, J. F. Klemic, D. A. Routenberg, P. N. Wyrembak, D. B. Turner-Evans, A. D. Hamilton*, et al.*, "Label-free immunodetection with CMOS-compatible semiconducting nanowires," *Nature,* vol. 445, pp. 519-522, 02/01/print 2007.

[6]   M. Curreli, Z. Rui, F. N. Ishikawa, H.-K. Chang, R. J. Cote, Z. Chongwu*, et al.*, "Real-Time, Label-Free Detection of Biological Entities Using Nanowire-Based FETs," *Nanotechnology, IEEE Transactions on,* vol. 7, pp. 651-667, 2008.

[7]   F. Patolsky, G. Zheng, O. Hayden, M. Lakadamyali, X. Zhuang, and C. M. Lieber, "Electrical detection of single viruses," *Proceedings of the National Academy of Sciences of the United States of America,* vol. 101, pp. 14017-14022, September 28, 2004.

[8]   R. Tian, S. Regonda, J. Gao, Y. Liu, and W. Hu, "Ultrasensitive protein detection using lithographically defined Si multi-nanowire field effect transistors," *Lab on a Chip,* vol. 11, pp. 1952-1961, 2011.

[9]   S. Regonda, R. Tian, J. Gao, S. Greene, J. Ding, and W. Hu, "Silicon multi-nanochannel FETs to improve device uniformity/stability and femtomolar detection of insulin in serum," *Biosensors and Bioelectronics,* vol. 45, pp. 245-251, 7/15/2013.

[10]   P. Bergveld, "Development of an Ion-Sensitive Solid-State Device for Neurophysiological Measurements," *Biomedical Engineering, IEEE Transactions on,* vol. BME-17, pp. 70-71, 1970.

[11]   P. Bergveld, "ISFET, theory and practice," in *IEEE Sensor Conference Toronto*, p. 1, 2003.

[12]   M. C. Goldschmidt, "BIOSENSORS: BLESSING OR BANE?," *Journal of Rapid Methods & Automation in Microbiology,* vol. 2, pp. 9-15, 1993.

[13] K. Rogers, "Principles of affinity-based biosensors," *Molecular Biotechnology,* vol. 14, pp. 109-129, 2000.

[14] A. Hassibi, S. Zahedi, R. Navid, R. W. Dutton, and T. H. Lee, "Biological shot-noise and quantum-limited signal-to-noise ratio in affinity-based biosensors," *Journal of Applied Physics,* vol. 97, 2005.

[15] G. S. Kulkarni and Z. Zhong, "Detection beyond the Debye Screening Length in a High-Frequency Nanoelectronic Biosensor," *Nano Letters,* vol. 12, pp. 719-723, 2012.

[16] C. M. M. P. A. Sensors, B. M. E. Design, D. E. P. Sciences, and N. R. Council, *Sensor Systems for Biological Agent Attacks:: Protecting Buildings and Military Bases*: National Academies Press, 2005.

[17] X. Yang, "Performance analysis of Silicon nanowire biosensor - a modeling and simulation approach," 3600540 Ph.D., The University of Texas at Dallas, Ann Arbor, 2012.

[18] J.-K. Shin, D.-S. Kim, H.-J. Park, and G. Lim, "Detection of DNA and Protein Molecules Using an FET-Type Biosensor with Gold as a Gate Metal," *Electroanalysis,* vol. 16, pp. 1912-1918, 2004.

[19] P. B. Luppa, L. J. Sokoll, and D. W. Chan, "Immunosensors—principles and applications to clinical chemistry," *Clinica Chimica Acta,* vol. 314, pp. 1-26, 2001.

[20] S. Dübel, "Therapeutic Antibodies - From Past to Future," in *Handbook of Therapeutic Antibodies*, ed: Wiley-VCH Verlag GmbH, pp. 2-16, 2008.

[21] C. Janeway, *Immunobiology five*: Garland Pub., 2001.

[22] M. d. Vestergaard, K. Kerman, and E. Tamiya, "An Overview of Label-free Electrochemical Protein Sensors," *Sensors,* vol. 7, pp. 3442-3458, 2007.

[23] B. Sikarwar, P. K. Sharma, A. Srivastava, G. S. Agarwal, M. Boopathi, B. Singh*, et al.*, "Surface plasmon resonance characterization of monoclonal and polyclonal antibodies of malaria for biosensor applications," *Biosensors and Bioelectronics,* vol. 60, pp. 201-209, 10/15/2014.

[24] X. P. A. Gao, G. Zheng, and C. M. Lieber, "Subthreshold Regime has the Optimal Sensitivity for Nanowire FET Biosensors," *Nano Letters,* vol. 10, pp. 547-552, 2009.

[25] A. Kim, C. S. Ah, C. W. Park, J.-H. Yang, T. Kim, C.-G. Ahn*, et al.*, "Direct label-free electrical immunodetection in human serum using a flow-through-apparatus approach with integrated field-effect transistors," *Biosensors and Bioelectronics,* vol. 25, pp. 1767-1773, 3/15/2010.

[26] A. Kim, C. S. Ah, H. Y. Yu, J.-H. Yang, I.-B. Baek, C.-G. Ahn*, et al.*, "Ultrasensitive, label-free, and real-time immunodetection using silicon field-effect transistors," *Applied Physics Letters,* vol. 91, p. 103901, 2007.

[27] M. Lee, N. Zine, A. Baraket, M. Zabala, F. Campabadal, M. G. Trivella*, et al.*, "Novel Capacitance Biosensor Based on Hafnium Oxide for Interleukin-10 Protein Detection," *Procedia Engineering,* vol. 25, pp. 972-975, 2011.

[28] G. Zheng, X. P. A. Gao, and C. M. Lieber, "Frequency Domain Detection of Biomolecules Using Silicon Nanowire Biosensors," *Nano Letters,* vol. 10, pp. 3179-3183, 2010.

[29] G. Zheng, F. Patolsky, Y. Cui, W. U. Wang, and C. M. Lieber, "Multiplexed electrical detection of cancer markers with nanowire sensor arrays," *Nat Biotech,* vol. 23, pp. 1294-1301, 2005.

[30] Y. Cui, Q. Wei, H. Park, and C. M. Lieber, "Nanowire Nanosensors for Highly Sensitive and Selective Detection of Biological and Chemical Species," *Science,* vol. 293, pp. 1289-1292, 08/17/2001.

[31] K.-I. Chen, B.-R. Li, and Y.-T. Chen, "Silicon nanowire field-effect transistor-based biosensors for biomedical diagnosis and cellular recording investigation," *Nano Today,* vol. 6, pp. 131-154, 2011.

[32] D. Grieshaber, R. MacKenzie, J. Voeroes, and E. Reimhult, "Electrochemical biosensors-sensor principles and architectures," *Sensors,* vol. 8, pp. 1400-1458, 2008.

[33] X. Yang, W. R. Frensley, D. Zhou, and W. Hu, "Performance Analysis of Si Nanowire Biosensor by Numerical Modeling for Charge Sensing," *Nanotechnology, IEEE Transactions on,* vol. 11, pp. 501-512, 2012.

[34] N. Elfström, R. Juhasz, I. Sychugov, T. Engfeldt, A. E. Karlström, and J. Linnros, "Surface Charge Sensitivity of Silicon Nanowires: Size Dependence," *Nano Letters,* vol. 7, pp. 2608-2612, 2007.

[35] O. Knopfmacher, A. Tarasov, W. Fu, M. Wipf, B. Niesen, M. Calame*, et al.*, "Nernst limit in dual-gated Si-nanowire FET sensors," *Nano Lett,* vol. 10, pp. 2268-74, 6/9/2010.

[36] N. Couniot, A. Afzalian, and D. Flandre, "Scaling laws and performance improvements of integrated biosensor microarrays with multi-pixel per spot," *Sensors and Actuators B: Chemical,* vol. 166–167, pp. 184-192, 5/20/2012.

[37] S. M. Sze and K. K. Ng, *Physics of Semiconductor Devices*: Wiley, 2006.

[38] S. Yoshinori and K. Hiroshi, "Low drift and small hysteresis characteristics of diamond electrolyte-solution-gate FET," *Journal of Physics D: Applied Physics,* vol. 43, p. 374020, 2010.

[39] L. Bousse, H. H. van den Vlekkert, and N. F. de Rooij, "Hysteresis in Al2O3-gate ISFETs," *Sensors and Actuators B: Chemical,* vol. 2, pp. 103-110, 1990.

[40] L. Bousse, S. Mostarshed, B. van der Schoot, and N. F. de Rooij, "Comparison of the hysteresis of Ta2O5 and Si3N4 pH-sensing insulators," *Sensors and Actuators B: Chemical,* vol. 17, pp. 157-164, 1994.

[41] L. Bousse and P. Bergveld, "The role of buried OH sites in the response mechanism of inorganic-gate pH-sensitive ISFETs," *Sensors and Actuators,* vol. 6, pp. 65-78, 1984.

[42] S. Caras and J. Janata, "Field effect transistor sensitive to penicillin," *Analytical Chemistry,* vol. 52, pp. 1935-1937, 1980.

[43] P. Bergveld, R. E. G. van Hal, and J. C. T. Eijkel, "The remarkable similarity between the acid-base properties of ISFETs and proteins and the consequences for the design of ISFET biosensors," *Biosensors and Bioelectronics,* vol. 10, pp. 405-414, 1995.

[44] B. R. Dorvel, B. Reddy, J. Go, C. Duarte Guevara, E. Salm, M. A. Alam*, et al.*, "Silicon Nanowires with High-k Hafnium Oxide Dielectrics for Sensitive Detection of Small Nucleic Acid Oligomers," *ACS Nano,* vol. 6, pp. 6150-6164, 2012.

[45] M. Wipf, "Chemical and biochemical sensors based on silicon nanowire field-effect transistor arrays," University of Basel, 2014.

[46] A. Vacic, J. M. Criscione, E. Stern, N. K. Rajan, T. Fahmy, and M. A. Reed, "Multiplexed SOI BioFETs," *Biosensors and Bioelectronics,* vol. 28, pp. 239-242, 10/15/2011.

[47] Z. Gao, A. Agarwal, A. D. Trigg, N. Singh, C. Fang, C.-H. Tung*, et al.*, "Silicon Nanowire Arrays for Label-Free Detection of DNA," *Analytical Chemistry,* vol. 79, pp. 3291-3297, 2007.

[48] B.-R. Li, C.-W. Chen, W.-L. Yang, T.-Y. Lin, C.-Y. Pan, and Y.-T. Chen, "Biomolecular recognition with a sensitivity-enhanced nanowire transistor biosensor," *Biosensors and Bioelectronics,* vol. 45, pp. 252-259, 7/15/2013.

[49] D. Niwa, K. Omichi, N. Motohashi, T. Homma, and T. Osaka, "Organosilane self-assembled monolayer-modified field effect transistors for on-chip ion and biomolecule sensing," *Sensors and Actuators B: Chemical,* vol. 108, pp. 721-726, 2005.

[50] Y. Chen, X. Wang, S. Erramilli, P. Mohanty, and A. Kalinowski, "Silicon-based nanoelectronic field-effect pH sensor with local gate control," *Applied Physics Letters,* vol. 89, 2006.

[51] O. H. Elibol, D. Morisette, D. Akin, J. P. Denton, and R. Bashir, "Integrated nanoscale silicon sensors using top-down fabrication," *Applied Physics Letters,* vol. 83, pp. 4613-4615, 2003.

[52] Z. Li, B. Rajendran, T. I. Kamins, X. Li, Y. Chen, and R. S. Williams, "Silicon nanowires for sequence-specific DNA sensing: device fabrication and simulation," *Applied Physics A,* vol. 80, pp. 1257-1263, 2005.

[53] K.-S. Shin, L. Kyunghoon, K. Ji Yoon, and C. Chi On, "Novel T-channel nanowire FET with built-in signal amplification for pH sensing," in *Electron Devices Meeting (IEDM), 2009 IEEE International*, pp. 1-4, 2009.

[54] A. Tarasov, M. Wipf, R. L. Stoop, K. Bedner, W. Fu, V. A. Guzenko*, et al.*, "Understanding the Electrolyte Background for Biochemical Sensing with Ion-Sensitive Field-Effect Transistors," *ACS Nano,* vol. 6, pp. 9291-9298, 2012.

[55] K. Trivedi, H. Yuk, H. C. Floresca, M. J. Kim, and W. Hu, "Quantum Confinement Induced Performance Enhancement in Sub-5-nm Lithographic Si Nanowire Transistors," *Nano Letters,* vol. 11, pp. 1412-1417, 2011.

[56] E. Stern, A. Vacic, C. Li, F. N. Ishikawa, C. Zhou, M. A. Reed*, et al.*, "A Nanoelectronic Enzyme-Linked Immunosorbent Assay for Detection of Proteins in Physiological Solutions," *Small,* vol. 6, pp. 232-238, 2010.

[57] M. Margulies, M. Egholm, W. E. Altman, S. Attiya, J. S. Bader, L. A. Bemben*, et al.*, "Genome sequencing in microfabricated high-density picolitre reactors," *Nature,* vol. 437, pp. 376-380, 09/15/2005.

[58] T. Sakata and Y. Miyahara, "DNA Sequencing Based on Intrinsic Molecular Charges," *Angewandte Chemie International Edition,* vol. 45, pp. 2225-2228, 2006.

[59] S. Fiorilli, P. Rivolo, E. Descrovi, C. Ricciardi, L. Pasquardini, L. Lunelli*, et al.*, "Vapor-phase self-assembled monolayers of aminosilane on plasma-activated silicon substrates," *Journal of Colloid and Interface Science,* vol. 321, pp. 235-241, 5/1/2008.

[60] F. Zhang, K. Sautter, A. M. Larsen, D. A. Findley, R. C. Davis, H. Samha*, et al.*, "Chemical Vapor Deposition of Three Aminosilanes on Silicon Dioxide: Surface Characterization, Stability, Effects of Silane Concentration, and Cyanine Dye Adsorption," *Langmuir,* vol. 26, pp. 14648-14654, 2010.

[61]   A. Y. Fadeev and T. J. McCarthy, "Self-Assembly Is Not the Only Reaction Possible between Alkyltrichlorosilanes and Surfaces: Monomolecular and Oligomeric Covalently Attached Layers of Dichloro- and Trichloroalkylsilanes on Silicon," *Langmuir,* vol. 16, pp. 7268-7274, 2000.

[62]   M. Zhu, M. Z. Lerum, and W. Chen, "How To Prepare Reproducible, Homogeneous, and Hydrolytically Stable Aminosilane-Derived Layers on Silica," *Langmuir,* vol. 28, pp. 416-423, 2011.

[63]   P. Zang, Y. Liang, L. Spurgin, and W. Hu, "pH sensing comparison of vapor and solution APTES coated Si nanograting FETs," in *Nanotechnology (IEEE-NANO), 2013 13th IEEE Conference on*, pp. 301-304, 2013.

[64]   M. Etienne and A. Walcarius, "Analytical investigation of the chemical reactivity and stability of aminopropyl-grafted silica in aqueous medium," *Talanta,* vol. 59, pp. 1173-1188, 5/1/2003.

[65]   C.-S. Lee, S. Kim, and M. Kim, "Ion-Sensitive Field-Effect Transistor for Biological Sensing," *Sensors,* vol. 9, pp. 7111-7131, 2009.

[66]   A. Tarasov, M. Wipf, K. Bedner, J. Kurz, W. Fu, V. A. Guzenko*, et al.*, "True Reference Nanosensor Realized with Silicon Nanowires," *Langmuir,* vol. 28, pp. 9899-9905, 2012.

[67]   O. Knopfmacher, A. Tarasov, M. Wipf, W. Fu, M. Calame, and C. Schönenberger, "Silicon-Based Ion-Sensitive Field-Effect Transistor Shows Negligible Dependence on Salt Concentration at Constant pH," *ChemPhysChem,* vol. 13, pp. 1157-1160, 2012.

[68]   G. L. Long and J. D. Winefordner, "Limit of Detection A Closer Look at the IUPAC Definition," *Analytical Chemistry,* vol. 55, pp. 712A-724A, 1983.

[69]   P. Bergveld, "Thirty years of ISFETOLOGY: What happened in the past 30 years and what may happen in the next 30 years," *Sensors and Actuators B: Chemical,* vol. 88, pp. 1-20, 1/1/2003.

[70]   P. Bergveld, "A critical evaluation of direct electrical protein detection methods," *Biosensors and Bioelectronics,* vol. 6, pp. 55-72, 1991.

[71]   R. Schasfoort, P. Bergveld, R. Kooyman, and J. Greve, "Possibilities and limitations of direct detection of protein charges by means of an immunological field-effect transistor," *Analytica chimica acta,* vol. 238, pp. 323-329, 1990.

[72]   F. Chiodi, Å. Sidén, and E. Ösby, "Isoelectric focusing of monoclonal immunoglobulin G, A and M followed by detection with the avidin-biotin system," *ELECTROPHORESIS,* vol. 6, pp. 124-128, 1985.

[73] "International Technology Roadmap For Semiconductors 2.0 ", Executive Report 2015.

[74] B. Merriman, I. T. D Team, and J. M. Rothberg, "Progress in Ion Torrent semiconductor chip based sequencing," *ELECTROPHORESIS,* vol. 33, pp. 3397-3417, 2012.

[75] "International Technology Roadmap for Semiconductors," Executive Summary 2001.

[76] K. Bedner, V. A. Guzenko, A. Tarasov, M. Wipf, R. L. Stoop, S. Rigante*, et al.*, "Investigation of the dominant 1/f noise source in silicon nanowire sensors," *Sensors and Actuators B: Chemical,* vol. 191, pp. 270-275, 2014.

[77] J.-L. Burgot, *Ionic equilibria in analytical chemistry*: Springer Science & Business Media, 2012.

[78] E. Stern, R. Wagner, F. J. Sigworth, R. Breaker, T. M. Fahmy, and M. A. Reed, "Importance of the Debye Screening Length on Nanowire Field Effect Transistor Sensors," *Nano Letters,* vol. 7, pp. 3405-3409, 2007.

[79] D. M. Rissin, C. W. Kan, T. G. Campbell, S. C. Howes, D. R. Fournier, L. Song*, et al.*, "Single-molecule enzyme-linked immunosorbent assay detects serum proteins at subfemtomolar concentrations," *Nat Biotech,* vol. 28, pp. 595-599, print 2010.

[80] S. Sorgenfrei, C.-y. Chiu, R. L. Gonzalez, Y.-J. Yu, P. Kim, C. Nuckolls*, et al.*, "Label-free single-molecule detection of DNA-hybridization kinetics with a carbon nanotube field-effect transistor," *Nat Nano,* vol. 6, pp. 126-132, print 2011.

[81] P. Zang, Y. Liang, and W. Hu, "Improved Hydrolytic Stability and Repeatability: pH sensing with APTES-coated silicon nanowire bio-FETs," *Nanotechnology Magazine, IEEE,* vol. 9, pp. 19-28, 2015.

[82] P. Zang, S. Zhang, Y. Liang, and W. Hu, "Noise suppression with additional reference electrode for time-dependent protein sensing tests with Si nanograting FETs," in *Nanotechnology (IEEE-NANO), 2014 IEEE 14th International Conference on*, pp. 930-933, 2014.

[83] F. Patolsky, G. Zheng, and C. M. Lieber, "Fabrication of silicon nanowire devices for ultrasensitive, label-free, real-time detection of biological and chemical species," *Nat. Protocols,* vol. 1, pp. 1711-1724, print 2006.

[84] Z. Qingxue, Z. Dian, and Z. Xuan, "A novel machine learning-enabled framework for instantaneous heart rate monitoring from motion-artifact-corrupted electrocardiogram signals," *Physiological Measurement,* vol. 37, p. 1945, 2016.

BIOGRAPHICAL SKETCH

Pengyuan Zang received his BS degree in Electronic and Information Science and Technology from Peking University, Beijing, China in 2009 and his MS degree in Electrical Engineering from the University of Southern California, Los Angeles, CA in 2011. Since 2011 he has been pursuing his PhD degree in Electrical Engineering at The University of Texas at Dallas, Richardson, TX. His research interests include design, fabrication and characterization of nanowire and other nano-electronic devices, as well as their applications in biosensing.

<div align="center">**CURRICULUM VITAE**</div>

PENGYUAN ZANG

800 W Campbell Rd, RL10/2.716, Richardson, TX 75080
pxz110730@utdallas.edu

EDUCATION

Ph.D. in Electrical Engineering May 2017
  The University of Texas at Dallas, Richardson, TX
  Dissertation: Study of Silicon Nanowire Field Effect Transistor for Analog and Digital Biosensing

M.S. in Electrical Engineering May 2011
  University of Southern California, Los Angeles, CA

B.S. in Electronics July 2009
  Peking University, Beijing, China

EXPERIENCE

THE UNIVERSITY OF TEXAS AT DALLAS ● DOCTORAL RESEARCH
Development of Si Nanowire FETs for Biosensing Applications

- Played a key role in the design and fabrication of Si nanowire FETs with multi-wire channel, fabricated on SOI wafers with six masks for FEOL, metallization and passivation; Devices show excellent performance consistency with small subthreshold swing of 65 mV/Dec, small V_T of 0.7 V and large 6-order on/off current ratio
- Independently designed, fabricated and demonstrated the first Si nanowire FET with multi-serpentine-nanowire channel, and achieved the same excellent performance following the scaling rule, plus improved surface charge sensitivity in pH sensing experiments
- Solved various fabrication problems of Si nanowire FETs with 15 nm linewidth defined by e-beam lithography, and achieved single analyte detection in biosensing; Demonstrated quantum confinement effect (Coulomb blockade) with sub-10 nm nanowire device at room temperature

Development of CMOS Biosensors Fabricated by Industrial Foundries (TI 45 nm, SMIC 180 nm)

- Demonstrated novel CMOS junctionless nanowire FET biosensors with industrial planar technology nodes, via cross-section study and post-fabrication with focused ion beam (FIB) etch and wet etch
- Designed a post-fabrication process utilizing wet etch for CMOS nanowire biosensors with metal wells, analyzed process data, solved problems with protection for bond pads, and demonstrated working devices with serpentine nanowire patterns successfully exposed, as well as floating gate FET biosensors

Biosensing with Si Nanowire FET Biosensors

- Developed a hydrolysis technique to stabilize the surface charge of nanowire gate dielectric in pH sensing, and achieved +/- 0.008 pH accuracy, which exceeded the specifications of existing commercial ISFETs, and led to a startup company with venture investment

THE UNIVERSITY OF TEXAS AT DALLAS ● LAB MANAGEMENT

- Developed 10 standard operating procedures (SOPs) for various fabrication and chemistry processes, which are currently used by all the group members

- Maintained, troubleshot and conducted training sessions for Keithley 4200 and probe station which were openly accessible to all UTD users; Improved and enabled new functions requested by the users

THE UNIVERSITY OF TEXAS AT DALLAS ● TEACHING ASSISTANT
- TA performance was rated "Exceeds" or "Far Exceeds" in *Quality of Work*, *Quantity of Work*, *Dependability*, *Compatibility* and *Attendance*, by professors from all four courses with TA assignments

SKILLS

- Critical Thinking and Problem Solving
- Photolithography and E-Beam Lithography
- CAD Layout Design: AutoCAD, KLayout (photo mask), Raith 150-Two (e-beam mask)
- Plasma Etch: RIE, ICP; Wet Etch, FIB Etch
- Thin Film Deposition: ALD, Evaporation, Sputtering, PECVD; FIB-induced Deposition
- RTA and FG Annealing
- RCA Cleaning
- Characterization & Metrology: Optical Microscopy, SEM, EDS, AFM, Ellipsometry, Profilometry, XPS
- Electrical Characterization (I-V, C-V): Keithley 4200 and Probe Station, oscilloscope, multimeter
- Matlab, C, Visual Basic, OriginPro, COMSOL, SolidWorks

PUBLICATION

PAPERS

P. Zang, Y. Liang, and W. Hu, "Improved Hydrolytic Stability and Repeatability: pH sensing with APTES-coated silicon nanowire bio-FETs," Nanotechnology Magazine, IEEE, vol. 9, pp. 19-28, 2015.

Liang Y, Huang J, Zang P, Kim J, Hu W. Molecular layer deposition of APTES on silicon nanowire biosensors: Surface characterization, stability and pH response. Applied Surface Science. 2014 12/15/;322(0):202-8.

Zang P, Liang Y, Spurgin L, Hu W, editors. pH sensing comparison of vapor and solution APTES coated Si nanograting FETs. Nanotechnology (IEEE-NANO), 2013 13th IEEE Conference on; 2013 5-8 Aug. 2013.

Zang P, Zhang S, Liang Y, Hu W, editors. Noise suppression with additional reference electrode for time-dependent protein sensing tests with Si nanograting FETs. Nanotechnology (IEEE-NANO), 2014 IEEE 14th International Conference on; 2014 18-21 Aug. 2014.

Yang X, Zang P, Frensley W, Zhou D, Hu W, editors. Doping fluctuation induced performance variation in SiNW biosensors. Nanotechnology (IEEE-NANO), 2013 13th IEEE Conference on; 2013 5-8 Aug. 2013.

Zhang S, Zang P, Liang Y, Hu W, editors. Determination of protein titration curves using Si Nanograting FETs. Nanotechnology (IEEE-NANO), 2014 IEEE 14th International Conference on; 2014 18-21 Aug. 2014.

Wang H, Liang Y, Zang P, Young CD, Hu W, editors. Alternating current approach on Si nanograting FETs for pH sensitivity improvement. Nanotechnology (IEEE-NANO), 2014 IEEE 14th International Conference on; 2014 18-21 Aug. 2014.

CONFERENCE ABSTRACT
Zang P, Wang H, Qian L, Zhou D, Hu W, Tao J, et al. Post Fabrication of Foundry-Fabricated CMOS Serpentine Nanowire Biosensor with Focused Ion Beam. The 59th International Conference on Electron, Ion, and Photon Beam Technology and Nanofabrication; San Diego, CA 2015.

Hu W, Zang P, Tao J, Wang H, Li W, Zhou D. Design and Implantation of CMOS Serpentine Finfet Biosensor. The 10th IEEE International Conference on Nano/Micro Engineered and Molecular Systems; Xi'an, China 2015.

Zang P, Liang Y, WANG H, Tao J, Zeng X, Zhou D, Hu W. Digital Biosensing of Influenza Virus with Single Serpentine Si Nanowire Field Effect Transistor. The 61st International Conference on Electron, Ion, and Photon Beam Technology and Nanofabrication; Orlando, FL 2017 (Accepted)